



Universiteit  
Leiden  
The Netherlands

## **Parkinson's protein $\alpha$ -synuclein : membrane interactions and fibril structure**

Kumar, P.

### **Citation**

Kumar, P. (2017, June 27). *Parkinson's protein  $\alpha$ -synuclein : membrane interactions and fibril structure*. *Casimir PhD Series*. Retrieved from <https://hdl.handle.net/1887/50076>

Version: Not Applicable (or Unknown)

License: [Licence agreement concerning inclusion of doctoral thesis in the Institutional Repository of the University of Leiden](#)

Downloaded from: <https://hdl.handle.net/1887/50076>

**Note:** To cite this publication please use the final published version (if applicable).

Cover Page



Universiteit Leiden



The handle <http://hdl.handle.net/1887/50076> holds various files of this Leiden University dissertation

**Author:** Kumar, Pravin

**Title:** Parkinson's protein  $\alpha$ -synuclein : membrane interactions and fibril structure

**Issue Date:** 2017-06-27

# **Parkinson's Protein $\alpha$ -Synuclein: Membrane Interactions and Fibril Structure**

**Pravin Kumar**



# Parkinson's Protein $\alpha$ -Synuclein: Membrane Interactions and Fibril Structure

Proefschrift

ter verkrijging van  
de graad van Doctor aan de Universiteit Leiden,  
op gezag van Rector Magnificus prof.mr. C.J.J.M. Stolker,  
volgens besluit van het College voor Promoties  
te verdedigen op dinsdag 27 juni 2017  
klokke 13.45 uur

door

**Pravin Kumar**

geboren te Munger, Bihar (India)

in 1983

Promotor: Prof. Dr. Edgar J.J. Groenen

Co-promotor: Dr. Martina Huber

Promotiecommissie: Dr. Wolfgang Hoyer (Heinrich-Heine-Universität  
Düsseldorf, Germany)

Prof. Dr. Vinod Subramaniam (Vrije Universiteit,  
Amsterdam)

Prof. Dr. ir. Tjerk H. Oosterkamp (Universiteit  
Leiden)

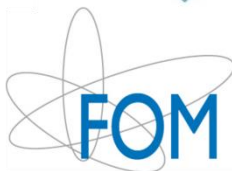
Prof. Dr. Eric R. Eliel (Universiteit Leiden)



Universiteit  
Leiden



leiden  
*Casimir*  
research school



Cover design: by Gabriele Panarelli, Martina Huber & Pravin Kumar

Casimir PhD series, Delft-Leiden 2017-17  
ISBN 978-90-8593-301-4

An electronic version of this thesis can be found at <https://openaccess.leidenuniv.nl>

The work described in this thesis was performed at the Leiden Institute of Physics (LION) and is part of the research program of the Foundation for Fundamental Research on Matter (FOM), which is part of the Netherlands Organization for Scientific Research (NWO).

To

*my beloved mother who could not see this thesis completed  
and my father for their continuous love and support*



# CONTENTS

<b><u>1</u> Introduction</b>	<b>1</b>
1.1 <i><math>\alpha</math>-Synuclein and its properties</i>	2
1.3 <i>Posttranslational modification of <math>\alpha</math>-Synuclein</i>	7
1.4 <i><math>\alpha</math>-Synuclein and fibrils</i>	8
1.6 <i>Spin-label EPR spectroscopy</i>	10
1.6.1 <i>Spin-label mobility</i>	11
1.6.2 <i>Distance determination by EPR</i>	14
1.7 <i>Thesis outline</i>	19
1.8 <i>References</i>	20
<b><u>2</u> Parkinson's Protein <math>\alpha</math>-Synuclein Binds Efficiently and with a Novel Conformation to Two Natural Membrane Mimics</b>	<b>29</b>
2.2 <i>Materials and methods</i>	32
2.2.1 <i>Protein expression and labelling</i>	32
2.2.2 <i>Preparation of vesicles</i>	33
2.2.3 <i>Sample Preparation</i>	33
2.2.4 <i>Continuous wave-EPR experiments</i>	34
2.2.5 <i>DEER experiments</i>	35
2.3 <i>Results</i>	36
2.3.1 <i>Continuous-wave EPR of <math>\alpha</math>S</i>	36
2.3.2 <i>Results of DEER experiments</i>	39
2.4 <i>Discussion</i>	41
2.5 <i>References</i>	44
<b><u>3</u> Membrane Binding of Parkinson's Protein <math>\alpha</math>-Synuclein: Effect of Phosphorylation at Positions 87 and 129</b>	<b>49</b>
3.1 <i>Introduction</i>	50
3.2 <i>Materials and methods</i>	54

3.2.1 Protein expression and labelling	54
3.2.2 Preparation of vesicles	55
3.2.3 Sample Preparation	55
3.2.4 Filtration experiments	55
3.2.5 Continuous wave-EPR experiments	56
3.3 Results	57
3.4 Discussion	64
3.5 References	68
<b>Appendix A to Chapter 3</b>	<b>73</b>
<b>4 Characterization of Fibrils Obtained by Seeded Fibrillization of a Series of Spin-Labeled <math>\alpha</math>-Synuclein Variants by Transmission Electron Microscopy</b>	<b>77</b>
4.1 Introduction	78
4.2 Materials and methods	78
4.2.1 Preparation of fibrillar $\alpha$ S	78
4.2.2 Transmission electron microscopy	81
4.3 Results	81
4.4 Discussion	86
4.5 References	88
<b>Appendix B to chapter 4</b>	<b>91</b>
<b>5 Nanometer Distance Constraints for the Fold of <math>\alpha</math>-Synuclein in Fibrils of Single Morphology</b>	<b>93</b>
5.1 Introduction	94
5.2 Materials and methods	97
5.2.1 Expression and purification of cysteine mutants of the $\alpha$ -Synuclein protein	97
5.2.2 Preparation of $\alpha$ S fibril seeds	97
5.2.3 Seeded fibrillization of spin labelled $\alpha$ S and harvesting	98
5.2.4 Transmission electron microscopy	99

5.2.5 Continuous-wave EPR at 120 K	100
5.2.6 DEER measurements	100
5.2.7 MMM analysis	101
5.3 Results	102
5.3.2 MMM derived distance distributions	107
5.4 Discussion	108
5.4.1 Distances from DEER experiments	109
5.4.2 Comparison with DEER distances from other studies	111
5.4.3 Comparison with recently published structural models	112
5.5 References	115
<b>Appendix C to chapter 5</b>	<b>119</b>
<b>Appendix D to chapter 5: Exploring Methods to Increase the DEER Evolution Time in <math>\alpha</math>-Synuclein Fibrils: Deuteration of Buffer and 35 GHz DEER</b>	<b>122</b>
<b>6 Understanding the Peptide-Coiled-Coil Interaction of the Membrane-Fusion K/E Peptides</b>	<b>129</b>
6.1 Introduction	130
6.2 Materials and methods	133
6.2.1 Peptide synthesis, labelling and sample preparation	133
6.2.2 cw-EPR measurements at 120 K	134
6.2.3 DEER measurements	135
6.3 Results	136
6.4 Discussion	140
6.5 References	143
<b>Summary</b>	<b>147</b>
<b>Samenvatting</b>	<b>151</b>
<b>Curriculum Vitae</b>	<b>155</b>

<b>List of Publications</b>	<b>157</b>
<b>Acknowledgements</b>	<b>159</b>

# **1 Introduction**

## Chapter 1

Parkinson's disease (PD) (1) is the second most highly spread neurodegenerative disease after Alzheimer's (2), and affects primarily the elderly population (2,3). The clinical effect of PD is associated with the loss of dopaminergic neurons from part of the mid-brain called *substantia nigra pars compacta* (2,4,5). The most common symptoms of PD are movement-related such as resting tremor, bradykinesia, muscular rigidity and postural instability (2,4,5). These symptoms were first described by James Parkinson in 1817 (1). Moreover, patients may have other problems like depression, olfactory deficits, psychosis, cognitive impairment and sleeping problems (6–8). To find a cure to PD is still difficult, because the symptoms of the disease are not early detectable. PD is characterized by the presence of Lewy bodies in the patient's brain (9). The Lewy body is a protein deposit, which mainly consists of aggregates of  $\alpha$ -Synuclein (9,10). This protein is expressed abundantly in the brain and localizes in the presynaptic terminal of nerve cells (11,12).

This thesis focuses on the protein  $\alpha$ -Synuclein ( $\alpha$ S). Its ability to interact with membranes as well as to form amyloid fibrils in certain conditions are the main aspects of this thesis. Spin-label electron paramagnetic resonance (EPR) is the method used to study these complex processes. This chapter presents a brief introduction to this thesis. We describe the protein  $\alpha$ S, its membrane interaction, fibrils, and spin-label EPR.

### 1.1 $\alpha$ -Synuclein and its properties

The protein  $\alpha$ S consists of 140 amino acids. It lacks a defined secondary structure in solution at neutral pH (13,14) and is a member of the intrinsically disordered protein (IDP) class (15,16). The amino acid sequence of  $\alpha$ S can be divided into two major regions: a) the N-terminal region (residues 1-100), which can be further

## Chapter 1

divided into two sub regions: a highly positively charged region (residues from 1-60), and a hydrophobic non-amyloid-beta-component (NAC) region (residues 61-94); and b) the C-terminal region (residues 100-140), which is rich in negatively charged amino acids, especially glutamate (see Figure 1.1).

The N-terminal region contains the seven imperfect repeats (KTKEGV consensus sequence) spread from residue 7 to residue 87 (11,17), and has a tendency to form an  $\alpha$ -helical conformation upon membrane binding (14,18–21). The three most common point mutations in  $\alpha$ S linked to PD are A30P (22), E46K (23), A53T (24). In addition, two other point mutations G51D (25), H50Q (26), and A53E (92) have been described recently. They are all located in the N-terminal region of  $\alpha$ S. The NAC region plays a crucial role in the aggregation of  $\alpha$ S (27), and the C-terminal part of  $\alpha$ S remains largely unstructured under most conditions (18).

Like other proteins,  $\alpha$ S can undergo posttranslational modification (PTM). Phosphorylation (28–30), ubiquitination (31), oxidation (32), and truncation (33) are commonly found PTMs in  $\alpha$ S. These PTMs have an impact on the structure and function of  $\alpha$ S (34,35).

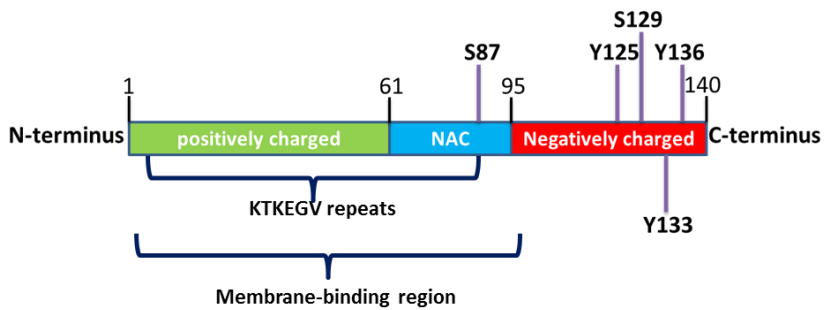


Figure 1.1. Schematic representation of the  $\alpha$ S sequence and its different regions: The N-terminal region contains the highly positively charged region (in green), the KTKEGV repeats, and the central region (in blue), also called the NAC region. The C-terminal region (in red), the negatively charged region, contains most of the phosphorylation sites. The NAC region also contains a phosphorylation site at serine (S) 87. The numbers mark the residues and the numbers in bold the phosphorylation sites of  $\alpha$ S.

## Chapter 1

### 1.2 $\alpha$ -Synuclein and membrane interaction

One of the proposed physiological functions of  $\alpha$ S is neurotransmitter release (Figure 1.2) (36). In this process,  $\alpha$ S is believed to interact with synaptic vesicles, to cluster them and bring them in close proximity of the presynaptic membrane. The protein  $\alpha$ S also interacts with SNARE complex proteins (37,38) at synaptic vesicles. Besides in presynaptic terminals,  $\alpha$ S is also found in the mitochondria. The presence of  $\alpha$ S in mitochondria disturbs the functioning of mitochondria (mitochondrial dysfunction) (39–41). These functions involve the interaction of  $\alpha$ S with membranes.

In vitro studies suggest that early-onset PD mutations do not only affect the aggregation tendency of  $\alpha$ S, but also modulate the  $\alpha$ S-membrane interaction (19,21,42). These observations make the interaction of  $\alpha$ S with membranes of great interest. Therefore, the  $\alpha$ S-membrane interaction was studied (43–64), mostly using membranes composed of simple lipids or binary lipid mixtures. The lipid composition of natural membranes is complicated as these natural membranes contain a complex mixture of lipids. In chapter 2 of this thesis, we investigate the interaction of  $\alpha$ S with two natural membrane mimics, the Inner Mitochondrial membrane (IMM) and the Neuronal Plasma membrane (NPM).

The protein  $\alpha$ S interacts with the membrane by the N-terminal part (residues 1-100) of the protein. Upon binding to membranes,  $\alpha$ S attains an amphipathic  $\alpha$ -helical conformation (14,18,63). The membrane-bound-N-terminal- $\alpha$ -helical region consists of three regions, one is called helix 1 (residues 3-37), the second is helix 2 (residues 45-92) and the third is the linker part in between the two helices (43,44). The affinity of  $\alpha$ S to membranes depends on the negative charge density ( $\rho$ ) of the membrane (54,55,63), where  $\rho$  represents the molar fraction of anionic lipids present in the membrane (56).

## Chapter 1

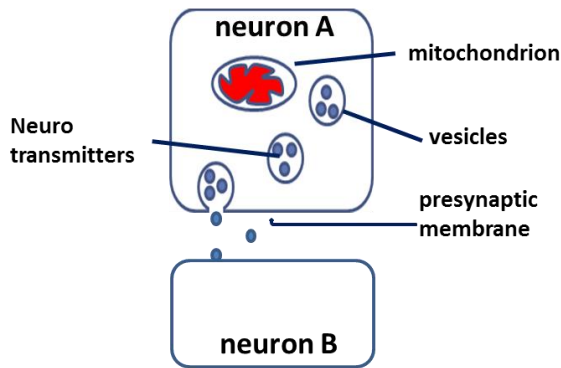


Figure 1.2. The proposed physiological function of  $\alpha S$ : Schematic representation of a synapse showing the process of neurotransmission from neuron A to neuron B. In this process,  $\alpha S$  interacts with vesicles loaded with neurotransmitters, clusters them and brings them to the presynaptic membrane. Vesicles fuse and release the neurotransmitters. The protein  $\alpha S$  is present in mitochondria (shown in red) of cells, where  $\alpha S$  interacts with the mitochondrial membranes.

If the membrane has a higher charge density ( $\rho = 0.5$  to  $1$ ),  $\alpha S$  binds with both helices to the membrane (Figure 1.3a). At low surface charge density ( $\rho < 0.5$ ), helix 1 of  $\alpha S$  remains attached to the membrane while helix 2 shows weak binding and detaches, starting from the C-terminal side of the protein (Figure 1.3b) (56). In connection to these observations, in chapter 2, we investigate the binding of  $\alpha S$  with the IMM and the NPM, which have a low negative charge density of  $\rho = 0.2$  and  $0.3$ , respectively.

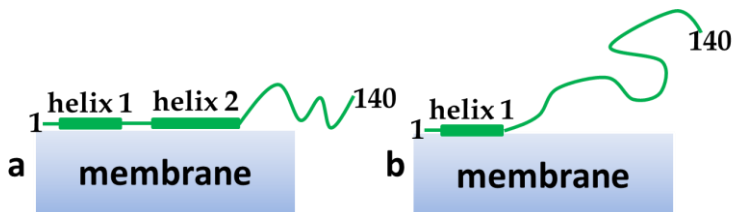


Figure 1.3. Schematic representation of  $\alpha S$ -membrane interaction. Two conditions are shown: a. both helices of  $\alpha S$  are completely bound to the membrane with high charge density; b. Helix 2 is detached from the membrane with low charge density, whereas  $\alpha S$  remains bound via helix 1.

## Chapter 1

As a consequence of binding to membranes, the  $\alpha S$  attains different conformations. On membranes,  $\alpha S$  can be in the extended or the horseshoe conformation shown in Figure 1.4. Figure 1.4a depicts the extended conformation, and Figure 1.4b represents the horseshoe, also called the broken helix conformation. The helical region of  $\alpha S$  has a break in the middle (residue 42 to 44), hence named linker region. The first report of the horseshoe conformation came from a solution-NMR study (43) of  $\alpha S$  on micelles by Ulmer *et al.* (43). Later, one EPR study by Georgieva *et al.*(46) reported the presence of the extended conformation on vesicles, bicelles, and rod-like micelles, while other EPR studies (52,64) show the presence of the horseshoe conformation on vesicles and micelles.

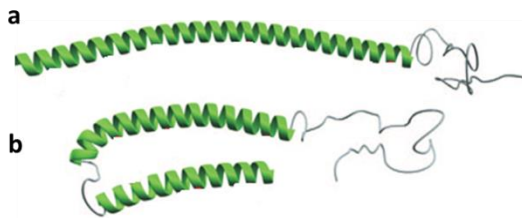


Figure 1.4. Schematic diagram of  $\alpha S$  conformation (58) upon membrane binding: a. the extended conformation, b. the broken helix conformation also termed horseshoe conformation.

Other studies (45,51,58) found that  $\alpha S$  coexists in both forms, the extended and the horseshoe. It is still a question whether the membrane-bound part of  $\alpha S$  has the extended or the horseshoe form, especially when considering membranes with compositions close to natural membranes. In chapter 2 of this thesis, we report the arrangement of  $\alpha S$  on the natural membranes IMM and NPM.

## Chapter 1

### 1.3 Posttranslational modification of $\alpha$ -Synuclein

As we mentioned above, the protein  $\alpha$ S undergoes several modifications. The most observed and studied modification is phosphorylation, a chemical process in which a phosphate group is attached to a hydroxyl group (R-OH) (Figure 1.5). For proteins, an amino-acid residue with a hydroxyl group (for example serine (S), tyrosine (Y), and threonine (T)) is phosphorylated by enzymes, normally protein kinases, by the addition of a covalently bound phosphate group. Serine and tyrosine are the residues that undergo phosphorylation in  $\alpha$ S. Figure 1.5 shows the phosphorylated form of serine and of tyrosine. The common phosphorylation sites of  $\alpha$ S are shown in Figure 1.1.

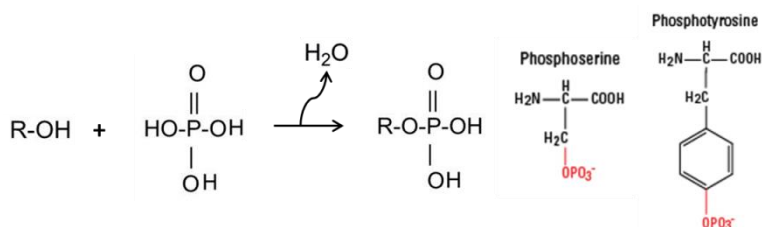


Figure 1.5. Schematic showing the process of phosphorylation and the two amino acids (serine and tyrosine) after phosphorylation: phosphoserine and phosphotyrosine.

In the Lewy bodies,  $\alpha$ S has been found phosphorylated at residue S129 (28,65,66). The other residue found phosphorylated, albeit less than S129, is S87 (30,67). Residue S129 resides in the C-terminal part, which is not in the core of the  $\alpha$ S fibrils (discussed below) that make up the Lewy bodies. Therefore, S129 could be more accessible to phosphorylation in the fibril/Lewy body than S87. Studies to understand the effect of phosphorylation on the aggregation and membrane binding properties of  $\alpha$ S show conflicting results. In connection to this, we choose to investigate the relation between  $\alpha$ S-membrane binding and phosphorylation. In chapter 3, we report how the phosphorylation of  $\alpha$ S affects membrane binding.

## Chapter 1

### 1.4 $\alpha$ -Synuclein and fibrils

The protein  $\alpha$ S is found as fibrillar aggregates in the Lewy bodies (9,68) where it adopts a highly ordered structure, the amyloid fibril. The amyloid fibrils have a width of approximately 10 nm and a length of a few micrometers (69). The amyloid fibril has a cross  $\beta$ -sheet structure (70). In these fibrils, schematically represented in Figure 1.6, individual proteins form  $\beta$ -strands (shown with black arrow), which arrange perpendicular to the fibril axis into a  $\beta$ -sheet structure (shown as grey sheets). The  $\beta$ -sheets grow along the fibril axis to make the protofibrils.

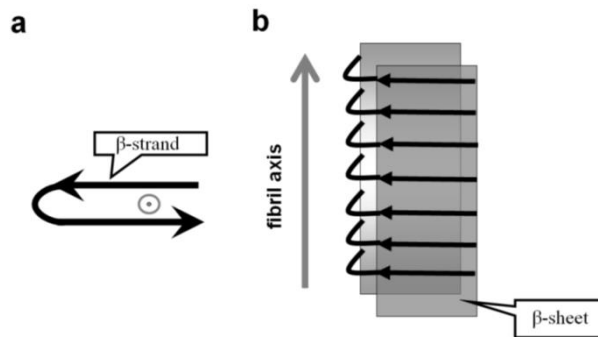


Figure 1.6. Schematic representation of amyloid fibrils . a: the black arrow shows a  $\beta$ -strand and the grey dot shows the direction of the fibril axis, which is pointing out of the page. b: the grey arrow shows the direction of the fibril axis. The grey planes are representative of  $\beta$ -sheets, which are parallel to the fibril axis. Adapted from (78).

The cross  $\beta$ -sheet structure is a common feature of amyloid fibrils, and many proteins are able to form fibrils. Amyloid fibrils made from the same protein can have different morphologies, a phenomenon called polymorphism. This also applies to  $\alpha$ S fibrils. In Figure 1.7, we show transmission electron microscope (TEM) images of  $\alpha$ S fibrils with two forms, cylindrical and twisted. The cylindrical fibrils have a uniform width indicated by black arrows in Figure 1.7a, while twisted fibrils are characterized by the twists indicated by white arrows in Figure 1.7b.

## Chapter 1

Polymorphism among fibrils can be due to a) a difference in the number of protofibrils making the fibrils (71,72), b) a different protofibrils arrangement inside fibrils, or c) a difference in the intrinsic protofibrils structure (73–75). This means that polymorphism can affect the internal fold of  $\alpha$ S in fibrils. Since we study the fold of  $\alpha$ S in fibrils by EPR spectroscopy in chapter 5 of this thesis, it is desired to have fibrils of similar morphology. Chapter 4 describes the TEM characterization of fibrils.

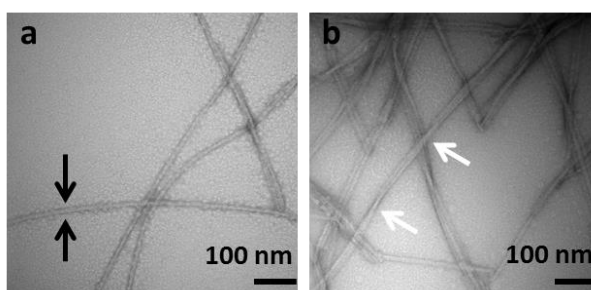


Figure 1.7. Structural characterization of two different polymorphs of  $\alpha$ S fibrils. TEM images of  $\alpha$ S showing a. cylindrical fibrils with uniform width, indicated by black arrows; b. twisted fibrils, where white arrows depict the points of cross-over of a twist in the fibril and the distance between the two points is called the periodicity.

### 1.5 Protein mediated membrane fusion

Membrane fusion is an important process in all living organisms. It is widely accepted that membrane fusion takes place in three steps, schematically represented in Figure 1.8: 1. two unfused vesicles are brought into close proximity; 2. local disruption of the outer membranes at the site of contact, also called hemifusion; 3. fusion facilitating mixing of content between the two fused vesicles (76,77). Despite this common understanding, the detailed mechanism is still lacking.

## Chapter 1

One of the best studied membrane fusion systems is the SNARE system (SNARE: soluble NSF attachment protein receptor; NSF=*N*-ethylmaleimide-sensitive factor), which involves the coiled-coil interaction between three complementary SNARE proteins (76,79). SNARE proteins are located on unfused vesicles and, in the first step of the fusion process, bind to form a tetrameric coiled-coil bringing the unfused vesicles into close contact and triggering the fusion cascade (80). In connection to that, in chapter 6 of this thesis, we investigate the first step of the fusion process, which is to bring two membranes close by the coiled-coil interaction. We use two synthetic small peptides E and K, which form K:E heterodimers with a coiled-coil structure (81). We describe in detail how the two peptides interact and arrange themselves in the coiled-coil structure.

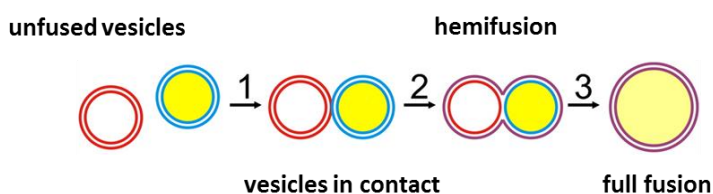


Figure 1.8. Membrane fusion steps shown with vesicles: Two unfused vesicles get closer, docking (1), mixing of outer lipid layer (hemifusion) (2) and then full fusion by mixing inner lipid layer and content (3). The Figure is modified from (77).

### 1.6 Spin-label EPR spectroscopy

Electron-paramagnetic-resonance (EPR) spectroscopy is a method that is sensitive to paramagnetic systems. In nature most bio-macromolecules do not contain a paramagnetic center, which makes them EPR silent. To make these molecules detectable by EPR, they need to be spin labelled. With the development of site directed spin-labelling strategies (82–84), EPR has become a powerful tool to investigate structural aspects of bio-macromolecular complexes.

## Chapter 1

Nitroxide radicals are used as spin-labels in EPR studies. The commonly used nitroxide radical is MTS ((1-oxyl-2,2,5,5-tetramethylpyrroline-3-methyl) methanethiosulfonate). Figure 1.9 shows the chemical structure of MTS. The MTS chemical structure contains a five-membered pyrroline ring with N-O bond and a methanethiosulfonate group. The unpaired electron localizes in the N-O bond shown with a black dot in Figure 1.9. The spin label attaches to a protein by a covalent bond between the –SH group of cysteine and the methanethiosulfonate of MTS.

Spin-label EPR is useful to obtain information such as: a. mobility of the spin label, b. distance between two spins, c. solvent accessibility of the spin-labelled protein site, d. polarity of the local environment of the spin label. In our research, we focus on the first two aspects. Therefore, in the following part of this chapter, we will describe briefly the effect of spin-label mobility on EPR spectra and the determination by EPR of the distance between two spins.

### 1.6.1 Spin-label mobility

The EPR spectrum of nitroxides is sensitive to the rotation of the spin label with respect to the external magnetic field. If the nitroxide spin label is freely mobile in solution, it exhibits an EPR spectrum with three narrow lines as shown in Figure 1.10a. The lines are spaced by the isotropic nitrogen hyperfine interaction  $A_{iso}$ , which is due to the hyperfine interaction of the unpaired electron spin  $S = 1/2$  with the  $^{14}\text{N}$  nuclear spin  $I = 1$ .

## Chapter 1

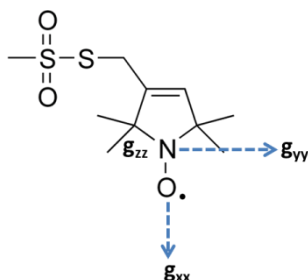


Figure 1.9. The chemical structure of the MTS nitroxide radical. The unpaired electron (shown as a black dot) localizes on the N-O bond attached to the five-membered pyrroline ring. Principal directions of the g-tensor (blue dotted arrows) are shown. The g-tensor along the Z-direction, i.e.,  $g_{zz}$  is perpendicular to the ring.

Figure 1.10 shows the effect of the spin-label mobility in terms of the rotation-correlation time ( $\tau_r$ ) on the line shape of the EPR spectrum by a set of simulations. At  $\tau_r$  values from 0.01 ns to 0.1 ns, the line position stays fixed, and the linewidth increases in a characteristic way (Figure 1.10a and b). The line at high field broadens and shifts slightly as the rotation-correlation time increases from 0.1 ns to 1 ns. For the spectra with  $\tau_r$  values of 3.2 ns and 10 ns, the line positions change and the lines at low field and high field broaden. For longer times ( $\tau_r > 10$  ns), the spectrum approaches that of a completely immobilized spin label (Figure 1.10f). In chapters 2 and 3 of this thesis, we have used the spin-label mobility to investigate the interaction of  $\alpha$ S with membranes.

## Chapter 1

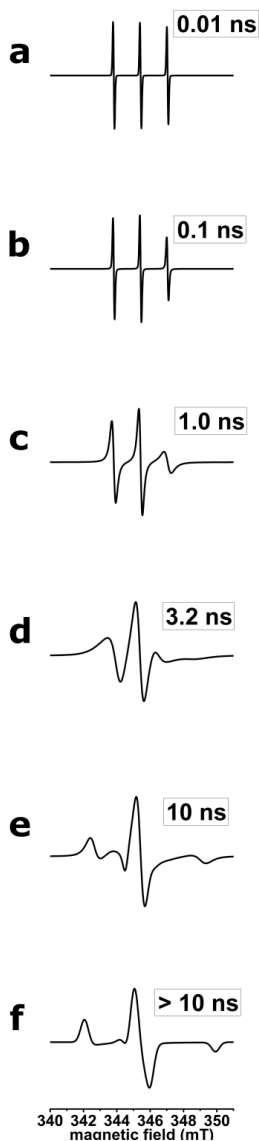


Figure 1.10. Simulated cw-EPR spectra to show the effect of the rotational motion of a nitroxide spin label on the line shape of the spectrum at room temperature. In the fast-motion regime, the three lines have almost equal intensities; a.  $\tau_r = 0.01$  ns, b.  $\tau_r = 0.1$  ns, c.  $\tau_r = 1.0$  ns, d.  $\tau_r = 3.2$  ns, e.  $\tau_r = 10.0$  ns, and f.  $\tau_r > 10.0$  ns. Spectra a to c were simulated with the algorithm “garlic”, d to e with “chili” and f with “pepper” using the EasySpin (85) package. We used a g tensor  $[g_{xx} \ g_{yy} \ g_{zz}] = [2.009006 \ 2.00687 \ 2.003]$ , and a hyperfine coupling  $[A_{xx} \ A_{yy} \ A_{zz}] = [13 \ 13 \ 110]$  MHz. The linewidth parameter used for spectra a to e was 0.1 mT, and for spectrum f, 0.55 mT was used.

## Chapter 1

### 1.6.2 Distance determination by EPR

An important part of this thesis concerns structure determination by EPR, which is based upon the measurement of distances between pairs of spin labels. The measurement of distances makes use of the dipole-dipole interaction between the electron spins of two nitroxides. For nitroxide spin labels, the electron spin is considered to be localized in the center of the N-O bond. For systems where the distance between two spins is above 1 nm, the interaction of the spin can be described under the assumption of point-dipole approximation (86).

The dipole-dipole interaction ( $\nu_{dd}$  in MHz units) between two spins is proportional to the inverse cube of the distance, and is given by (86)

$$\nu_{dd} = -\frac{\mu_0 \hbar \gamma_A \gamma_B}{8\pi^2 r_{AB}^3} (3\cos^2 \theta - 1)$$

where  $\mu_0$  is the magnetic permeability at vacuum,  $\gamma_A$  and  $\gamma_B$  are the magnetogyric ratios for the two spins,  $\hbar$  is the reduced Planck's constant,  $r_{AB}$  is the distance between the two spins, and  $\theta$  is the angle between the spin-spin vector and the magnetic field.

The distance between pairs of spins can be measured by EPR in two ways depending on the distance; a) by cw-EPR and b) by a pulsed-EPR method called double electron-electron resonance (DEER), which is discussed below.

#### 1.6.2.1 cw-EPR line broadening

Short distances up to 2 nm between two spins can be detected by cw-EPR. Figure 1.11 depicts the cw-EPR spectra of frozen nitroxides as a function of the dipolar interaction. The spectra are simulated using a dipolar tensor  $D$ , of the form

## Chapter 1

$[-D - D + 2D]$  in which  $+2D$  represents the parallel component of the dipolar tensor ( $D_{||}$ ). Figure 1.11 shows the effect of the dipolar coupling on the lineshape of cw-EPR spectra of nitroxides, where the parallel component of the dipolar tensor was aligned either with the  $g_{yy}$  and  $A_{yy}$  direction or the  $g_{zz}$  and  $A_{zz}$  direction of the  $g$  and  $A$  tensors of the two nitroxides, assuming that the  $g$  and the  $A$  tensors of the two nitroxides are collinear. The direction of the principal axes of the  $g$ -tensor is indicated with blue dotted lines in Figure 1.9.

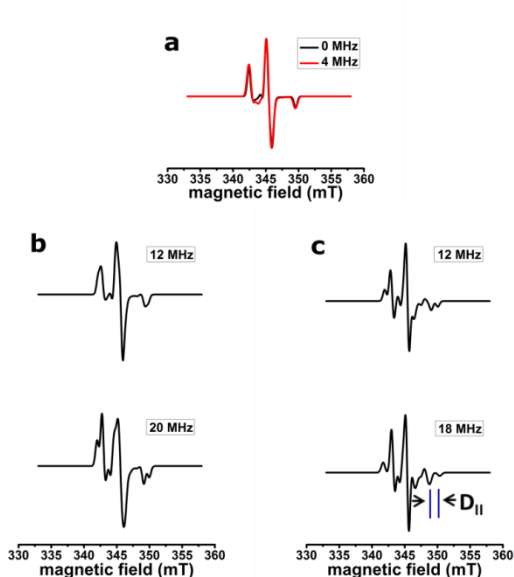


Figure 1.11. Effect of dipolar coupling on cw-EPR spectra of nitroxides at 120 K. a. Nitroxide spectrum simulated without dipolar interaction (black line) superimposed with simulated nitroxide spectrum for  $D = 4$  MHz for  $D_{||}$  along the Z-direction (red line), b. simulated nitroxide spectrum showing dipolar line broadening and splitting at low and high field for  $D = 12$  MHz (top) and  $D = 20$  MHz (bottom) for  $D_{||}$  along the Y-direction, c. nitroxide spectrum showing dipolar line broadening and splitting at low field and high field for  $D = 12$  MHz (top) and  $D = 18$  MHz (bottom) for  $D_{||}$  along the Z-direction. The splitting of the line at high field marked by blue lines corresponds to 1.4 mT, i.e., 36 MHz (magnitude of  $D_{||}$  along the Z-direction). All the spectra were simulated with the algorithm “pepper” using the EasySpin (85) package. We used a  $g$  tensor  $[g_{xx} \ g_{yy} \ g_{zz}] = [2.009006 \ 2.00687 \ 2.003]$ , and a hyperfine coupling  $[A_{xx} \ A_{yy} \ A_{zz}] = [13 \ 13 \ 100]$  MHz. The linewidth was kept fixed at 0.55 mT.

## Chapter 1

Figure 1.11a shows the superposition of the spectrum simulated for  $D = 0$  MHz (Figure 1.11a, black line) with the spectrum for  $D = 4$  MHz, and  $D_{||}$  along the Z-direction. This comparison depicts that the changes in lineshape become visible for dipolar coupling of  $D = 4$  MHz (i.e., a distance of 2.35 nm between two spins). In Figure 1.11b, the parallel component was aligned with the Y-direction. For  $D = 12$  MHz (i.e., a distance of 1.6 nm), the spectrum only slightly deviates from the one in the absence of dipolar interaction (Figure 1.11 b, top). With the increase of the  $D$  value to 20 MHz (i.e., a distance of 1.37 nm), a splitting of lines becomes visible (Figure 1.11 b, bottom). In Figure 1.11c, the  $D_{||}$  was aligned along the Z-direction. For  $D = 12$  MHz (i.e., a distance of 1.6 nm), the splitting of the low-field and high-field lines becomes visible (Figure 1.11c, top). The splitting of the low-field and the high-field line becomes larger for  $D = 18$  MHz (i.e., a distance of 1.4 nm) (Figure 1.11c, bottom). In this case, the splitting of the EPR line at high field (indicated with blue lines) corresponds to 36 MHz, i.e., the magnitude of  $D_{||}$ .

These simulations show how the lineshape varies with the orientation of the dipolar axis with respect to the  $g$  and  $A$  tensors of the nitroxides. The simulated effect is more pronounced than for real samples, which may be due to: a) in the simulation,  $D_{||}$  is aligned with a canonical orientation of the nitroxide, i.e.,  $g_{yy}$  or  $g_{zz}$ , but arbitrary orientations of  $D_{||}$  will distribute the effect over the spectral lines, making the broadening less visible. b) the  $g$ -tensors of the two nitroxides are taken collinear in the simulation, while in practice this need not to be the case and there will be a distribution of orientations.

In chapter 6, we have used this method to derive inter-spin distances from line broadening in cw-EPR spectra.

### 1.6.2.2 Double electron-electron resonance (DEER)

For distances between two electron spins larger than 2 nm, their dipolar interaction becomes too weak to be detectable as a line broadening of transitions in cw-EPR spectra. Pulsed-EPR methods are available to determine the dipolar interaction in such cases and in our research we have made use of double electron-electron resonance (DEER) to access distances between 1.8 and 6 nm (87). The DEER pulse sequence is represented in Figure 1.12a. The two interacting spins are excited at distinct microwave frequencies, the so-called observer and pump frequencies. The three-pulse excitation of one of the spins (the observer spin) results in a spin echo, as indicated in the top line. Excitation of the second spin, which is in interaction with the first one, with microwaves at the pump frequency and at a time between the second and third pulse at the observer frequency, results in a modulation of the echo intensity. The variation of the echo intensity as a function of the dipolar evolution time  $t$  is called the DEER-trace. As an example, Figure 1.12b, shows the DEER trace of a model sample, the biradical PH2, in which two nitroxide groups are covalently linked at a distance of 1.9 nm. The modulation at the frequency  $\nu_{dd}$ , owing to the dipolar interaction between the two nitroxide spins, is clearly visible superimposed on the echo decay, which results from relaxation. For a distribution of distances between the two spins, for example for non-covalently bound nitroxide radicals, the modulation pattern will become less obvious or even smeared out completely, as illustrated in Figure 1.12c. In this case the separation of the effect of the dipolar interaction from other contributions to the echo decay becomes important. After subtraction of this background, the decrease of the echo intensity owing to the dipolar coupling remains and can be translated into a distribution of distances. The modulation

## Chapter 1

depth ( $\lambda$ ) (Figure 1.12c) is related to the number of coupled spins that account for the measured DEER trace.

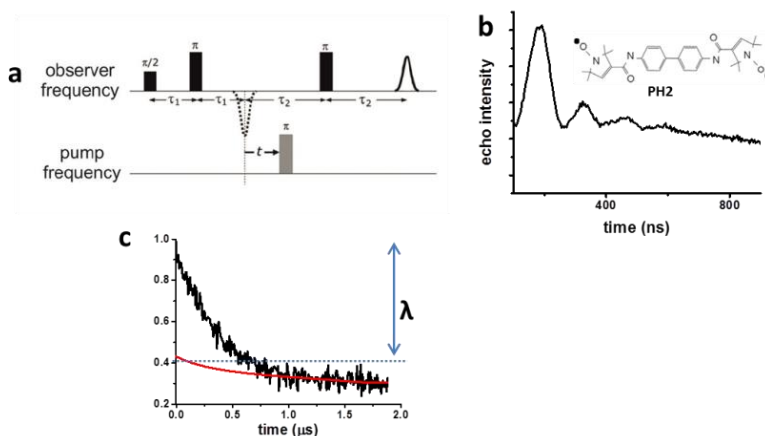


Figure 1.12. The DEER experiment. a. The DEER four-pulse sequence at two frequencies, the observer and the pump frequency. Delay times  $\tau_1$  and  $\tau_2$  are kept fixed, while the delay time  $t$  between the unobserved first echo (dotted line) and the pump pulse is varied. b. The measured DEER trace of a reference sample PH2 contains modulations, the period of which is related to the dipolar coupling between two electron spins. c. the DEER trace of a fibril sample (black line), which shows no modulations; the red line represents the background derived from the singly labelled proteins. The modulation depth ( $\lambda$ ) represents the number of spins that contribute to the measured DEER trace.

For broad distance distributions, special attention has to be paid to the background, which is due to all interactions of spins that belong to all spin-labelled proteins, referred to as nano-objects (87,88). For a random distribution of these nano-objects, analytical background functions were calculated in (87,88). For soluble proteins, in buffer, the background is defined by a homogeneous 3D-background function, which describes the three-dimensional, random distribution of nano-objects in the sample (87–90). Such a background has been applied in chapter 6. The DEER traces of peptides or proteins bound to membranes can be corrected by a 2D background function, since membrane-bound proteins are randomly distributed in the plane of the lipid-bilayer(88,91). In

## Chapter 1

chapter 2 of this thesis, we derived the background function for the membrane-bound doubly-labelled proteins from that of the membrane-bound singly-labelled proteins. For the fibrils investigated in chapter 5, we encounter a special situation. For fibrils, the background dimensionality is expected to be close to a 1D-background function since the nano-objects, i.e., the doubly spin-labelled proteins are arranged preferentially in one dimension, which is along the fibril axis (Figure 1.6b, black arrow). Usually, the background function for fibrils is derived from the singly labelled proteins (chapter 5).

### 1.7 Thesis outline

In chapter 2, continuous wave (cw)-EPR is employed to investigate the interaction of  $\alpha$ S with natural membranes. The membrane is presented in the form of SUVs, composed of lipids that mimic the natural membranes IMM and NPM. In the same chapter we examine the arrangement of  $\alpha$ S on the membrane by measuring the distance between two spins on the same  $\alpha$ S protein by double electron-electron resonance (DEER).

In chapter 3, we investigate the influence of phosphorylation on the binding of  $\alpha$ S with model membranes by cw-EPR. We mimic the phosphorylation of  $\alpha$ S at position S87 and S129.

In chapter 4, the fibril morphology of  $\alpha$ S is characterized by negative stain transmission electron microscopy (TEM). This study provides the necessary information about the fibril morphology.

In chapter 5, we investigate the fibril fold of  $\alpha$ S by DEER. In this study we use the fibrils whose characterization was described in chapter 4.

In chapter 6, the arrangement of K/E peptides in their coiled-coil structure is investigated by cw-EPR and DEER, which reveals the orientation of the individual peptide in the coiled-coil structure.

## Chapter 1

### 1.8 References

1. Parkinson J. An Essay on the Shaking Palsy (Whitingham and Rowland, London). 1817.
2. Ozansoy M, Başak AN. The central theme of parkinson's disease:  $\alpha$ -Synuclein. *Mol Neurobiol.* 2013;47:460–465.
3. De Rijk MC, Breteler MM, Graveland GA, Ott A, Grobbee DE, van der Meché FG, Hofman A. Prevalence of Parkinson's disease in the elderly: the Rotterdam Study. *Neurology.* 1995;45:2143–2146.
4. Cookson MR.  $\alpha$ -Synuclein and neuronal cell death. *Mol Neurodegener.* 2009;4:9.
5. Gasser T. Molecular pathogenesis of Parkinson disease: insights from genetic studies. *Expert Rev Mol Med.* 2009;11:1-20.
6. Wolters EC. Non-motor extranigral signs and symptoms in Parkinson's disease. *Parkinsonism Relat Disord.* 2009;15:S6–S12.
7. Gasser T, Hardy J, Mizuno Y. Milestones in PD genetics. *Mov Disord.* 2011;26:1042–1048.
8. Dickson DW, Fujishiro H, Orr C, DelleDonne A, Josephs KA, Frigerio R, Burnett M, Parisi JE, klos KJ, Ahlskog JE. Neuropathology of non-motor features of Parkinson disease. *Parkinsonism Relat Disord.* 2009;15:S1–S5.
9. Spillantini M, Schmidt M, Lee V, Trojanowski J, Jakes R, Goedert M.  $\alpha$ -Synuclein in Lewy bodies. *Nature.* 1997;388:839–840.
10. Spillantini MG, Crowther RA, Jakes R, Hasegawa M, Goedert M.  $\alpha$ -Synuclein in filamentous inclusions of Lewy bodies from Parkinson's disease and dementia with Lewy bodies. *Proc Natl Acad Sci U S A.* 1998;95:6469–6473.
11. Maroteaux L, Campanelli JT, Scheller RH. Synuclein: a neuron-specific protein localized to the nucleus and presynaptic nerve terminal. *J Neurosci.* 1988;8:2804–2815.
12. Shumin Liu, Ipe Ninan, Irina Antonova, Fortunato Battaglia, Fabrizio Trinchese, Archana Narasanna, Nikolai Kolodilov, William Dauer, Robert D Hawkins OA.  $\alpha$ -Synuclein produces a long-lasting increase in neurotransmitter release. *EMBO J.* 2004;23:4506–4516.
13. Uversky VN. Protein folding revisited. A polypeptide chain at the folding-misfolding-nonfolding cross-roads: which way to go? *Cell Mol Life Sci.* 2003;60:1852–1871.

## Chapter 1

14. Davidson WS, Jonas A, Clayton DF, George JM. Stabilization of  $\alpha$ -Synuclein secondary structure upon binding to synthetic membranes. *J Biol Chem.* 1998;273:9443–9449.
15. Dunker AK, Lawson JD, Brown CJ, Williams RM, Romero P, Oh JS, Oldfield CJ, Campen AM, Ratliff CM, Hipps KW, Ausio J, Nissen MS, Reeves R, Kang C, Kissinger CR, Bailey RW, Griswold MD, Chiu W, Garner EC, Obradovic Z. Intrinsically disordered protein. *J Mol Graph Model.* 2001;19:26–59.
16. Dyson HJ, Wright PE. Intrinsically unstructured proteins and their functions. *Nat Rev Mol Cell Biol.* 2005;6:197–208.
17. Goedert M. The awakening of  $\alpha$ -Synuclein. *Nature.* 1997;388:232–232.
18. Eliezer D, Kutluay E, Bussell R, Browne G. Conformational properties of  $\alpha$ -Synuclein in its free and lipid-associated states. *J Mol Biol.* 2001;307:1061–1073.
19. Perrin RJ, Woods WS, Clayton DF, George JM. Interaction of human  $\alpha$ -Synuclein and Parkinson's disease variants with phospholipids. Structural analysis using site-directed mutagenesis. *J Biol Chem.* 2000;275:34393–34398.
20. Jo E, McLaurin J, Yip CM, St. George-Hyslop P, Fraser PE.  $\alpha$ -Synuclein membrane interactions and lipid specificity. *J Biol Chem.* 2000;275:34328–34334.
21. Jo E, Fuller N, Rand RP, St George-Hyslop P, Fraser PE. Defective membrane interactions of familial Parkinson's disease mutant A30P  $\alpha$ -Synuclein. *J Mol Biol.* 2002;315:799–807.
22. Krüger R, Kuhn W, Müller T, Woitalla D, Graeber M, Kösel S, Przuntek H, Eppelen JT, Schols L, Riess O. AlaSOPro mutation in the gene encoding  $\alpha$ -Synuclein in Parkinson's disease. *Nat Genet.* 1998;18:106–108.
23. Zarranz JJ, Alegre J, Gómez-Esteban JC, Lezcano E, Ros R, Ampuero I, Vidal L, Hoenicka J, Rodríguez O, Atarés B, Llorens V, Gomez Tortosa E, del Ser T, Muñoz DG, de Yébenes JG. The new mutation, E46K, of  $\alpha$ -Synuclein causes Parkinson and Lewy body dementia. *Ann Neurol.* 2004;55:164–173.
24. Polymeropoulos MH. Mutation in the  $\alpha$ -Synuclein gene identified in families with Parkinson's disease. *Science.* 1997;276:2045–2047.
25. Lesage S, Anheim M, Letournel F, Bousset L, Honoré A, Rozas N, Pieri L, Madiona K, Dürr A, Melki R, Verny C, Brice A. G51D  $\alpha$ -Synuclein mutation causes a novel Parkinsonian-pyramidal syndrome. *Ann Neurol.* 2013;73:459–471.

## Chapter 1

26. Appel-Cresswell S, Vilarino-Guell C, Encarnacion M, Sherman H, Yu I, Shah B, Weir D, Thompson C, Szu-Tu C, Trinh J, Aasly JO, Rajput A, Rajput AH, Jon Stoessel A, Farrer MJ.  $\alpha$ -Synuclein p.H50Q, a novel pathogenic mutation for Parkinson's disease. *Mov Disord*. 2014;28:811–813.
27. Miake H. Biochemical characterization of the core structure of  $\alpha$ -Synuclein filaments. *J Biol Chem*. 2002;277:19213–19219.
8. Fujiwara H, Hasegawa M, Dohmae N, Kawashima A, Masliah E, Goldberg MS, Shen J, Takio K, Iwatsubo T.  $\alpha$ -Synuclein is phosphorylated in synucleinopathy lesions. *Nat Cell Biol*. 2002;4:160–164.
29. Takahashi M, Kanuka H, Fujiwara H, Koyama A, Hasegawa M, Miura M, Iwatsubo T. Phosphorylation of  $\alpha$ -Synuclein characteristic of synucleinopathy lesions is recapitulated in  $\alpha$ -Synuclein transgenic *Drosophila*. *Neurosci Lett*. 2003;336:155–158.
30. Okochi M, Walter J, Koyama a, Nakajo S, Baba M, Iwatsubo T, Meijer L, Kahle PJ, Haass C. Constitutive phosphorylation of the Parkinson's disease associated  $\alpha$ -Synuclein. *J Biol Chem*. 2000;275:390–397.
31. Shimura H, Schlossmacher M, Hattori, N.Frosch M, Trockenbacher A, Schneider R, Mizuno Y, Kosik KS, Selkoe DJ. Ubiquitination of a new form of  $\alpha$ -Synuclein by parkin from human brain: implications for Parkinson's disease. *Science*. 2001;293:263–269.
32. Hodara R, Norris EH, Giasson BI, Mishizen-Eberz AJ, Lynch DR, Lee VM, Ischiropoulos H. Functional consequences of  $\alpha$ -Synuclein tyrosine nitration: diminished binding to lipid vesicles and increased fibril formation. *J Biol Chem*. 2004;279:47746–47753.
33. Crowther RA, Jakes R, Spillantini MG, Goedert M. Synthetic filaments assembled from C-terminally truncated  $\alpha$ -Synuclein. *FEBS Lett*. 1998;436:309–312.
34. Braithwaite SP, Stock JB, Mouradian MM.  $\alpha$ -Synuclein phosphorylation as a therapeutic target in Parkinson's disease. *Rev Neurosci*. 2012;23:191–198.
35. McFarland MA, Ellis CE, Markey SP, Nussbaum RL. Proteomics analysis identifies phosphorylation-dependent  $\alpha$ -Synuclein protein interactions. *Mol Cell Proteomics*. 2008;7:2123–2137.
36. Clayton DF, George JM. The synucleins: a family of proteins involved in synaptic function, plasticity, neurodegeneration and disease. *Trends Neurosci*. 1998;21:249–

## Chapter 1

- 254.
37. Burré J, Sharma M, Tsetsenis T, Buchman V, Etherton MR, Südhof TC.  $\alpha$ -Synuclein promotes SNARE-complex assembly in vivo and in vitro. *Science*. 2010;329:1663–1667.
  38. Nemani VM, Lu W, Berge V, Nakamura K, Onoa B, Lee MK, Chaudhry FA, Nicoll RA, Edwards RH. Increased expression of  $\alpha$ -Synuclein reduces neurotransmitter release by inhibiting synaptic vesicle reclustering after endocytosis. *Neuron*. 2010;65:66–79.
  39. Vila M, Ramonet D, Perier C. Mitochondrial alterations in Parkinson's disease: new clues. *J Neurochem*. 2008;107:317–328.
  40. Devi L, Raghavendran V, Prabhu BM, Avadhani NG, Anandatheerthavarada HK. Mitochondrial import and accumulation of  $\alpha$ -Synuclein impair complex I in human dopaminergic neuronal cultures and Parkinson disease brain. *J Biol Chem*. 2008;283: 9089–9100.
  41. Devi L, Anandatheerthavarada HK. Mitochondrial trafficking of APP and  $\alpha$ -Synuclein: Relevance to mitochondrial dysfunction in Alzheimer's and Parkinson's diseases. *Biochim Biophys Acta*. 2010;1802:11–19.
  42. Li J, Uversky VN, Fink AL. Effect of familial Parkinson's disease point mutations A30P and A53T on the structural properties, aggregation, and fibrillation of human  $\alpha$ -Synuclein. *Biochemistry*. 2001;40:11604–11613.
  43. Ulmer TS, Bax A. structure and dynamics of micelle-bound human  $\alpha$ -Synuclein. *J Biol Chem*. 2005;280:9595–9603.
  44. Ulmer TS, Bax A. Comparison of structure and dynamics of micelle-bound human  $\alpha$ -Synuclein and Parkinson disease variants. *J Biol Chem*. 2005;280:43179–43187.
  45. Georgieva ER, Ramlall TF, Borbat PP, Freed JH, Eliezer D. The lipid-binding domain of wild type and mutant  $\alpha$ -Synuclein: compactness and interconversion between the broken and extended helix forms. *J Biol Chem*. 2010;285:28261–28274.
  46. Georgieva ER, Ramlall TF, Borbat PP, Freed JH, Eliezer D. Membrane-bound  $\alpha$ -Synuclein forms an extended helix: long-distance pulsed ESR measurements using vesicles, bicelles, and rodlike micelles. *J Am Chem Soc*. 2008;130:12856–12857.
  47. Eliezer D, Kutluay E, Bussell R, Browne G. Conformational properties of  $\alpha$ -Synuclein in its free and lipid-associated states. *J Mol Biol*. 2001;307:1061–1073.

## Chapter 1

48. Dikiy I, Eliezer D. Folding and misfolding of  $\alpha$ -Synuclein on membranes. *Biochim Biophys Acta - Biomembr.* 2012;1818:1013–1018.
49. Haque F, Pandey AP, Cambrea LR, Rochet J-C, Hovis JS. Adsorption of  $\alpha$ -Synuclein on lipid bilayers: modulating the structure and stability of protein assemblies. *J Phys Chem B.* 2010;114:4070–4081.
50. Drescher M, Van Rooijen BD, Veldhuis G, Subramaniam V, Huber M. A stable lipid-induced aggregate of  $\alpha$ -Synuclein. *J Am Chem Soc.* 2010;132:4080–4082.
51. Bekshe Lokappa S, Ulmer TS.  $\alpha$ -Synuclein populates both elongated and broken helix states on small unilamellar vesicles. *J Biol Chem.* 2011;286:21450–21457.
52. Drescher M, Veldhuis G, Van Rooijen BD, Milikisyants S, Subramaniam V, Huber M. Antiparallel arrangement of the helices of vesicle-bound  $\alpha$ -Synuclein. *J Am Chem Soc.* 2008;130:7796–7797.
53. Fusco G, De Simone A, Gopinath T, Vostrikov V, Vendruscolo M, Dobson CM, Veglia G. Direct observation of the three regions in  $\alpha$ -Synuclein that determine its membrane-bound behaviour. *Nat Commun.* 2014;5:1-8.
54. Middleton ER, Rhoades E. Effects of curvature and composition on  $\alpha$ -Synuclein binding to lipid vesicles. *Biophys J.* 2010;99:2279–2288.
55. Rhoades E, Ramlall TF, Webb WW, Eliezer D. Quantification of  $\alpha$ -Synuclein binding to lipid vesicles using fluorescence correlation spectroscopy. *Biophys J.* 2006;90:4692–4700.
56. Drescher M, Godschalk F, Veldhuis G, van Rooijen BD, Subramaniam V, Huber M. Spin-label EPR on  $\alpha$ -Synuclein reveals differences in the membrane binding affinity of the two antiparallel helices. *ChemBioChem.* 2008;9:2411–2416.
57. Jao CC, Hegde BG, Chen J, Haworth IS, Langen R. Structure of membrane-bound  $\alpha$ -Synuclein from site-directed spin labeling and computational refinement. *Proc Natl Acad Sci U S A.* 2008;105:19666–19671.
58. Robotta M, Braun P, van Rooijen B, Subramaniam V, Huber M, Drescher M. Direct evidence of coexisting horseshoe and extended helix conformations of membrane-bound  $\alpha$ -Synuclein. *ChemPhysChem.* 2011;12:267–269.
59. Kumar P, Segers-Nolten IMJ, Schilderink N, Subramaniam V, Huber M. Parkinson's protein  $\alpha$ -Synuclein binds efficiently and with a novel conformation to two natural membrane mimics. *PLoS One.* 2015;10:1-11.

## Chapter 1

60. Robotta M, Hintze C, Schildknecht S, Zijlstra N, Jüngst C, Karreman C, Huber M, Leist M, Subramaniam V, Drescher M. Locally resolved membrane binding affinity of the N-terminus of  $\alpha$ -Synuclein. *Biochemistry*. 2012;51:3960–3962.
61. Robotta M, Gerding HR, Vogel A, Hauser K, Schildknecht S, Karreman C, Leist M, Subramaniam V, Drescher M. Alpha-Synuclein binds to the inner membrane of mitochondria in an  $\alpha$ -helical conformation. *Chembiochem*. 2014;1–4.
62. Högen T, Levin J, Schmidt F, Caruana M, Vassallo N, Kretzschmar H, Botzel K, Kamp F, Giese A. Two different binding modes of  $\alpha$ -Synuclein to lipid vesicles depending on its aggregation state. *Biophys J*. 2012;102:1646–1655.
63. Jao CC, Der-Sarkissian A, Chen J, Langen R. Structure of membrane-bound  $\alpha$ -Synuclein studied by site-directed spin labeling. *Proc Natl Acad Sci U S A*. 2004;101:8331–8336.
64. Bortolus M, Tombolato F, Tessari I, Bisaglia M, Mammi S, Bubacco L, Ferrarini A, Maniero AL. Broken helix in vesicle and micelle-bound  $\alpha$ -Synuclein: insight from site-directed spin labelling-EPR experiments and MD simulations. *J Am Chem Soc*. 2008;130:6690–6691.
65. Anderson JP, Walker DE, Goldstein JM, De Laat R, Banducci K, Caccavello RJ, Barbour R, Huang J, Kling K, Lee M, Diep L, Keim PS, Shen X, Chataway T, Schlossmacher MG, Seubert P, Schenk D, Sinha S, Gai WP, Chilcote TJ. Phosphorylation of Ser-129 is the dominant pathological modification of  $\alpha$ -Synuclein in familial and sporadic Lewy body disease. *J Biol Chem*. 2006;281:29739–29752.
66. Sato H, Kato T, Arawaka S. The role of Ser129 phosphorylation of  $\alpha$ -Synuclein in neurodegeneration of Parkinson's disease: a review of in vivo models. *Rev Neurosci*. 2013;24:115–123.
67. Paleologou KE, Oueslati A, Shakked G, Rospigliosi CC, Kim H-Y, Lamberto GR, Fernandez CO, Schmid A, Chegini F, Gai WP, Chiappe D, Moniatte M, Schneider BL, Aebischer P, Eliezer D, Zweckstetter M, Masliah E, Lashuel HA. Phosphorylation at S87 is enhanced in synucleinopathies, inhibits  $\alpha$ -Synuclein oligomerization, and influences Synuclein-membrane interactions. *J Neurosci*. 2010;30:3184–3198.
68. Goedert M.  $\alpha$ -Synuclein and neurodegenerative diseases. *Nat Rev Neurosci*. 2001;2:492–501.
69. Crowther RA, Daniel SE, Goedert M. Characterisation of isolated  $\alpha$ -Synuclein filaments from substantia nigra of Parkinson's disease brain. *Neurosci Lett*. 2000;292:128–130.

## Chapter 1

70. Fändrich M. On the structural definition of amyloid fibrils and other polypeptide aggregates. *Cell Mol Life Sci.* 2007;64:2066–2078.
71. Jimenez JL, Nettleton EJ, Bouchard M, Robinson C V, Dobson CM, Saibil HR. The protofilament structure of insulin amyloid fibrils. *Proc Natl Acad Sci U S A.* 2002;99:9196–9201.
72. Fändrich M, Meinhardt J, Grigorieff N. Structural polymorphism of Alzheimer A $\beta$  and other amyloid fibrils. *Prion.* 2009;3:89–93.
73. Meinhardt J, Sachse C, Hortschansky P, Grigorieff N, Fändrich M. A $\beta$ (1-40) fibril polymorphism implies diverse interaction patterns in amyloid fibrils. *J Mol Biol.* 2009;386:869–877.
74. Petkova AT, Leapman RD, Guo Z. Self-propagating ,molecular-level polymorphism in Alzheimer 's A $\beta$ -amyloid fibrils. 2005;307:262–265.
75. Heise H, Hoyer W, Becker S, Andronesi OC, Riedel D, Baldus M. Molecular-level secondary structure, polymorphism, and dynamics of full-length  $\alpha$ -Synuclein fibrils studied by solid-state NMR. *Proc Natl Acad Sci U S A.* 2005;102:15871-15876.
76. Weber T, Zemelman BV., McNew JA, Westermann B, Gmachl M, Parlati F, Sollner TH, Rothman JE. SNAREpins: Minimal Machinery for Membrane Fusion. *Cell.* 1998;92:759–772.
77. van den Bogaart G, Jahn R. Insight to membrane fusion. *Proc Natl Acad Sci U S A.* 2011;108:11729–11730.
78. Hashemi Shabestari M. Spin-label EPR on disordered and amyloid proteins. Thesis, Leiden University Repository. 2013.
79. Sutton RB, Fasshauer D, Jahn R, Brunger AT. Crystal structure of a SNARE complex involved in synaptic exocytosis at 2.4 Å resolution. *Nature.* 1998;395:347–353.
80. Jahn R, Lang T, Südhof TC. Membrane Fusion. *Cell.* 2003;112:519–533.
81. Litowski JR, Hodges RS. Designing heterodimeric two-stranded  $\alpha$ -helical coiled-coils. Effect of hydrophobicity and alpha-helical propensity on protein folding, stability, and specificity. *J Biol Chem.* 2002;277:37272–37279.
82. Hubbell WL, Altenbach C. Investigation of structure and dynamics in membrane proteins using site-directed spin labeling. *Curr Opin Struct Biol.* 1994;4:566–573.

## Chapter 1

83. Hubbell WL, Mchaourab HS, Altenbach C, Lietzow MA. Watching proteins move using site-directed spin labeling. *Structure*. 1996;4:779–783.
84. Hubbell WL, Cafiso DS, Altenbach C. Identifying conformational changes with site-directed spin labeling. *Nat Struct Biol*. 2000;7:735–739.
85. Stoll S, Schweiger A. EasySpin, a comprehensive software package for spectral simulation and analysis in EPR. *J Magn Reson*. 2006;178:42–55.
86. Jeschke G. Determination of the Nanostructure of Polymer Materials by Electron Paramagnetic Resonance Spectroscopy. *Macromol Rapid Commun*. 2002;23:227–246.
87. Jeschke G. Distance measurements in the nanometer range by pulse EPR. *ChemPhysChem*. 2002;3:927–932.
88. Jeschke G, Chechik V, Ionita P, Godt A, Zimmermann H, Banham J, Timmel CR, Hilger D, Jung H. DeerAnalysis2006 - a comprehensive software package for analyzing pulsed ELDOR data. *Appl Magn Reson*. 2006;30:473–498.
89. Steigmiller S, Börsch M, Gräber P, Huber M. Distances between the b-subunits in the tether domain of FOF1-ATP synthase from *E. coli*. *Biochim Biophys Acta - Bioenerg*. 2005;1708:143–153.
90. Jeschke G, Koch A, Jonas U, Godt A. Direct conversion of EPR dipolar time evolution data to distance distributions. *J Magn Reson*. 2002;155:72–82.
91. Hilger D, Jung H, Padan E, Wegener C, Vogel KP, Steinhoff HJ, Jeschke G. Assessing oligomerization of membrane proteins by four-pulse DEER: pH-dependent dimerization of NhaA Na<sup>+</sup>/H<sup>+</sup> antiporter of *E. coli*. *Biophys J*. 2005;89:1328–1338.
92. Pasanen P, Myllykangas L, Siitonen M, Raunio A, Kaakkola S, Lyytinen J, Tienari PJ, Pöyhönen M, Paetau A. Novel  $\alpha$ -Synuclein mutation A53E associated with atypical multiple system atrophy and Parkinson's disease-type pathology. *Neurobiol. Aging*. 2014;35:2180.e1-2180.e5.



## **2 Parkinson's Protein $\alpha$ -Synuclein Binds Efficiently and with a Novel Conformation to Two Natural Membrane Mimics**

**Kumar P**, Segers-Nolten IMJ, Schilderink N, Subramaniam V, Huber M. Parkinson's protein  $\alpha$ -Synuclein binds efficiently and with a novel conformation to two natural membrane mimics. *PLOS ONE*, 2015;10:1-11

## Chapter 2

### 2.1 Introduction

Parkinson's disease [1] is the second most prevalent neurodegenerative disorder [2], characterized by the formation of intra-neuronal protein deposits such as Lewy bodies [3] [4]. The protein  $\alpha$ -Synuclein ( $\alpha$ S) is the main component of these protein deposits [5] [6]. The protein  $\alpha$ S consists of 140 amino acids and lacks a defined secondary structure in solution [7] [8]. Its physiological function is still not clear, although  $\alpha$ S has been proposed to play a role in neurotransmitter release [9] [10] and vesicle trafficking [11]. Both these functions involve the neuronal plasma membrane (NPM). The protein  $\alpha$ S is also associated with diseases like dementia, and mitochondrial dysfunction [12] [13] and with aging [14]. In the brain,  $\alpha$ S is present in high concentrations in presynaptic nerve terminals, it has been found to be associated with synaptic vesicles [15], and also in glia. The protein also occurs in mitochondria, especially close to the inner mitochondrial membrane [16][17] and it is thought to be associated with mitochondrial damage [18][19].

When  $\alpha$ S binds to membranes, it attains an amphipathic  $\alpha$ -helical structure from residues 1-100 [20] [21] [22]. The membrane-bound  $\alpha$ -helical  $\alpha$ S forms either a continuous helix (residues 1-100), referred to as the extended helix, or the horseshoe conformation, sometimes also referred to as the broken helix. The horseshoe conformation consists of a helix 1 (residues 3-37), a turn, and a helix 2 (residues 45-92)[23] [24]. Recently a different kink position was suggested [25]. Whether  $\alpha$ S binds in the horseshoe or the extended conformation to membranes is still controversial, with some reports supporting the horseshoe conformation [26] [27] and others the extended conformation [28] [29]. Langen and coworkers reported that subtle changes in lipid composition or membrane structure have strong effects on the conformation of  $\alpha$ S on the membrane [28]. Previously, we

## Chapter 2

found that the extended as well as the horseshoe conformation coexist on large unilamellar vesicles (LUVs) composed of the negatively charged lipid 1-palmitoyl-2-oleoyl-sn-glycero-3-phospho-(1'-rac-glycerol) (POPG) [30]. Here we show that the same is true for small unilamellar vesicles (SUVs).

The affinity of  $\alpha$ S to membranes depends on the negative charge density ( $\rho$ ) of the membrane, where  $\rho$  represents the molar fraction of anionic lipids present in the membrane [31][32][33]. At higher charge density, both  $\alpha$ S helices are tightly bound, but at lower charge density, helix 2 dissociates from the membrane [34].

Since not much is known about the detailed interaction of  $\alpha$ S with natural membranes, we investigated the interaction of  $\alpha$ S with membranes containing lipids that mimic natural membranes. We focus on two membranes [35]: a. the inner mitochondrial membrane (IMM) and b. the neuronal plasma membrane (NPM), presented in the form of small unilamellar vesicles (SUVs). We applied electron paramagnetic resonance (EPR) and investigated the binding of spin-labelled  $\alpha$ S making use of the mobility of the spin label as an indicator for local binding. We focus on two positions, 56 and 69 ( $\alpha$ S56,  $\alpha$ S69), in the helix 2. We also monitor the conformation of  $\alpha$ S on these membranes to determine whether  $\alpha$ S is in the horseshoe or the extended conformation. For these experiments,  $\alpha$ S was spin labelled at two positions, 27 and 56 ( $\alpha$ S27/56), and distances between the spin labels were obtained by DEER (Double Electron-Electron Resonance) [36]. The label positions 27 and 56 were chosen because for these labels both horseshoe and extended conformation yield distances that are measurable by DEER [30].

We show that according to EPR,  $\alpha$ S binds equally well to the two natural membranes IMM and NPM. In spite of the low negative charge density of the IMM and NPM membranes, helix 2 of  $\alpha$ S binds more strongly to these natural

## Chapter 2

membranes than to POPG/POPC model membranes at comparable charge densities. The binding mode differs from what had been observed on model SUVs before. The extended conformation predominates and the second fraction is a horseshoe with a larger opening angle than previously found.

## 2.2 Materials and methods

### 2.2.1 Protein expression and labelling

Mutagenesis, protein expression and purification were performed as described previously [37] [38]. Spin labelling was also done following the standard protocol. Briefly, before starting labelling,  $\alpha$ S cysteine mutants were reduced with a six-fold molar excess per cysteine with DTT (1,4-dithio-D-threitol) for 30 min at room temperature. To remove DTT, samples were passed twice through Pierce Zeba 5 ml desalting columns. Immediately, a ten-fold molar excess of the MTSL spin label [(1-oxy-2,2,5,5-tetramethylpyrroline-3-methyl)-methanethiosulfonate] was added (from a 25 mM stock in DMSO) and incubated for 1 h in the dark at room temperature. After this, free spin label was removed by using two additional desalting steps. Protein samples were applied onto Microcon YM-100 spin columns to remove any precipitated and/or oligomerised proteins and diluted in buffer (10 mM Tris-HCl, pH 7.4). Spin label concentrations for single-cysteine mutants were 2.5 mM and for double-cysteine mutants 5 mM at protein concentrations of 250  $\mu$ M. Owing to the high reactivity of the label and the fact that the cysteine residues are freely accessible in the intrinsically disordered structure, near quantitative labelling can be achieved under these conditions [22]. Samples were stored at -80 °C.

## Chapter 2

### 2.2.2 Preparation of vesicles

The lipid compositions for making SUVs were:

- a. IMM = 1',3'-bis[1,2-dioleoyl-*sn*-glycero-3-phospho]-*sn*-glycerol (CL) : 1-palmitoyl-2-oleoyl-*sn*-glycero-3-phosphoethanolamine (POPE) : 1-palmitoyl-2-oleoyl-*sn*-glycero-3-phosphocholine (POPC) = 4 : 3 : 5 [16]
- b. NPM = L- $\alpha$ -phosphatidylserine (Brain, Porcine) (brain PS) : L- $\alpha$ -phosphatidylethanolamine (Brain, Porcine) (brain PE) : cholesterol (ovine wool) (CH) = 2 : 5 : 3 [39]
- c. POPG SUV's as reference = 100 % 1-palmitoyl-2-oleoyl-*sn*-glycero-3-phospho-(1'-*rac*-glycerol) (POPG)

All lipids were purchased from Avanti Polar Lipids, Inc. as chloroform solutions and were used without further purification. Lipids were mixed in the desired ratio and then chloroform was evaporated by dry nitrogen gas. The resulting lipid films were kept under vacuum overnight. Dried lipid films were hydrated with 10 mM Tris-HCl, pH 7.4 for 1 hour at 30 °C, and the resulting milky lipid suspensions were sonicated for approximately 30 min to make SUVs. The size of the vesicles was determined by dynamic light scattering (DLS). The DLS-experiments were performed on a Zetasizer Nano-ZS (Malvern). We obtained vesicles with a homogeneous size distribution around diameter  $d = 35$  nm (NPM) and 40 nm (IMM and POPG SUVs).

### 2.2.3 Sample Preparation

Aliquots of  $\alpha$ S from stock solutions (concentration between 150  $\mu$ M and 250  $\mu$ M) were added to the SUVs to obtain a lipid to protein ratio (L : P) of 250 : 1, and incubated for 30 min at room temperature before measuring. All samples were prepared and measured at least three times. Frozen samples for continuous wave

## Chapter 2

(cw) low-temperature EPR measurements and distance measurements were prepared using 25 % spin-labelled and 75 % wild type (unlabelled)  $\alpha$ S (diamagnetic dilution). The diamagnetically diluted protein mixtures were mixed with the SUVs at a L : P ratio of 250 : 1 and incubated for 30 min at room temperature. Glycerol (20 % (v/v)) was added to all samples before transferring them into the 3 mm (outer diameter) quartz tubes. The sample tubes were plunged into liquid nitrogen for fast freezing.

### 2.2.4 Continuous wave-EPR experiments

The 9.7 GHz continuous wave (cw) EPR measurements have been performed using a. an EMX PLUS EPR spectrometer (Bruker, Rheinstetten, Germany) with a super high Q cavity (ER 4119 HS-W1) for room temperature measurements and b. an ELEXSYS E680 spectrometer (Bruker, Rheinstetten, Germany) with a rectangular cavity (ER 4102 ST) for low temperature measurements. The room temperature measurements were done at 20 °C, using 0.63 mW of microwave power, 100 kHz modulation frequency and a modulation amplitude of 0.1 mT. Total time to acquire EPR spectra was 20 min. The low-temperature measurements were done at 120 K using a helium gas-flow cryostat (Oxford Instruments, United Kingdom) with an ITC502 temperature controller (Oxford Instruments). The EPR spectra were acquired using a modulation amplitude of 0.25 mT and a microwave power of 0.63 mW.

#### 2.2.4.1 Simulation of cw-EPR spectra

Spectral simulation was performed using Matlab (7.11.0.584, Natick, Massachusetts, U.S.A) and the EasySpin package [40]. For all simulations, the following spectral parameters were used:  $g = [2.00906, 2.00687, 2.00300]$ [41], the hyperfine tensor parameters  $A_{xx} = A_{yy} = 13$  MHz, and the  $A_{zz}$  was varied (see Table

## Chapter 2

2.1). Usually a superposition of more than one component was required to simulate the spectra. The parameters were manually changed to check in which range acceptable simulations of the experimental spectra were obtained to determine the error margins. The rotation correlation time ( $\tau_r$ ) of spin-labelled  $\alpha$ S in solution, i.e., in the absence of the membrane was shown to have an error of  $\pm 0.02$  ns. To simulate spectra of  $\alpha$ S bound to membranes,  $\tau_r$  of the fastest component was kept at the value of the solution spectra of the respective mutant.

### 2.2.5 DEER experiments

All DEER experiments were done at 9.5 GHz on an ELEXSYS E680 spectrometer (Bruker, Rheinstetten, Germany) using a 3 mm split-ring resonator (ER 4118XMS-3-W1). We performed the measurements at 40 K with a helium gas flow using a CF935 cryostat (Oxford Instruments, United Kingdom). The pump and observer frequencies were separated by 70 MHz and adjusted as reported before [26]. The pump-pulse power was adjusted to invert the echo maximally [42]. The pump-pulse length was set to 16 ns. The pulse lengths of the observer channel were 16 and 32 ns for  $\pi/2$ - and  $\pi$  - pulses, respectively. A phase cycle (+ x) - (- x) was applied to the first observer pulse. The complete pulse sequence is given by:  $\frac{\pi}{2}_{\text{obs}} - \tau_1 - \pi_{\text{obs}} - t - \pi_{\text{pump}} - (\tau_1 + \tau_2 - t) - \pi_{\text{obs}} - \tau_2 - \text{echo}$ . The DEER time traces for ten different  $\tau_1$  values spaced by 8 ns starting at  $\tau_1 = 200$  ns were added to suppress proton modulations. Typical accumulation times per sample were 16 hours.

#### 2.2.5.1 DEER Analysis

In order to analyze the DEER traces and extract the distance distributions, the software package “DeerAnalysis 2011” was used [43]. Experimental background

## Chapter 2

functions were derived from DEER traces of membrane-bound singly labelled  $\alpha$ S under conditions of diamagnetic dilution. The distance distribution was derived by the model free Tikhonov regularization [42] [43]. The distance distributions obtained from the Tikhonov regularization were then fitted using two Gaussians. Errors in the amount by which each fraction contributes to the two distances were determined by changing the amplitude of the two Gaussians independently to determine the range which results in an acceptable fit.

### 2.3 Results

To be sure of the integrity of the vesicles, all SUVs were checked by DLS before and after adding  $\alpha$ S. The vesicles were found to have a diameter  $d = 40$  nm for IMM and POPG SUVs and  $d = 35$  nm for NPM, values that did not change upon adding  $\alpha$ S.

#### 2.3.1 Continuous-wave EPR of $\alpha$ S

Figure 2.1a shows the spectra of  $\alpha$ S56 and  $\alpha$ S69 in buffer solution, measured at room temperature. The spectra of  $\alpha$ S56 and  $\alpha$ S69 both consist of three narrow lines. Figure 2.1b and 1c show the spectra of  $\alpha$ S in the presence of IMM and NPM respectively. For both  $\alpha$ S56 and  $\alpha$ S69, the spectral lines are broadened relative to those in Figure 2.1a. The EPR spectrum of  $\alpha$ S56 shows an additional feature, indicated by the arrow in Figure 2.1.

## Chapter 2

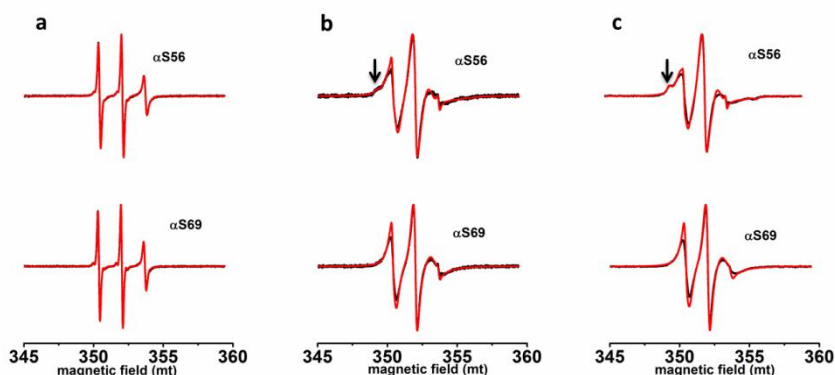


Figure 2.1. Room temperature, solution EPR spectra of  $\alpha$ S56 and  $\alpha$ S69 (a) in buffer, (b) with IMM, (c) with NPM. Black line: experiment, red line: simulation. Arrows show the low-field feature indicating reduced mobility (see text).

More detailed information was obtained by spectral simulation of the experimental spectra, which yields the parameters of mobility of the spin label, the rotation correlation time  $\tau_r$  and, for multicomponent spectra, the amount by which each fraction contributes. These parameters are given in Table 2.1. The solution spectra are simulated with a single component. The  $\tau_r$  of  $\alpha$ S56 is longer than that of  $\alpha$ S69. The spectra of  $\alpha$ S56 bound to the IMM and NPM membranes consist of a superposition of three and those of  $\alpha$ S69 of two components. The  $\tau_r$  of the fast component in all spectra was fixed to the  $\tau_r$  of the respective mutants in solution. The contribution of this fraction to the total spectrum is smaller than 2.5 % for each spectrum. The slow components with  $\tau_r$  values between 2 and 3 ns, contribute at least 87 % and  $\alpha$ S56 additionally has an immobile component in the order of 10 %. The  $\tau_r$  values and contributions for each mutant are the same within the error margin for IMM and NPM.

For comparison, the  $\tau_r$  values for the mutant  $\alpha$ S69 on POPG SUVs (34) are  $0.39 \pm 0.02$  ns (for the fast component) and  $2.9 \pm 0.3$  ns (for the slow component), which is larger than found for the IMM and NPM membranes here. We attribute the

## Chapter 2

reduced motion of the nitroxides on POPG vesicles to stronger binding because of the higher negative charge density of POPG SUVs and other factors, such as differences in head-group structure of lipids.

Table 2.1. Parameters ( $\tau_r$ ) describing the mobility of the spin label of  $\alpha S$  bound to natural membranes from simulations of cw-EPR spectra.  $\tau_r$ : rotation-correlation time,  $A_{zz}$ : the hyperfine splitting along the Z-direction.

condition	$\alpha S$ spin-label positions	fast component			slow component			Immobile component		
		$\tau_r$ (ns)	contribution (%)	$A_{zz}$ (MHz)	$\tau_r$ (ns)	contribution (%)	$A_{zz}$ (MHz)	$\tau_r$ (ns)	contribution (%)	$A_{zz}$ (MHz)
buffer	$\alpha S56$	0.45 $\pm$ 0.02	100	110	na	na	na	na	na	na
	$\alpha S69$	0.31 $\pm$ 0.02	100	110	na	na	na	na	na	na
IMM	$\alpha S56$	0.45	2.0 $\pm$ 0.5	110	2.88 $\pm$ 0.13	90 $\pm$ 1.5	105	>50.0	8.0	92.5
	$\alpha S69$	0.31	2.0 $\pm$ 0.5	110	2.23 $\pm$ 0.11	98 $\pm$ 1.0	104	na	na	na
NPM	$\alpha S56$	0.45	2.0 $\pm$ 0.5	110	2.95 $\pm$ 0.14	88 $\pm$ 1.5	104.5	>50.0	10.0	92.5
	$\alpha S69$	0.31	2.2 $\pm$ 0.3	110	1.99 $\pm$ 0.13	98 $\pm$ 0.3	105	na	na	na

na: not contributing in the simulation. For error determination, see Materials and methods

### 2.3.2 Results of DEER experiments

Figure 2.2 shows the DEER results obtained for  $\alpha$ S27/56 bound to IMM, NPM and POPG SUVs; in Figure 2.2a the raw experimental DEER time traces before the background correction are displayed, in Figure 2.2b the experimental time traces after background correction.

The DEER time traces were analyzed by Tikhonov regularization and the resulting distance distributions are shown in Figure 2.2c (for IMM and NPM) and Figure 2.2d (for POPG SUVs). The DEER traces show modulation, i.e., a periodic oscillation of the echo intensity as a function of the time  $t$ , see for example the maximum around  $1.7 \mu\text{s}$  (Figure 2.2a for  $\alpha$ S on NPM membranes). The oscillation is the Fourier Transform of the frequency of the dipolar coupling between the unpaired electron spins of the two nitroxides. The dipolar coupling reflects the distances between the spins in the ensemble. The shape of the time traces obtained in the experiments is analyzed in terms of the distance distributions. The optimized distance distributions (Figure 2.2c and 2d) result in the fits shown as red lines in Figure 2.2b. Different methods of analysis were tried for  $\alpha$ S on IMM and NPM, revealing that the experimental data is not well reproduced with a single, Gaussian distance distribution. This shows that the data cannot be explained by a single, broad distribution of distances, as would be expected for a continuous spread in conformations.

Considering the two contributions to the distance distributions, the larger intensity contribution is centered at a longer distance and the smaller intensity contribution is centered at a shorter distance. The distance distributions were fitted with two Gaussians, the parameters of which are given in Table 2.2.

## Chapter 2

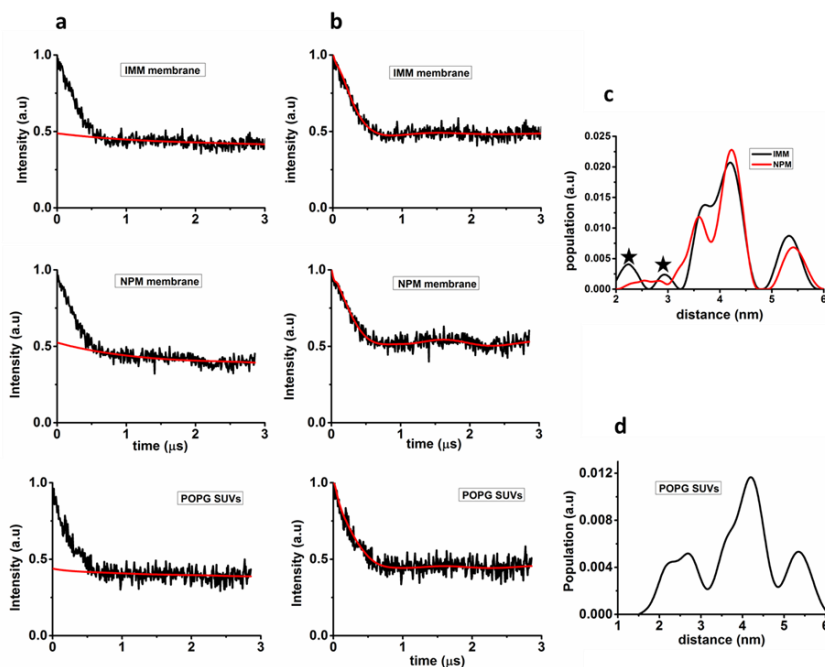


Figure 2.2. DEER time traces and distance distributions for  $\alpha$ S27/56 bound to IMM, NPM and POPG SUVs. (a) Time trace before background correction (black line), red line: background. (b) Time trace after background correction (black line), red line: fit of the time trace with the distance distributions shown in c. (c) Distance distribution obtained after Tikhonov regularization of  $\alpha$ S27/56 bound to IMM (black line) and NPM (red line). (d) Distance distribution obtained after Tikhonov regularization of  $\alpha$ S27/56 bound to POPG SUVs. For comparison, the same regularization parameter ( $\alpha = 100$ ) was used for c and d, which seems to be on the small side for d. The peak at 2.6 nm in Figure 2.2d is related to the horseshoe conformation on POPG SUVs. Small peaks shown with asterisks in Figure 2.2c have negligible contribution to the distance distribution according to the suppression tool in DEER analysis, the feature at 5.5 nm in all distributions is related to a background artefact and not relevant.

## Chapter 2

Table 2.2. Parameters of distance distributions for  $\alpha$ S27/56 bound to SUVs of IMM and NPM and model membranes for comparison

SUVs mimicking natural membranes				POPG SUVs		POPG LUVs	
IMM		NPM				[30]*	
distance (nm)	fraction (%)	distance (nm)	fraction (%)	distance (nm)	fraction (%)	distance (nm)	fraction (%)
3.7	32	3.6	36	2.6	30	2.7	27
4.2	68	4.3	64	4.2	70	4.3	73

Errors in contribution to fraction  $\pm 3$  % (IMM and NPM) and  $\pm 2$  % (POPG SUVs)

\*reanalyzed from ref. (30)

## 2.4 Discussion

In this study, we investigate the binding of  $\alpha$ S to natural membranes by spin-label EPR. The membrane is presented in the form of SUVs, composed of lipids that mimic the natural membranes IMM and NPM. To check the binding of helix 2 of  $\alpha$ S to these membranes, cw-EPR at room temperature was performed with spin-label positions representative of helix 2 binding, positions 56 and 69. All spectra reveal clear changes in lineshape in the presence of IMM and NPM showing that  $\alpha$ S interacts with these membranes. The spectra and the spectral lineshape simulation parameters (given in Table 2.1) of  $\alpha$ S on IMM and NPM agree within experimental uncertainty, showing that the interaction of  $\alpha$ S with both membranes is similar. The fast fraction of  $\alpha$ S spin labelled at position 56 and 69 is below 2.5 % (Table 2.1), which shows that helix 2 is firmly bound to the membrane.

When considering only the relatively small negative charge density ( $\rho$ ) of the membranes investigated, IMM ( $\rho = 0.3$ ) and NPM ( $\rho = 0.2$ ), the tight binding of helix 2 is surprising, since on model membranes studied previously,  $\alpha$ S binding is strongest with vesicles composed exclusively of anionic phospholipids ( $\rho = 1$ )

## Chapter 2

[20][33][44]. On SUVs of mixtures of zwitterionic and anionic lipids with a charge density of  $\rho = 0.26$ , which is comparable to IMM and NPM membranes, the local degree of binding of  $\alpha S$ , when monitored at spin label position 69 of helix 2 is even so low that the bound fraction is too small to be reliably detected by EPR [34]. Therefore, other factors than membrane charge must be responsible for the binding behavior of  $\alpha S$ . Several studies have shown such effects [44][45][46][47]. In the present case, the specific lipid composition, for example the CL content must play a role, as already shown by Zigoneanu et al.[45] and Robotta et al.[46]. The lipid CL has a very small head group area compared to the head group of other synthetic lipids such as POPC and POPG, along with a tail region, which consists of four acyl chains. Why this inverted-cone-shaped lipid promotes  $\alpha S$  binding is presently unclear, however, it is a likely candidate to promote binding of  $\alpha S$  on our IMM SUVs as well. This could be tested by measurements on membranes with different amounts of CL as done in ref. [45] and [46]. The second natural membrane we investigated, NPM, does not contain CL, and it is not clear what causes binding comparable to that for IMM mimics. Besides membrane charge and CL content, several other factors, for example, membrane phase, lipid saturation [27] and posttranslational modification of  $\alpha S$  [47] were shown to influence the affinity of  $\alpha S$  to the membrane.

The distances measured by DEER report on the conformation of  $\alpha S$  on the membranes. As in the binding studies, the results of the DEER experiments are similar for IMM and NPM, showing that also the conformation of  $\alpha S$  is similar on both membranes. As described in the results section, a two-peaked distance distribution fits the data better than a single component, showing that there are two distinct conformations of  $\alpha S$ . The long-distance component agrees well with the distance attributed to the extended conformation (Table 2.2). On IMM and on

## Chapter 2

NPM SUVs, this is the major fraction, which also reveals that more than half of the  $\alpha$ S binds to the membrane in the extended conformation. The second fraction has a shorter distance, a distance that is too short for an extended helix conformation. However, the distance is longer than that of the  $\alpha$ S horseshoe conformation on micelles (2.7 nm) [23], on SUVs (shown in Figure 2.2d and Table 2.2), and on LUVs [30]. The helix 2 appears to be firmly bound, so this fraction cannot be due to a flexible helix 2 section of the protein, and the DLS results show that the SUVs are intact in the presence of  $\alpha$ S. Therefore, we attribute this form to a horseshoe-like conformation with a larger opening angle than the horseshoe conformation found on SDS micelles or POPG SUVs and LUVs (Table 2.2). The molecular interactions leading to this conformation is not clear, and why it is stabilized by the natural-membrane mimics is difficult to answer. The distance between the helices is too large to enable intramolecular interactions of the sidechains of the helix residues. Specific turn configurations of the residues linking the two helices [48], protein-membrane interactions or the formation of  $\alpha$ S-aggregates on the membrane have been discussed as factors leading to the horseshoe conformation, however, so far no conclusive interpretation has been found.

To characterize this novel form in detail, distances between more spin-label pairs would be useful, studies we are planning in the future.

The larger-opening-angle horseshoe conformation is another example of the variability in  $\alpha$ S-membrane interaction. The tight binding of  $\alpha$ S to the natural membrane-mimics again emphasizes that  $\alpha$ S is perfectly suited to interact with such membranes, suggesting that the co-localization and the presumed function may very likely involve these membranes.

## Chapter 2

### 2.5 References

1. Parkinson J. An Essay on the Shaking Palsy (Whitingham and Rowland, London). 1817.
2. De Rijk MC, Breteler MM, Graveland GA, Ott A, Grobbee DE, van der Meché FG, Hofman A. Prevalence of Parkinson's disease in the elderly: the Rotterdam Study. *Neurology*. 1995;45:2143–2146.
3. Junn E, Ronchetti RD, Quezado MM, Kim S-Y, Mouradian MM. Tissue transglutaminase-induced aggregation of  $\alpha$ -Synuclein: Implications for Lewy body formation in Parkinson's disease and dementia with Lewy bodies. *Proc Natl Acad Sci U S A*. 2003;100:2047–2052.
4. Chung KK, Zhang Y, Lim KL, Tanaka Y, Huang H, Gao J, Ross CA, Dawson VL, Dawson TM. Parkin ubiquitinates the alpha-synuclein-interacting protein, synphilin-1: Implications for Lewy-body formation in Parkinson disease. *Nat Med*. 2001;7:1144–1150.
5. Spillantini MG, Schmidt ML, Lee VM, Trojanowski JQ, Jakes R, Goedert M.  $\alpha$ -Synuclein in Lewy bodies. *Nature*. 1997;388:839–840.
6. Goedert M.  $\alpha$ -Synuclein and neurodegenerative diseases. *Nat Rev Neurosci*. 2001;2: 492–501.
7. Weinreb PH, Zhen W, Poon AW, Conway KA, Lansbury PT. NACP, a protein implicated in Alzheimer's disease and learning, is natively unfolded. *Biochemistry*. 1996;35:13709–13715.
8. Uversky VN. Protein folding revisited. A polypeptide chain at the folding-misfolding- nonfolding cross-roads: which way to go? *Cell Mol Life Sci*. 2003;60:1852–1871.
9. Liu S, Ninan I, Antonova I, Battaglia F, Trinchese F, Narasanna A, Kolodilov N, Dauer W, Hawkins RD, Arancio O.  $\alpha$ -Synuclein produces a long-lasting increase in neurotransmitter release. *EMBO J*. 2004;23:4506–4516.
10. Maroteaux L, Campanelli JT, Scheller RH. Synuclein: a neuron-specific protein localized to the nucleus and presynaptic nerve terminal. *J Neurosci*. 1988;8:2804–2815.

## Chapter 2

11. Nemani VM, Lu W, Berge V, Nakamura K, Onoa B, Lee MK, Chaudhry FA, Nicoll RA, Edwards RH. Increased expression of  $\alpha$ -Synuclein reduces neurotransmitter release by inhibiting synaptic vesicle reclustering after endocytosis. *Neuron*. 2010;65:66–79.
12. Vila M, Ramonet D, Perier C. Mitochondrial alterations in Parkinson's disease: New clues. *J Neurochem*. 2008;107:317–328.
13. Devi L, Anandatheerthavarada HK. Mitochondrial trafficking of APP and  $\alpha$ -Synuclein: Relevance to mitochondrial dysfunction in Alzheimer's and Parkinson's diseases. *Biochim Biophys Acta*. 2010;1802:11–19.
14. Burré J, Sharma M, Tsetsenis T, Buchman V, Etherton MR, Südhof TC.  $\alpha$ -Synuclein promotes SNARE-complex assembly in vivo and in vitro. *Science*. 2010;329:1663–1667.
15. Kubo SI, Nemani VM, Chalkley RJ, Anthony MD, Hattori N, Mizuno Y, Edwards RH, Fortin DL. A combinatorial code for the interaction of  $\alpha$ -Synuclein with membranes. *J Biol Chem*. 2005;280:31664–31672.
16. Ardail D, Privat JP, Egret-Charlier M, Levrat C, Lerme F, Louisot P. Mitochondrial contact sites. Lipid composition and dynamics. *J Biol Chem*. 1990;265:18797–18802.
17. Devi L, Raghavendran V, Prabhu BM, Avadhani NG, Anandatheerthavarada HK. Mitochondrial import and accumulation of  $\alpha$ -Synuclein impair complex I in human dopaminergic neuronal cultures and Parkinson disease brain. *J Biol Chem*. 2008;283: 9089–9100.
18. Nakamura K, Nemani VM, Azarbal F, Skibinski G, Levy JM, Egami K, Munishkina L, Zhang J, Gardner B, Wakabayashi J, Sesaki H, Cheng Y, Finkbeiner S, Nussbaum RL, Masliah E, Edwards RH. Direct membrane association drives mitochondrial fission by the Parkinson's disease-associated protein  $\alpha$ -Synuclein. *J Biol Chem*. 2011;286:20710–20726.
19. Yong-Kee CJ, Sidorova E, Hanif A, Perera G, Nash JE. Mitochondrial dysfunction precedes other sub-cellular abnormalities in an in vitro model linked with cell death in Parkinson's disease. *Neurotox Res*. 2012;21:185–194.
20. Davidson WS, Jonas A, Clayton DF, George JM. Stabilization of  $\alpha$ -Synuclein secondary structure upon binding to synthetic membranes. *J Biol Chem*. 1998;273:9443–9449.

## Chapter 2

21. Eliezer D, Kutluay E, Bussell R, Browne G. Conformational properties of  $\alpha$ -Synuclein in its free and lipid-associated states. *J Mol Biol.* 2001;307: 1061–1073.
22. Jao CC, Der-Sarkissian A, Chen J, Langen R. Structure of membrane-bound  $\alpha$ -Synuclein studied by site-directed spin labelling. *Proc Natl Acad Sci U S A.* 2004;101:8331–8336.
23. Ulmer TS, Bax A. structure and dynamics of micelle-bound human  $\alpha$ -Synuclein. *J Biol Chem.* 2005;280:9595–9603.
24. Ulmer TS, Bax A. Comparison of structure and dynamics of micelle-bound human  $\alpha$ -Synuclein and Parkinson disease variants. *J Biol Chem.* 2005;280:43179–43187.
25. Shvadchak V V., Subramaniam V. A four-amino acid linker between repeats in the  $\alpha$ -Synuclein sequence is important for fibril formation. *Biochemistry.* 2014;53:279–281.
26. Drescher M, Veldhuis G, Van Rooijen BD, Milikisyants S, Subramaniam V, Huber M. Antiparallel arrangement of the helices of vesicle-bound  $\alpha$ -Synuclein. *J Am Chem Soc.* 2008;130:7796–7797.
27. Lokappa SB, Ulmer TS. Alpha-synuclein populates both elongated and broken helix states on small unilamellar vesicles. *J Biol Chem.* 2011;286: 21450–21457.
28. Jao CC, Hegde BG, Chen J, Haworth IS, Langen R. Structure of membrane-bound  $\alpha$ -Synuclein from site-directed spin labelling and computational refinement. *Proc Natl Acad Sci U S A U S A.* 2008;105:19666–19671.
29. Georgieva ER, Ramlall TF, Borbat PP, Freed JH, Eliezer D. Membrane-bound  $\alpha$ -Synuclein forms an extended helix: long-distance pulsed ESR measurements using vesicles, bicelles, and rodlike micelles. *J Am Chem Soc.* 2008;130:12856–12857.
30. Robotta M, Braun P, Van Rooijen B, Subramaniam V, Huber M, Drescher M. Direct evidence of coexisting horseshoe and extended helix conformations of membrane-bound  $\alpha$ -Synuclein. *ChemPhysChem.* 2011;12:267–269.
31. Robotta M, Hintze C, Schildknecht S, Zijlstra N, Jüngst C, Karreman C, Huber M, Leist M, Subramaniam V, Drescher M. Locally resolved membrane binding affinity of the N-terminus of  $\alpha$ -Synuclein. *Biochemistry.* 2012;51:3960–3962.
32. Middleton ER, Rhoades E. Effects of curvature and composition on  $\alpha$ -Synuclein binding to lipid vesicles. *Biophys J.* 2010;99:2279–2288.

## Chapter 2

33. Rhoades E, Ramlall TF, Webb WW, Eliezer D. Quantification of  $\alpha$ -Synuclein binding to lipid vesicles using fluorescence correlation spectroscopy. *Biophys J*. 2006;90:4692–4700.
34. Drescher M, Godschalk F, Veldhuis G, van Rooijen BD, Subramaniam V, Huber M. Spin-label EPR on  $\alpha$ -Synuclein reveals differences in the membrane binding affinity of the two antiparallel helices. *ChemBioChem*. 2008;9:2411–2416.
35. Stefanovic AND, Stöckl MT, Claessens MMAE, Subramaniam V.  $\alpha$ -Synuclein oligomers distinctively permeabilize complex model membranes. *FEBS J*. 2014;281:2838–2850.
36. Milov AD, Tsvetkov YD. Double electron-electron resonance in electron spin echo: Conformations of spin-labelled poly-4-vinilpyridine in glassy solutions. *Applied Magnetic Resonance*. 1997;12:495–504.
37. Van Raaij ME, Segers-Nolten IMJ, Subramaniam V. Quantitative morphological analysis reveals ultrastructural diversity of amyloid fibrils from  $\alpha$ -Synuclein mutants. *Biophys J*. 2006;91:L96–L98.
38. Veldhuis G, Segers-Nolten I, Ferlemann E, Subramaniam V. Single-molecule FRET reveals structural heterogeneity of SDS-bound  $\alpha$ -Synuclein. *ChemBioChem*. 2009;10:436–439.
39. Van Meer G, Voelker DR, Feigenson GW. Membrane lipids: where they are and how they behave. *Nat Rev Mol Cell Biol*. 2008;9:112–124.
40. Stoll S, Schweiger A. EasySpin, a comprehensive software package for spectral simulation and analysis in EPR. *J Magn Reson*. 2006;178:42–55.
41. Steigmiller S, Börsch M, Gräber P, Huber M. Distances between the b-subunits in the tether domain of F<sub>0</sub>F<sub>1</sub>-ATP synthase from *E. coli*. *Biochim Biophys Acta - Bioenerg*. 2005;1708:143–153.
42. Jeschke G. Distance measurements in the nanometer range by pulse EPR. *ChemPhysChem*. 2002;3:927–932.
43. Jeschke G, Chechik V, Ionita P, Godt A, Zimmermann H, Banham J, Timmel CR, Hilger D, Jung H. DeerAnalysis2006 - a comprehensive software package for analyzing pulsed ELDOR data. *Appl Magn Reson*. 2006;30:473–498.
44. Jo E, McLaurin JA, Yip CM, George-Hyslop PS, Fraser PE.  $\alpha$ -Synuclein Membrane Interactions and Lipid Specificity. *J Biol Chem*. 2000;275:34328–34334.

## Chapter 2

45. Zigoneanu IG, Yang YJ, Krois AS, Haque ME, Pielak GJ. Interaction of  $\alpha$ -Synuclein with vesicles that mimic mitochondrial membranes. *Biochim Biophys Acta - Biomembr.* 2012;1818:512–519.
46. Robotta M, Gerding HR, Vogel A, Hauser K, Schildknecht S, Karreman C, Leist M, Subramaniam V, Drescher M.  $\alpha$ -Synuclein binds to the inner membrane of mitochondria in an  $\alpha$ -helical conformation. *Chembiochem.* 2014;1–4.
47. Dikiy I, Eliezer D. N-terminal Acetylation stabilizes N-terminal Helicity in Lipid- and Micelle-bound  $\alpha$ -Synuclein and increases its affinity for Physiological Membranes. *J Biol Chem.* 2014;289:3652–3665.
48. Bortolus M, Tombolato F, Tessari I, Bisaglia M, Mammi S, Bubacco L, Ferrarini A, Maniero AL. Broken helix in vesicle and micelle-bound  $\alpha$ -Synuclein: Insight from site-directed spin labelling-EPR experiments and MD simulations. *J Am Chem Soc.* 2008;130:6690–6691.

## **3 Membrane Binding of Parkinson's Protein $\alpha$ -Synuclein: Effect of Phosphorylation at Positions 87 and 129**

**Kumar P**, Schilderink N, Subramaniam V, Huber M. Membrane binding of Parkinson's protein  $\alpha$ -Synuclein: Effect of phosphorylation at positions 87 and 129 by the S to D mutation approach. *Israel Journal of Chemistry*, 2016; DOI: 10.1002/ijch.201600083

## Chapter 3

### 3.1 Introduction

Parkinson's disease (1) is the second most spread neurodegenerative disease after the Alzheimer's disease (2). This disease is characterized by the formation of protein deposits such as Lewy bodies in the brain (3,4). The protein  $\alpha$ -Synuclein ( $\alpha$ S) constitutes the main component of these deposits (5–7). A number of post-translational modifications of  $\alpha$ S are present within the Lewy bodies in Parkinson's disease (PD) and related disorders (8,9). The major disease-associated post-translational modifications (PTMs) are phosphorylation (8,10), truncation, ubiquitination (11) and also oxidation (like nitration) (12). Phosphorylation is the most studied PTM among them.

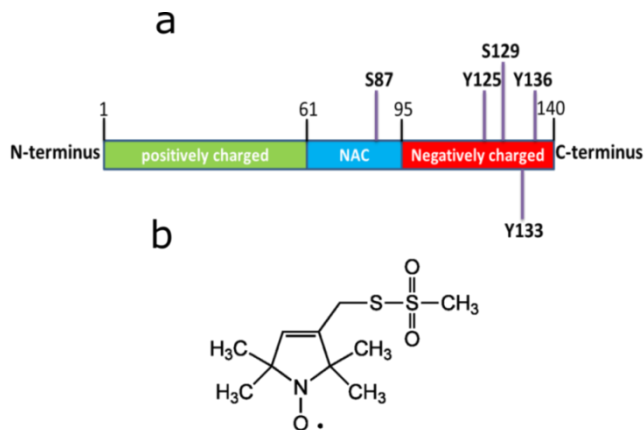


Figure 3.1. a. The most common phosphorylation sites in  $\alpha$ S. Given is the sequence number (in boldface) preceded by the residue (Y or S) that is phosphorylated. Also, the important regions of the protein are shown, indicated by sequence numbers at start and stop. Positively charged (green): Net positive charge of protein between residues 1 and 61, NAC – non-amyloid- $\beta$  component (blue), and negatively charged C-terminal part of the protein (red), from residue 95 onwards; b. chemical structure of the spin label MTSL, by which Cys is labelled.

The protein  $\alpha$ S has been found hyperphosphorylated in Lewy bodies and Lewy neurites (1,9,13). The role of phosphorylation of  $\alpha$ S in neurotoxicity is

### Chapter 3

controversial. However, growing evidence suggests that phosphorylation could influence membrane/vesicle binding of  $\alpha$ S and its aggregation(8,14–17). Recent reviews summarize results of in vivo and in vitro studies and describe to which degree phosphorylation of  $\alpha$ S is linked to disease (18,19). The major phosphorylation sites of  $\alpha$ S are shown in Figure 3.1.

The phosphorylation sites Y125, S129, Y133, and Y136 are most discussed in the literature, for example S129 is highly phosphorylated in Lewy bodies. One more phosphorylation site is special, S87, since it distinguishes the human  $\alpha$ S sequence from that of mouse and rat (13). Also, a link between phosphorylation at site 87 and disease was discussed by Paleologou *et al.* (13).

Here we focus on the membrane-binding aspect of  $\alpha$ S phosphorylation in vitro at positions S87 and S129. Membrane-binding of  $\alpha$ S concerns an amphipathic helix spanning residues from 1-100 (20–22). The N-terminal half (residues 1-50) of the amphipathic helix is termed helix 1, and the other half (residues 51-100), helix 2. The affinity of  $\alpha$ S to membranes depends on the negative charge density ( $\rho$ ) of the membrane, where  $\rho$  represents the molar fraction of anionic lipids present in the membrane (23). Different binding properties were found for helix 1 and helix 2 (24).

There are three ways to generate protein constructs to study the effect of phosphorylation: a. to phosphorylate the respective residues enzymatically, which requires dedicated enzymes/ overexpression systems (25,26) and is reversible, b. by a semisynthetic approach in which a (phosphorylated) peptide is linked to the corresponding overexpressed protein (27), and c. by generating mutants whose side chains mimic the chemical properties of the phosphorylated state (negative charge) and size, sometimes referred to as pseudophosphorylation (28). Typically,

### Chapter 3

serine (S) is replaced by aspartate (D) or glutamate (E) (13,17,29,30) to mimic phosphorylation and alanine (A) is used as reference for the non-phosphorylated state, especially for in vivo studies.

All three approaches have been used to study  $\alpha$ S-phosphorylation in vivo and in vitro, showing that in some cases, enzymatically phosphorylated  $\alpha$ S (P- $\alpha$ S) and pseudophosphorylated  $\alpha$ S behave differently (29,31). For example, enzymatic phosphorylation of  $\alpha$ S at S129 has been shown to have an inhibitory effect on  $\alpha$ S-aggregation, while pseudophosphorylation does not show such an effect (29). Apparently, the different behavior depends strongly on the properties probed and the environment  $\alpha$ S is exposed to. In the present study we focus on the phosphomimic approach with the S $\rightarrow$ D substitution to mimic phosphorylation, and investigate the constructs S87A or S129A : non-phosphorylated; S87D or S129D : phosphorylated.

We used large unilamellar vesicles (LUVs) (see appendix A) as membrane models with a 1:1 mixture of the lipids 1-palmitoyl-2-oleoyl-*sn*-glycero-3-phospho-(1'-rac-glycerol) (POPG) and 1-palmitoyl-2-oleoyl-*sn*-glycero-3-phosphocholine (POPC), generating a membrane with a charge density  $\rho = 0.5$ . Previous studies on model membranes showed that at high charge densities, i.e., above 0.8 – 0.9,  $\alpha$ S is fully bound to those membranes (23,24,32–34), revealing that the interaction is strong and dominated by electrostatics, which risks to mask the effects of phosphorylation. Additionally, such charge densities are non-physiological, so we avoided these high negative charge densities. At low charge densities ( $\rho \leq 0.2$ ), i.e., on neutral or weakly negatively charged membranes, binding is very low, resulting in a large fraction of unbound protein, which would also abolish any differential binding effect of phosphorylation. This made  $\rho = 0.5$  an optimum charge density to work at.

### Chapter 3

To investigate membrane binding, we used spin label Electron Paramagnetic Resonance (EPR) spectroscopy. For spin labelling, the amino-acid residue at the sequence position of interest is replaced by a cysteine, which is reacted with a suitable functional group of the nitroxide spin label (see Fig. 1b), an approach introduced by the Hubbell group (35). In this way, a nitroxide, which contains an unpaired electron and is therefore EPR active, is covalently attached to the protein. Then the properties of the protein can be probed at the modified position by EPR. In the present study, we make use of the ability of EPR to detect the mobility of the spin label by room-temperature, continuous-wave (cw) EPR. Characteristic lineshapes of the spectra reveal the mobility of the spin label, with narrow lines corresponding to fast motion (i.e., rotational correlation times ( $\tau_r$ ) of several hundreds of ps) and broad lines to slow motion, in the ns-regime. In our particular case, slow motion of the spin label shows that the section of the protein to which the spin label is attached is bound to the membrane, whereas fast motion shows detachment of the protein from the membrane. The methodology described was introduced before and has proven valuable to determine the local binding of  $\alpha$ S to membranes (24,32–34).

The spin-labelled constructs are referred to as *SLposition* $\alpha$ S/S87A(D) or *SLposition* $\alpha$ S/S129A(D), such that for example, *SL27* $\alpha$ S/S87D is the construct with the spin label at position 27 and is the phosphorylated variant at position 87. We investigated several spin-label positions for each phosphorylation site, resulting in a total of nine constructs, summarized in Table 3.1.

In this work, we show how phosphorylation affects the binding of  $\alpha$ S to the membrane. It decreases the binding of  $\alpha$ S to the membrane when phosphorylated at the S87 position, whereas no effect is seen when phosphorylated at the S129 position. We also show that phosphorylation at position 87 does not detach the

## Chapter 3

protein completely from the membrane, but rather causes local unbinding, which is particularly pronounced in the helix 2 region.

### 3.2 Materials and methods

#### 3.2.1 Protein expression and labelling

All  $\alpha$ S mutants were expressed in *Escherichia coli* strain BL21(DE3) using the pT7-7 expression plasmid and purified in the presence of 1 mM DTT as previously reported(36,37) Serine-87 is substituted either by Alanine (S87A, represents phosphorylation- inactive form) or by Aspartate (S87D, represents phosphomimic form). For labelling, a cysteine mutation was introduced at the desired residues.

Spin labelling was done following the standard protocol, described briefly. Before starting labelling,  $\alpha$ S cysteine mutants were reduced with a six-fold molar excess per cysteine with DTT (1,4-dithio-D-threitol) for 30 min at room temperature. To remove DTT, samples were passed through a Pierce Zeba 5 ml desalting column. Immediately, a ten-fold molar excess of the MTSL spin label [(1-oxyl-2,2,5,5-tetramethylpyrroline-3-methyl)-methanethiosulfonate] was added (from a 25 mM stock in DMSO) and incubated for 1 h in the dark at room temperature. After this, free spin label was removed by using two additional desalting steps. Protein samples were applied onto Microcon YM-100 spin columns to remove any precipitated and/or oligomerised proteins and diluted in buffer (10 mM Tris-HCl, pH 7.4). Spin label concentrations were 2.5 mM at protein concentrations of 250  $\mu$ M. Owing to the high reactivity of the label and the fact that the cysteine residues are freely accessible in the poorly folded structure, near quantitative labelling can be achieved under these conditions(38). Samples were stored at -80 °C.

## Chapter 3

### 3.2.2 Preparation of vesicles

All lipids were purchased from Avanti Polar Lipids, Inc. as chloroform solutions and were used without further purification. LUVs were prepared from 1 : 1 mixtures of 1-palmitoyl-2-oleoyl-*sn*-glycero-3-phospho-(1'-*rac*-glycerol) (POPG) and 1-palmitoyl-2-oleoyl-*sn*-glycero-3-phosphocholine (POPC). Lipids were mixed in the desired ratio and then chloroform was evaporated by dry nitrogen gas. The resulting lipid films were kept under vacuum overnight. Dried lipid films were hydrated with 10 mM Tris – HCl, pH 7.4 for 1 hour at 30 °C, and the resulting milky lipid suspensions were extruded through 100 nm pore size polycarbonated membranes using the mini extruder (catalogue no. 610000) from Avanti Polar Lipids. The size of the vesicles was determined by dynamic light scattering (DLS). The DLS-experiments were performed on a Zetasizer Nano-ZS (Malvern). We obtained vesicles with a homogeneous size distribution around diameter  $d = 100$  nm.

### 3.2.3 Sample Preparation

Spin-labelled  $\alpha$ S mutants were added from stock solutions (concentration between 150  $\mu$ M and 250  $\mu$ M) to the LUVs to obtain a lipid to protein ratio (L : P) of 250 : 1, and incubated for 30 min at room temperature before measuring. All samples were prepared and measured at least three times. All spin labelled  $\alpha$ S constructs used in this work are shown in Table 3.1.

### 3.2.4 Filtration experiments

To determine, whether  $\alpha$ S physically detaches from the membrane, we performed filtration experiments similar to those described in Drescher et. al (24). An  $\alpha$ S-vesicle solution, prepared as for the EPR experiments described above

### Chapter 3

(sample preparation), was passed through a 100 kDa cut-off filter device (Amicon Ultra 100k), which retains the vesicles and thereby the membrane-bound  $\alpha$ S fraction, but is permeable for unbound  $\alpha$ S. The concentration of  $\alpha$ S in the filtrate is too low to measure directly, therefore the filtrate was concentrated using a 3 kDa cut-off filter device (Amicon Ultra 3k) and measured by EPR to determine the amount of  $\alpha$ S in the filtrate. The error in the final value, in the order of 20 %, derives largely from the errors in determining the volumes before and after the concentration step, and the error of the double integral procedure to determine the spin concentration by EPR.

Table 3.1. The  $\alpha$ S constructs used to study phosphorylation at position S87 and S129; SL denotes the spin-label.

<b>Spin label positions</b>	<b>S87A (non-phosphorylated)</b>	<b>S87D (phosphorylated)</b>
<b>SL27</b>	SL27 $\alpha$ S/S87A	SL27 $\alpha$ S/S87D
<b>SL56</b>	SL56 $\alpha$ S/S87A	SL56 $\alpha$ S/S87D
<b>SL63</b>	SL63 $\alpha$ S/S87A	SL63 $\alpha$ S/S87D
<b>SL69</b>	SL69 $\alpha$ S/S87A	SL69 $\alpha$ S/S87D
<b>SL76</b>	SL76 $\alpha$ S/S87A	SL76 $\alpha$ S/S87D
<b>SL90</b>	SL90 $\alpha$ S/S87A	SL90 $\alpha$ S/S87D
<b>Spin label positions</b>	<b>S129A (non-phosphorylated)</b>	<b>S129D (phosphorylated)</b>
<b>SL27</b>	SL27 $\alpha$ S/S129A	SL27 $\alpha$ S/S129D
<b>SL56</b>	SL56 $\alpha$ S/S129A	SL56 $\alpha$ S/S129D
<b>SL69</b>	SL69 $\alpha$ S/S129A	SL69 $\alpha$ S/S129D

### 3.2.5 Continuous wave-EPR experiments

The 9.7 GHz continuous-wave (cw) EPR measurements have been performed using an ELEXSYS E680 spectrometer (Bruker, Rheinstetten, Germany) with a Super high Q cavity (ER 4122 SHQE-W1/1108). Measurements were performed at

## Chapter 3

20 °C, using 0.63 mW of microwave power, 100 kHz modulation frequency and a modulation amplitude of 0.1 mT. Total acquisition time for the EPR spectra was 20 minutes.

### 3.2.5.1 Simulation of cw-EPR spectra

Spectral simulations were performed using Matlab (7.11.0.584, Natick, Massachusetts, U.S.A) and the EasySpin package(39). For all simulations, the following spectral parameters were used:  $g = [2.00906, 2.00687, 2.00300]$  (40), the hyperfine tensor parameters  $A_{xx} = A_{yy} = 13$  MHz, and  $A_{zz}$  was varied (see Table 3.2). Usually a superposition of more than one component was required to simulate the spectra. The parameters were manually changed to check in which range acceptable simulations of the experimental spectra were obtained to determine the error margins. To simulate spectra of  $\alpha$ S bound to membranes, the  $\tau_r$  of the fastest component was kept at the  $\tau_r$  value of the spectra of the respective protein construct in the absence of vesicles.

## 3.3 Results

We investigate the binding of phosphorylation variants of  $\alpha$ S at positions 87 and 129 to LUVs of 100 nm diameter. The LUVs are composed of a 1:1 mixture of POPG and POPC, generating a membrane of charge density  $\rho = 0.5$ . We first describe the results of phosphorylation at position 87, then at 129.

Figure 3.2 shows the spectra of the spin labelled constructs probing phosphorylation at position 87 in the presence of LUVs (for complete list of constructs, see Table 3.1). In this set, helix 1 is probed in the middle, at residue 27, helix 2 is probed at five positions starting from position 56 and terminating in 90. Figure 3.22a shows the spectra of  $\alpha$ S in the non-phosphorylated and Figure 3.2b

### Chapter 3

in the phosphorylated form. Spectra in Figure 3.2a differ from those in Figure 3.2b, most notably, each spectrum in Figure 3.2b has narrower lines than its counterpart in Figure 3.2a. As described in the introduction, narrow lines derive from spin-labels that are rotating fast. As discussed in more detail below, fast rotation shows that the section of the protein to which the spin label is attached is not bound to the membrane. More detailed information was obtained by spectral simulation of the experimental spectra, which yields the parameters of mobility of the spin label, the rotational correlation time ( $\tau_r$ ) and, in the case of multicomponent spectra, the amount by which each fraction contributes. These parameters are given in Table 3.2. In Fig. 2c, an example of a simulation is shown. Three fractions are visible, the fast, the slow and the immobile component, which have increasingly large linewidths. The individual components add up to give the experimental spectrum. Table 3.2 reveals that all but two spectra consist of a superposition of two components, the fast and slow components, except for the SL56 $\alpha$ S/S87A variant, which in addition has a third, the immobile component, and the SL90 $\alpha$ S/S87A and SL90 $\alpha$ S/S87D variants, which have only one component, the fast component. Each component reflects a part of the protein population: The fast fraction is due to protein in which the region around the site that is spin labelled is not attached to the membrane, whereas the slow and immobilized fractions are due to sections bound to the membrane. The amount by which each component contributes to the spectra (Table 3.2, columns four and six) reflects the fraction of protein contributing to each component. The correlation times can be determined to several tens of ps, in the case of the fast fraction, and several hundreds of ps for the slow fraction (see Table 3.2). The contribution of the fast component of  $\alpha$ S in the non-phosphorylated form is smaller than in the phosphorylated form for each probing position. The opposite is the case for the

### Chapter 3

contribution of the slow components. Both these trends reveal that phosphorylation reduces membrane binding.

To illustrate the effect of phosphorylation at position 87, Figure 3.3 shows a plot of the amount of the fast fraction for phosphorylation at position 87 as a function of the sequence number at which mobility is probed. For all monitoring positions, the amount of mobile fraction is larger in the phosphorylated variant. At monitoring positions 27 and 56, the amount of mobile fractions of non-phosphorylated  $\alpha S$  is below 10 %, which indicates strong binding, but at later positions (helix 2) the amount of fast fractions increases to 70 % indicating the loosening of the helix 2 of  $\alpha S$ , when it is non-phosphorylated, in agreement with previous findings for wt  $\alpha S$  (24). For the phosphorylated  $\alpha S$ , the amount of the mobile fraction is higher than in the non-phosphorylated form for all positions monitored, enhancing the tendency for local unbinding in helix 2 until, at position 90, the bound fraction is so low that it becomes undetectable.

## Chapter 3

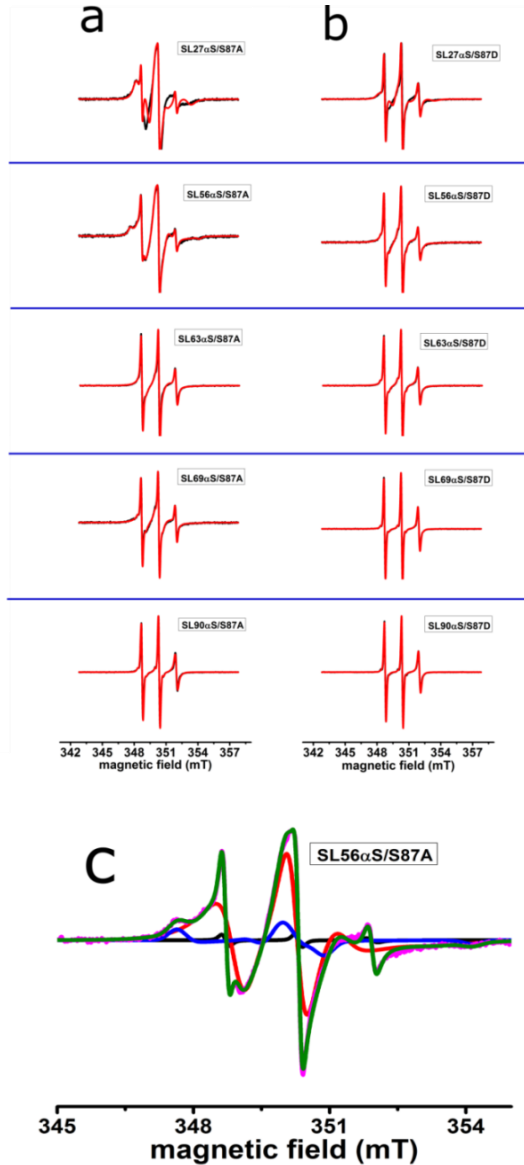


Figure 3.2. Effect of phosphorylation at position 87 on  $\alpha$ S-binding to LUVs: Room temperature, EPR spectra of spin-labelled  $\alpha$ S constructs (for nomenclature see Table 3.1) with LUVs of a 1:1 mixture of POPG and POPC; a. non-phosphorylated b. phosphorylated form. Black line: experiment, red line: simulation. c. Decomposition of EPR spectrum into components shown for SL56 $\alpha$ S/S87A. The fast (black), slow (red) and immobilized (blue) components are shown as well as the added simulation (green) and the experimental spectrum (pink).

### Chapter 3

Table 3.2. Effect of phosphorylation of  $\alpha$ S at position 87 (S87A/D): Parameters describing the mobility of the spin label in the EPR spectra;  $\tau_R$ , rotation correlation time of the spin label,  $A_{zz}$ , the hyperfine splitting along the Z-direction.

$\alpha$ S spin-label positions	components contributing to spectra	S87A (non-phosphorylated)			S87D (phosphorylated)		
		$\tau_R$ (ns)	contribution (%)	$A_{zz}$ (MHz)	$\tau_R$ (ns)	Contribution (%)	$A_{zz}$ (MHz)
SL 27	fast	$0.4 \pm 0.03$	$6 \pm 0.4$	110	$0.4 \pm 0.02$	$32 \pm 2$	110
	slow	$8.5 \pm 0.2$	$94 \pm 0.4$	85	$9.3 \pm 0.65$	$67 \pm 2$	83
	immobile	na	na	na	na	na	na
SL 56	fast	$0.4 \pm 0.02$	$6 \pm 0.2$	110	$0.4 \pm 0.03$	$34 \pm 3$	110
	slow	$3.2 \pm 0.07$	$78 \pm 1.2$	102	$3.1 \pm 0.4$	$63 \pm 3$	102
	immobile	>50	$16 \pm 1$	91	na	na	na
SL 63	fast	$0.35 \pm 0.04$	$29 \pm 2$	110	$0.4 \pm 0.03$	$51 \pm 5$	110
	slow	$2.6 \pm 0.3$	$70 \pm 2$	105	$2.5 \pm 0.6$	$44 \pm 5$	108
	immobile	na	na	na	na	na	na
SL 69	fast	$0.3 \pm 0.02$	$23 \pm 2$	110	$0.3 \pm 0.02$	$75 \pm 9$	110
	slow	$2.5 \pm 0.2$	$75 \pm 2$	110	$2.5 \pm 1.2$	$20 \pm 9$	110
	immobile	na	na	na	na	na	na

### Chapter 3

SL 76	fast	0.4 ± 0.04	42 ± 5	110	0.4 ± 0.02	79 ± 8	110
	slow	3.5 ± 0.8	57 ± 5	110	3.5 ± 3.2	16 ± 8	110
	immobile	na	na	na	na	na	na
SL 90	fast	0.4 ± 0.04	70 ± 10	110	0.3 ± 0.03	100* ± 8	110
	slow	2.5 ± 1.3	24 ± 10	110	na	na	na
	immobile	na	na	na	na	na	na

na: A component seen in other spectra, but not required to obtain a good simulation of the experimental spectrum in question, revealing that the rotational correlation time of the spin label does not contain contributions on the time scale of the component in question (for details see text and Fig. 2). For error determination see Materials and methods.\*including 4.5 % contribution of spin label with natural abundance of  $^{13}\text{C}$ .

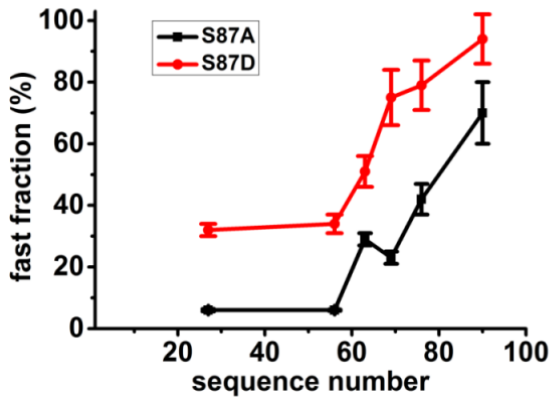


Figure 3.3. Local unbinding effect of phosphorylation at position 87: Amount of fast fraction in  $\alpha\text{S}$  87 A, D mutants in the presence of LUVs as a function of the sequence number. black: non-phosphorylated ( $\alpha\text{S}87\text{A}$ ), red: phosphorylated ( $\alpha\text{S}87\text{D}$ ) (see Table 3.2 for values), the lines connecting the points are guides to the eye.

To determine if the phosphorylation reduces the overall membrane affinity of  $\alpha\text{S}$ , i.e., if  $\alpha\text{S}$  detaches completely from the membrane, resulting in  $\alpha\text{S}$  protein that is

### Chapter 3

free in solution (physical unbinding) we separated the unbound fraction of  $\alpha$ S from the membrane-bound fraction, by filtrating the sample through a filter that retains the vesicles and  $\alpha$ S bound to them. The amount of physically unbound protein in the filtrate is then determined by EPR, as described in Drescher et al. (24) (for details see Materials and methods). The amount of unbound  $\alpha$ S is given in Table 3.3 and is below 16 % for all constructs. Thus the amount of physically unbound  $\alpha$ S is significantly lower than the amount of the fast fraction measured by EPR (see Table 3.2), showing that the local unbinding far out-weighs any physical unbinding. The percentages in Table 3.3 for spin label positions 27 and 56 are slightly lower than for the other positions. Given that the differences are just outside the error margins of the procedure, we cannot draw conclusions.

Table 3.3. Physical unbinding of  $\alpha$ S S87D from the membrane. Results of filtration experiments (for details, see Materials and methods and also Results).

mutants	$\alpha$ S unbound fraction (%)
SL27 $\alpha$ S/S87D	5.9 $\pm$ 2.0
SL56 $\alpha$ S/S87D	5.2 $\pm$ 1.0
SL69 $\alpha$ S/S87D	15.1 $\pm$ 3.0
SL90 $\alpha$ S/S87D	13.6 $\pm$ 3.0

For phosphorylation at position 129, Figure 3.4 shows the superposition of the spectra of non-phosphorylated and phosphorylated variants for three spin label positions (see Table 3.1). In contrast to phosphorylation at position 87, A and D variants at position 129 have similar spectra, obviating the need for detailed spectral analysis. Apparently, phosphorylation has a much smaller influence at position 129 than at position 87.

## Chapter 3

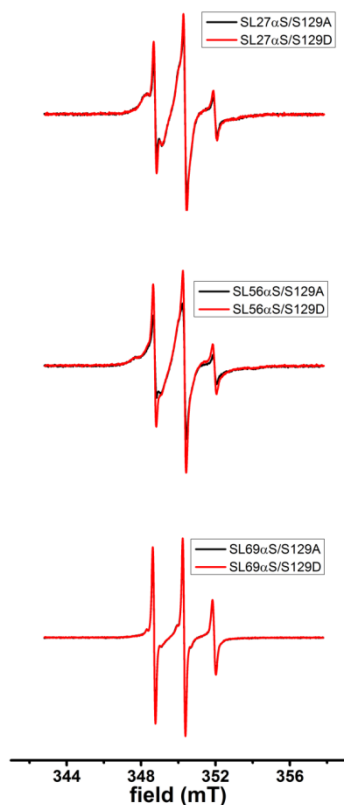


Figure 3.4. Effect of phosphorylation at position 129 on  $\alpha$ S-binding to LUVs: Room temperature, EPR spectra of spin-labelled  $\alpha$ S constructs (for nomenclature see Table 3.1) with LUVs of a 1:1 mixture of POG and POPC; Superposition of non-phosphorylated (black line) with phosphorylated EPR spectra (red line), normalized by their double integral value.

### 3.4 Discussion

We have investigated how membrane binding of  $\alpha$ S depends on the phosphorylation state of positions 87 and 129. Membrane binding is detected locally, via the mobility of spin labels attached to specific positions in the protein. An increased spin-label mobility shows that the protein detaches from the membrane around the position probed.

### Chapter 3

The membrane composition was chosen to be conducive to intermediate binding with a charge density of  $\rho = 0.5$ , to avoid: a) dominant electrostatic effects observed at higher charge densities, where they cause strong, undifferentiated binding and are non-physiological, b) overall unbinding observed at low charge densities (23,24,32–34), as described in the introduction. The membrane was offered in the form of LUVs of a diameter of 100 nm. We mimic phosphorylation by the phosphorylation-mutation approach, replacing S by D, an approach used before (13,17,29,30) (for details, see introduction). Although some studies showed that biochemically phosphorylated  $\alpha$ S can have different properties than phosphorylation mimics (29,31), the latter constructs provide a robust system to study phosphorylation effects in vitro, explaining their popularity.

Under the conditions of our study, phosphorylation at position 129 has no noticeable effect on membrane binding, whereas 87 has, similar to what was observed by other techniques in the past (13). In the following, we will first discuss the influence of phosphorylation at position 87 on  $\alpha$ S-membrane binding, and then compare the results obtained on both phosphorylation sites to previous findings in the literature.

When position 87 is phosphorylated, membrane binding is reduced relative to the non-phosphorylated case. An almost the same reduction of the binding is observed at positions 27 and 56 in the helix 1 region, see Figure 3.3. Similar to wild type  $\alpha$ S (24), also in the S87A variants, helix 2 has a lower membrane affinity than helix 1. Phosphorylation enhances this trend, up to the point that at probing position 90, the bound fraction becomes so low that it is undetectable. Complete, detachment of the phosphorylated protein from the membrane does not play a role: as seen in Table 3.3, the physically unbound fraction is below 16 % for all constructs. To place this into perspective, the amount of physically unbound  $\alpha$ S is

### Chapter 3

maximally one third of the amount of fast fraction determined from EPR, showing that the majority of the fraction, seen by EPR, derives from protein that is attached to the membrane, presumably at the residues preceding the probed sequence position, e.g. for sample SL27/ $\alpha$ S87P, residues 27 and below.

Fluctuations in the amount of fast fraction (Table 3.2, SL 63, non-phosphorylated (SL63/S87A) has a larger amount of fast fraction than SL 69) and a larger amount of physically unbound  $\alpha$ S for SL positions in helix 2 (Table 3.3), could indicate an influence of the spin label on  $\alpha$ S-membrane binding. If such an effect is present, it never exceeds a contribution of 10 %, and therefore is not relevant for the conclusions drawn.

Overall we find that phosphorylation at position 87 decreases the membrane affinity of  $\alpha$ S, more for helix 2. This effect is fully consistent with the change in the charge caused by the conversion of S $\rightarrow$ D or by phosphorylation: A negative charge in the helix 2 will weaken the electrostatic interaction with the negatively charged membrane surface as it counteracts the effect of several lysines (Lys;K) in the  $\alpha$ S sequence from residues 1-100. Reduced membrane binding of S87E and P-S87 has been reported before, e.g. (13) (41).

Reduced membrane binding affects the entire protein, but is most pronounced in the helix 2 region, and may selectively influence the behavior of helix 2. Some models propose that the physiological function of  $\alpha$ S involves vesicle fusion events in which helix 1 and helix 2 interact with different types of membranes (42). We therefore speculate that phosphorylation at position 87 could be used to tune how  $\alpha$ S operates in vesicle trafficking.

For the  $\alpha$ S129 A/D variants, the difference in mobility of the spin label for phosphorylated and non-phosphorylated forms is minute, showing that under the

### Chapter 3

membrane conditions employed here, phosphorylation at this site does not affect membrane binding. The C-terminus of  $\alpha$ S is already negatively charged and was not found to interact with the membrane in previous studies (20,21,24,38,43), which is fully consistent with the lack of changes in membrane-binding observed in the present study upon phosphorylation at position 129.

The results of the present study suggest that phosphorylation at position 87 tunes those functions of  $\alpha$ S that involve membrane binding and vesicle interaction, whereas phosphorylation at position 129 acts on other aspects of  $\alpha$ S in the organism. Previously (13) several possibilities of how phosphorylation at position 129 could affect  $\alpha$ S in vivo behavior are described and the study of Kosten et.al (44) shows that the phosphorylation at position 129 depends on the phosphorylation state of position 125, suggesting a complex interplay of posttranslational modifications in the C-terminus.

Most of the current research is focused on phosphorylation at position 129, and the phosphorylation degree at this position is related to disease effects, as reviewed in (45). In agreement with our results, several studies show that  $\alpha$ S phosphorylation at 129 has no or little effect on membrane binding, see for example (28). However, several studies find an influence of phosphorylation at 129 on the aggregation of  $\alpha$ S (28,29,46) and on membrane binding of  $\alpha$ S aggregates (46) suggesting that in vivo effects are linked to aggregation-sensitive processes.

In conclusion, the large spectrum of phosphorylation effects on  $\alpha$ S in vivo and in vitro (13–16,19,28–31,41,45–54) furnishes the need for isolating the different factors that can be modulated by  $\alpha$ S phosphorylation in vitro. The present study gives one such example, where we show that in vitro-phosphorylation mimics at

## Chapter 3

position 87 (S87D) reduce  $\alpha$ S-membrane binding in a local, sequence dependent manner, whereas the same modification at position 129 (S129D) has no influence on membrane binding. We expect that this approach provides a foothold to interpret the challenging in vivo physiological and pathological functions of  $\alpha$ S.

### 3.5 References

1. Parkinson J. An Essay on the Shaking Palsy (Whitingham and Rowland, London). 1817.
2. De Rijk MC, Breteler MM, Graveland GA, Ott A, Grobbee DE, van der Meché FG, Hofman A. Prevalence of Parkinson's disease in the elderly: the Rotterdam Study. *Neurology*. 1995;45:2143–2146.
3. Junn E, Ronchetti RD, Quezado MM, Kim S-Y, Mouradian MM. Tissue transglutaminase-induced aggregation of alpha-synuclein: Implications for Lewy body formation in Parkinson's disease and dementia with Lewy bodies. *Proc Natl Acad Sci U S A*. 2003;100:2047–2052.
4. Chung KK, Zhang Y, Lim KL, Tanaka Y, Huang H, Gao J, Ross CA, Dawson VL, Dawson TM. Parkin ubiquitinates the alpha-synuclein-interacting protein, synphilin-1: implications for Lewy-body formation in Parkinson disease. *Nat Med*. 2001;7:1144–1150.
5. Spillantini MG, Schmidt ML, Lee VM, Trojanowski JQ, Jakes R, Goedert M. Alpha-synuclein in Lewy bodies. *Nature*. 1997;388:839–840.
6. Spillantini MG, Crowther RA, Jakes R, Hasegawa M, Goedert M.  $\alpha$ -Synuclein in filamentous inclusions of Lewy bodies from Parkinson's disease and dementia with Lewy bodies. *Proc Natl Acad Sci U S A*. 1998;95:6469–6473.
7. Goedert M. Alpha-synuclein and neurodegenerative diseases. *Nat Rev Neurosci*. 2001;2: 492–501.
8. Fujiwara H, Hasegawa M, Dohmae N, Kawashima A, Masliah E, Goldberg MS, Shen J, Takio K, Iwatsubo T.  $\alpha$ -Synuclein is phosphorylated in synucleinopathy lesions. *Nat Cell Biol*. 2002;4:160–164.
9. Anderson JP, Walker DE, Goldstein JM, De Laat R, Banducci K, Caccavello RJ, Barbour R, Huang J, Kling K, Lee M, Diep L, Keim PS, Shen X, Chataway T, Schlossmacher MG, Seubert P, Schenk D, Sinha S, Gai WP, Chilcote TJ.

### Chapter 3

- Phosphorylation of Ser-129 is the dominant pathological modification of  $\alpha$ -Synuclein in familial and sporadic Lewy body disease. *J Biol Chem.* 2006;281:29739–29752.
10. Okochi M, Walter J, Koyama a, Nakajo S, Baba M, Iwatsubo T, Meijer L, Kahle PJ, Haass C. Constitutive phosphorylation of the Parkinson's disease associated  $\alpha$ -Synuclein. *J Biol Chem.* 2000;275:390–397.
  11. Shimura H, Schlossmacher M, Hattori, N.Frosch M, Trockenbacher A, Schneider R, Mizuno Y, Kosik KS, Selkoe DJ. Ubiquitination of a new form of  $\alpha$ -Synuclein by parkin from human brain: implications for Parkinson's disease. *Science.* 2001;293:263–269.
  12. Hodara R, Norris EH, Giasson BI, Mishizen-Eberz AJ, Lynch DR, Lee VM, Ischiropoulos H. Functional consequences of  $\alpha$ -Synuclein tyrosine nitration: diminished binding to lipid vesicles and increased fibril formation. *J Biol Chem.* 2004;279:47746–47753.
  13. Paleologou KE, Oueslati A, Shakked G, Rospigliosi CC, Kim H-Y, Lamberto GR, Fernandez CO, Schmid A, Chegini F, Gai WP, Chiappe D, Moniatte M, Schneider BL, Aebischer P, Eliezer D, Zweckstetter M, Masliah E, Lashuel HA. Phosphorylation at S87 Is enhanced in synucleinopathies, inhibits  $\alpha$ -Synuclein oligomerization, and influences Synuclein-membrane interactions. *J Neurosci.* 2010;30:3184–3198.
  14. Gorbatyuk OS, Li S, Sullivan LF, Chen W, Kondrikova G, Manfredsson FP, Mandel RJ, Muzyczka N. The phosphorylation state of Ser-129 in human  $\alpha$ -Synuclein determines neurodegeneration in a rat model of Parkinson disease. *Proc Natl Acad Sci U S A.* 2008;105:763–768.
  15. McFarland NR, Fan Z, Xu K, Schwarzschild MA, Feany MB, Hyman BT, McLean PJ.  $\alpha$ -Synuclein S129 phosphorylation mutants do not alter nigrostriatal toxicity in a rat model of Parkinson disease. *J Neuropathol Exp Neurol.* 2009;68:515–524.
  16. Smith WW.  $\alpha$ -Synuclein phosphorylation enhances eosinophilic cytoplasmic inclusion formation in SH-SY5Y cells. *J Neurosci.* 2005;25:5544–5552.
  17. Chen L, Feany MB.  $\alpha$ -Synuclein phosphorylation controls neurotoxicity and inclusion formation in a *Drosophila* model of Parkinson disease. *Nat Neurosci.* 2005;8:657–663.
  18. Tenreiro S, Eckermann K, Outeiro TF. Protein phosphorylation in neurodegeneration: Friend or foe? *Front Mol Neurosci.* 2014;7:1-30.
  19. Sato H, Kato T, Arawaka S. The role of Ser129 phosphorylation of  $\alpha$ -Synuclein in neurodegeneration of Parkinson's disease: A review of in vivo models. *Rev Neurosci.* 2013;24:115–123.
  20. W S Davidson, A Jonas, D F Clayton JMG. Stabilization of  $\alpha$ -Synuclein secondary structure upon binding to synthetic membranes. *J Biol Chem.* 1998;273:9443–9449.

### Chapter 3

21. Eliezer D, Kutluay E, Bussell R, Browne G. Conformational properties of  $\alpha$ -Synuclein in its free and lipid-associated states. *J Mol Biol.* 2001;307:1061–1073.
22. Jao CC, Hegde BG, Chen J, Haworth IS, Langen R. Structure of membrane-bound  $\alpha$ -Synuclein from site-directed spin labeling and computational refinement. *Proc Natl Acad Sci U S A.* 2008;105:19666–19671.
23. Middleton ER, Rhoades E. Effects of curvature and composition on  $\alpha$ -Synuclein binding to lipid vesicles. *Biophys J.* 2010;99:2279–2288.
24. Drescher M, Godschalk F, Veldhuis G, van Rooijen BD, Subramaniam V, Huber M. Spin-label EPR on  $\alpha$ -Synuclein reveals differences in the membrane binding affinity of the two antiparallel helices. *ChemBioChem.* 2008;9:2411–2416.
25. Burnett G, Kennedy EP. The enzymatic phosphorylation of proteins. *J Biol Chem.* 1954; 211:969–980.
26. Kresge N, Simoni RD, Hill RL. The process of reversible phosphorylation: The work of Edmond H. Fischer. *J Biol Chem.* 2011;286:e1–e2.
27. Hejjaoui M, Butterfield S, Fauvet B, Vercruyse F, Cui J, Dikiy I, Prudent M, Olschewski D, Zhang Y, Eliezer D, Lashuel HA. Elucidating the role of C-terminal post-translational modifications using protein semisynthesis strategies:  $\alpha$ -Synuclein phosphorylation at tyrosine 125. *J Am Chem Soc.* 2012;134:5196–5210.
28. Nübling GS, Levin J, Bader B, Lorenzl S, Hillmer A, Högen T, Kamp F, Giese A. Modelling Ser129 phosphorylation inhibits membrane binding of pore-forming  $\alpha$ -Synuclein oligomers. *PLoS One.* 2014;9:1-7.
29. Paleologou KE, Schmid AW, Rospigliosi CC, Kim H-Y, Lamberto GR, Fredenborg RA, Lansbury Jr PT, Fernandez CO, Eliezer D, Zweckstetter M, Lashuel HA. Phosphorylation at Ser-129 but not the phosphomimics S129E/D inhibits the fibrillation of  $\alpha$ -Synuclein. *J Biol Chem.* 2008;283:16895–16905.
30. Chen L, Periquet M, Wang X, Negro A, Mclean PJ, Hyman BT, Feany MB. Tyrosine and serine phosphorylation of  $\alpha$ -Synuclein have opposing effects on neurotoxicity and soluble oligomer formation. *J Clin Invest.* 2009;119:3257–3265.
31. Schreurs S, Gerard M, Derua R, Waelkens E, Taymans J-M, Baekelandt V, Engelborghs Y. In Vitro phosphorylation does not influence the aggregation kinetics of WT  $\alpha$ -Synuclein in contrast to its phosphorylation mutants. *Int J Mol Sci.* 2014;15:1040–1067.
32. Robotta M, Hintze C, Schildknecht S, Zijlstra N, Jüngst C, Karreman C, Huber M, Leist M, Subramaniam V, Drescher M. Locally resolved membrane binding affinity of the N-terminus of  $\alpha$ -Synuclein. *Biochemistry.* 2012;51:3960–3962.
33. Robotta M, Gerding HR, Vogel A, Hauser K, Schildknecht S, Karreman C, Leist M, Subramaniam V, Drescher M. Alpha-Synuclein binds to the inner membrane of mitochondria in an  $\alpha$ -helical conformation. *Chembiochem.* 2014;1–4.

### Chapter 3

34. Kumar P, Segers-Nolten IMJ, Schilderink N, Subramaniam V, Huber M. Parkinson's protein  $\alpha$ -Synuclein binds efficiently and with a novel conformation to two natural membrane mimics. *PLoS One*. 2015;10:1-11.
35. Hubbell WL, Gross A, Langen R, Lietzow MA. Recent advances in site-directed spin labelling of proteins. *Curr Opin Struct Biol*. 1998;8:649–656.
36. Van Raaij ME, Segers-Nolten IMJ, Subramaniam V. Quantitative morphological analysis reveals ultrastructural diversity of amyloid fibrils from alpha-synuclein mutants. *Biophys J*. 2006;91:L96–L98.
37. Veldhuis G, Segers-Nolten I, Ferlemann E, Subramaniam V. Single-molecule FRET reveals structural heterogeneity of SDS-bound  $\alpha$ -synuclein. *ChemBioChem*. 2009;10:436–439.
38. Jao CC, Der-Sarkissian A, Chen J, Langen R. Structure of membrane-bound  $\alpha$ -Synuclein studied by site-directed spin labeling. *Proc Natl Acad Sci U S A*. 2004;101:8331–8336.
39. Stoll S, Schweiger A. EasySpin, a comprehensive software package for spectral simulation and analysis in EPR. *J Magn Reson*. 2006;178:42–55.
40. Steigmiller S, Börsch M, Gräber P, Huber M. Distances between the b-subunits in the tether domain of FOF1-ATP synthase from *E. coli*. *Biochim Biophys Acta-Bioenerg*. 2005;1708:143–153.
41. Oueslati A, Paleologou KE, Schneider BL, Aebischer P, Lashuel HA. Mimicking phosphorylation at serine 87 inhibits the aggregation of human  $\alpha$ -Synuclein and protects against its toxicity in a rat model of Parkinson's disease. *J Neurosci*. 2012;32:1536–1544.
42. Dikiy I, Eliezer D. Folding and misfolding of  $\alpha$ -Synuclein on membranes. *Biochim Biophys Acta - Biomembr*. 2012;1818:1013–1018.
43. Ulmer TS, Bax A. Structure and dynamics of micelle-bound human  $\alpha$ -Synuclein. *J Biol Chem*. 2005;280:9595–9603.
44. Kosten J, Binolfi A, Stuiver M, Verzini S, Theillet F-X, Bekei B, van Rossum M, Selenko P. Efficient modification of  $\alpha$ -Synuclein serine 129 by protein kinase CK1 requires phosphorylation of tyrosine 125 as a priming event. *ACS Chem Neurosci*. 2014;5:1203–1208.
45. Oueslati A. Implication of  $\alpha$ -Synuclein phosphorylation at S129 in synucleinopathies: What have we learned in the last decade? *J Parkinsons Dis*. 2016;6:39–51.
46. Samuel F, Flavin WP, Iqbal S, Pacelli C, Sri Renganathan SD, Trudeau LE, Campbell EM, Fraser PE, Tandon A. Effects of serine 129 phosphorylation on  $\alpha$ -Synuclein aggregation, membrane association, and internalization. *J Biol Chem*. 2016;291:4374–4385.

### Chapter 3

47. Azeredo da Silveira S, Schneider BL, Cifuentes-Diaz C, Sage D, Abbas-Terki T, Iwatsubo T, Unser M, Aebischer P. Phosphorylation does not prompt, nor prevent, the formation of  $\alpha$ -Synuclein toxic species in a rat model of Parkinson's disease. *Hum Mol Genet.* 2009;18:872–887.
48. Braithwaite SP, Stock JB, Mouradian MM.  $\alpha$ -Synuclein phosphorylation as a therapeutic target in Parkinson's disease. *Rev Neurosci.* 2012;23:191–198.
49. Fiske M, Valtierra S, Solvang K, Zorniak M, White M, Herrera S, Konnikova A, Brezinsky R, Deb Burman S, Contribution of alanine-76 and serine phosphorylation in  $\alpha$ -Synuclein membrane association and aggregation in yeasts. *Parkinsons Dis.* 2011;2011:1-12.
50. Ha Y, Yang A, Lee S, Kim K, Liew H, Suh YH, Park HS, Churchill DG. Facile “stop codon” method reveals elevated neuronal toxicity by discrete S87p- $\alpha$ -Synuclein oligomers. *Biochem Biophys Res Commun.* 2014;443:1085–1091.
51. Kuwahara T, Tonegawa R, Ito G, Mitani S, Iwatsubo T. Phosphorylation of  $\alpha$ -Synuclein protein at Ser-129 reduces neuronal dysfunction by lowering its membrane binding property in *Caenorhabditis elegans*. *J Biol Chem.* 2012;287:7098–7109.
52. Visanji NP, Wislet-Gendebien S, Oschipok LW, Zhang G, Aubert I, Fraser PE, Tondon A. Effect of Ser-129 phosphorylation on interaction of  $\alpha$ -Synuclein with synaptic and cellular membranes. *J Biol Chem.* 2011;286:35863–35873.
53. Tenreiro S, Reimão-Pinto MM, Antas P, Rino J, Wawrzycka D, Macedo D, Rosado-Ramos R, Amen T, Waiss M, Magalhaes F, Gomes A, Santos CN, Kaganovich D, Outeiro TF. Phosphorylation modulates clearance of  $\alpha$ -Synuclein inclusions in a yeast model of Parkinson's Disease. *PLoS Genet.* 2014;10:1-23.
54. Xu Y, Deng Y, Qing H. The phosphorylation of  $\alpha$ -Synuclein: Development and implication for the mechanism and therapy of the Parkinson's disease. *J Neurochem.* 2015;135:4–18.

## Appendix A to Chapter 3

In chapter 3, the effect of phosphorylation of  $\alpha$ -Synuclein ( $\alpha$ S) on binding to large unilamellar vesicles (LUVs) was studied, here we investigate the interaction of phosphorylated and non-phosphorylated  $\alpha$ S with small unilamellar vesicles (SUVs) with the same lipid compositions as used for LUVs, i.e., POPG : POPC = 1 : 1 (charge density  $\rho = 0.5$ ). We describe the binding of S87 variants of  $\alpha$ S at three probing positions (27, 56 and 69) by spin-labeled electron paramagnetic resonance (EPR) spectroscopy.

SUVs were prepared as described in chapter 2. The size of the vesicles was determined by dynamic light scattering (DLS). The DLS-experiments were performed on a Zetasizer Nano-ZS (Malvern). We obtained vesicles with a homogeneous size distribution with a diameter of approximately  $d = 50$  nm.

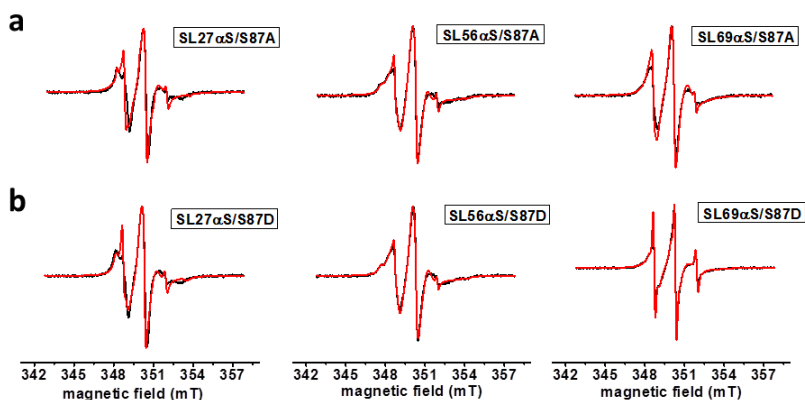


Figure A1. Effect of phosphorylation at position 87 on  $\alpha$ S-binding to SUVs: Room temperature, EPR spectra of spin-labeled  $\alpha$ S constructs (SL27, 56, and 69) with SUVs of a 1:1 mixture of POPG and POPC; a. non-phosphorylated b. phosphorylated form. Black line: experiment, red line: simulation.

### Chapter 3

Figure A1 shows the spectra of spin-labeled constructs of  $\alpha$ S probing the effect of phosphorylation at position 87 in the presence of SUVs. In this set, helix 1 is probed in the middle, at residue 27, helix 2 is probed at positions 56 and 69.

Table A1. Effect of phosphorylation of  $\alpha$ S at position 87 (S87A/D): Parameters describing the mobility of the spin label in the EPR spectra;  $\tau_r$  rotation correlation time of the spin label

$\alpha$ S spin label positions	components contributing in simulations	S87A (non-phosphorylated)		S87D (phosphorylated)	
		$\tau_r$ (ns)	contribution (%)	$\tau_r$ (ns)	contribution (%)
SL 27	fast	0.4	5	0.4	5
	slow	2.5	90	2.8	93
	immobile	>50	5	>50	2
SL 56	fast	0.48	2	0.44	1
	slow	3.2	91	2.9	90
	immobile	>50	6	>50	8
SL 69	fast	0.3	2	0.3	14
	slow	2.2	98	2.5	86
	immobile	na	na	na	na

for error see table 2

Figure A1a shows the spectra of  $\alpha$ S in the non-phosphorylated and Figure A1b in the phosphorylated form. In contrast to what we observe with LUVs, the spectra of  $\alpha$ S27 and  $\alpha$ S56 in the non-phosphorylated case (Figure A1a) are similar to those of the phosphorylated case (Figure A1b). The spectrum of  $\alpha$ S69 in the phosphorylated case shows that the lines are narrower compared to its

### Chapter 3

non-phosphorylated counterpart. This is also evident from the simulation parameters shown in Table A1. Overall,  $\alpha S$  shows stronger binding to SUVs than to LUVs (chapter 3) for the non-phosphorylated and phosphorylated variants, which is masking the effect of phosphorylation seen on LUVs.



**4 Characterization of Fibrils Obtained by Seeded  
Fibrillization of a Series of Spin-Labeled  $\alpha$ -  
Synuclein Variants by Transmission Electron  
Microscopy**

## Chapter 4

### 4.1 Introduction

The protein  $\alpha$ -Synuclein ( $\alpha$ S) is 140 amino-acids long and is present mainly in the human brain. The protein monomer is intrinsically disordered (1), which under certain conditions forms amyloid fibrils (2–9). Polymorphism of fibrils was described previously, for example, for Amyloid  $\beta$  (10), Immunoglobulin (Ig) light chains (11), ovalbumin (12), lysozyme (13), and also  $\alpha$ S (14–17).

In an accompanying pulsed-EPR study (chapter 5), we sought to determine the inner intrinsic fold of  $\alpha$ S in fibrils using  $\alpha$ S with spin labels at different positions. For that, independent information about the fibril morphology was desired. The main question was whether the fibrils of all spin-label constructs have the same morphology. To do so, we prepared the fibrils of nine doubly spin-labeled variants ( $\alpha$ S42/69,  $\alpha$ S42/75,  $\alpha$ S42/85,  $\alpha$ S56/69,  $\alpha$ S56/75,  $\alpha$ S56/90,  $\alpha$ S69/85,  $\alpha$ S69/90, and  $\alpha$ S75/85) and characterized the morphology by transmission electron microscopy (TEM). All the proteins were fibrillized as described in the Materials and methods section. We used the same fibrils for the successive EPR study in chapter 5.

In this study, we found that the morphology of the fibrils of all protein constructs grown under the conditions described in the present study is similar.

### 4.2 Materials and methods

#### 4.2.1 Preparation of fibrillar $\alpha$ S

The expression, purification and MTSL-labelling of the protein  $\alpha$ S has been described in chapter 5 (18–20).

## Chapter 4

### 4.2.1.1 Preparation of $\alpha$ S-fibril seeds

For seeds, we first prepared wild type (wt)  $\alpha$ S fibrils following the protocol from Sidhu *et al.* (17). Briefly, the wt- $\alpha$ S protein solution (concentration = 100  $\mu$ M, in 10 mM Tris- Cl buffer pH 7.4 containing 10 mM NaCl and 0.1 mM EDTA) was aliquoted into 15 Eppendorf tubes (Eppendorf LoProtein Bind 2 ml), 500  $\mu$ l each. All tubes were incubated at a temperature of 37  $^{\circ}$ C shaking continuously at 500 rpm in a Thermo mixer (Eppendorf). The time evolution of  $\alpha$ S fibrillization was monitored by the standard Thioflavin T (ThioT) fluorescence assay. For each tube, fibrillization was stopped when ThioT fluorescence intensity had reached a plateau. The fibrillization was completed in 6-7 days. The content of each Eppendorf tube was divided into two samples of 250  $\mu$ l each, which were frozen quickly in liquid nitrogen and stored at - 20  $^{\circ}$ C. To start the seeded fibrillization experiment, one aliquot was thawed and sonicated in a bath sonicator (Branson 2510) for one minute to break the fibrils into seeds, which were then added to the samples to be fibrillized.

### 4.2.1.2 Seeded fibrillization of spin-labeled $\alpha$ S

We prepared the fibrils by mixing the monomeric  $\alpha$ S (spin-labeled and wild type  $\alpha$ S) with the wt- $\alpha$ S seeds. The total monomer concentration used for making fibrils was 100  $\mu$ M. To this mixture 2 % monomer equivalent seeds were added. Diamagnetic dilution was employed to diminish the effect of intermolecular interaction. We used 1:20 (SL $\alpha$ S:wt) diamagnetic dilution for all doubly labeled  $\alpha$ S. A typical sample for doubly labeled  $\alpha$ S consisted of 5  $\mu$ M spin-labeled  $\alpha$ S, 95  $\mu$ M wt- $\alpha$ S and 2  $\mu$ M  $\alpha$ S-monomer equivalent seeds. The total volume for each sample was 3.0 ml, which was aliquoted into five Eppendorf tubes and put on the thermomixer. The seeded fibrillization was performed under the same conditions

## Chapter 4

as used for wt- $\alpha$ S fibrils (17). The time evolution of seeded fibrillization was monitored by the standard Thioflavin T (ThioT) fluorescence assay. Most of the mutants completed the aggregation, i.e., fluorescence intensity reached the plateau, in 24 hours except for  $\alpha$ S69/90, which took 9 days to complete the aggregation. These samples, after harvesting, were used for the pulsed EPR experiments, described in chapter 5. A small amount of fibril solution from each sample was used to prepare TEM-grids to visualize the morphology.

### 4.2.1.3 Preparation of unseeded fibrils of $\alpha$ S69/90

The unseeded fibril of  $\alpha$ S69/90 (referred to as  **$\alpha$ S69/90** in the text) was prepared following the method described by Hashemi Shabestari *et al.* (21), described briefly. The total monomer concentration used for making fibrils was kept 100  $\mu$ M. We used a diamagnetic dilution of 1:20 (SL  $\alpha$ S:wt) similar to the seeded fibrillization case. The fibrillization mixture was prepared by mixing a 5  $\mu$ M spin-labeled  $\alpha$ S69/90 with 95  $\mu$ M wt- $\alpha$ S protein in 10 mM Tris-Cl buffer, pH 7.4, containing 50 mM NaCl. The total volume of the mixture was 2.8 ml, which was aliquoted into four Eppendorf tubes (Eppendorf LoProtein Bind 2ml), 700  $\mu$ l each. All tubes were incubated at a temperature of 37 °C with constant shaking at 1000 rpm in a Thermo mixer (Eppendorf). The time evolution of fibrillization was monitored by the ThioT assay. For each tube, fibrillization was stopped when the ThioT-fluorescence intensity reached a plateau. The fibrillization was completed in 6-7 days. A small amount of fibril solution was used for TEM and the remaining fibril solution was harvested as described above and double electron-electron resonance (DEER) experiment (see appendix B) was performed.

## Chapter 4

### 4.2.2 Transmission electron microscopy

Negative staining of  $\alpha$ S fibril samples was done by placing a fresh carbon-coated grid (200 meshes) on top of a drop (10  $\mu$ l) of the  $\alpha$ S-fibril solution for 2 minutes. The grid was then washed 3 times on a drop of distilled water. Subsequently, the grids were placed directly on top of a small drop of 3.5 % uranyl acetate for 1.5 minutes and the excess uranyl acetate was blotted away by touching the grids to a filter paper at an angle of 45°. Afterwards the grids were placed in a Petri dish with filter paper to let them dry. The grids were examined with a FEI Technai-12 G2 Spirit Biotwin transmission electron microscope (FEI, Eindhoven, Netherlands) and micrographs were taken with a Veleta side-mounted TEM camera using Radius acquisition software (both Olympus Soft Imaging Solutions, Münster, Germany). Images were measured using the image processing feature within the Radius software package.

### 4.3 Results

Figures 4.1 and 4.2 show the TEM images of  $\alpha$ S fibrils prepared under seeded conditions. These Figures show that all fibrils used in this study have a similar appearance, which we describe in the following. Single fibrils have a width of  $5.6 \pm 1$  nm (Figure 4.1a, bottom, black arrows) and are often found to twin with another fibril that runs parallel to generate a fibril with a width of 9-10 nm marked by black arrows (see Figure 4.1a & Figure 4.2g, middle, and Table 4.1). Many of these twinned fibrils are twisted. We further characterize twinned fibrils with the periodicity of the twist, measured between the points marked by white arrows in Figure 4.1c and 4.2f, middle. With the exception of  $\alpha$ S56/75,  $\alpha$ S75/85 and  $\alpha$ S69/90, all fibrils show families of periodicities around 170 nm, 240 nm, and 290 nm. Fibrils of  $\alpha$ S56/75 show periodicity around 53 nm, 103 nm, and 152 nm,

## Chapter 4

while fibrils of  $\alpha$ S75/85 and  $\alpha$ S69/90 show just one family of periodicity around 177 nm and 190 nm respectively.

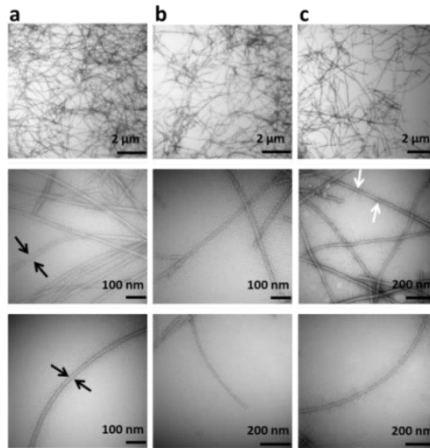


Figure 4.1. Morphological characterization of seeded fibrils of  $\alpha$ S by TEM. a.  $\alpha$ S42/69, b.  $\alpha$ S42/75, c.  $\alpha$ S42/85. Black arrows depict the width of a single fibril as shown for  $\alpha$ S42/69 fibril. White arrows depict the points of cross-over of a twist in the fibril and the periodicity was measured between the points as shown for  $\alpha$ S42/85 fibril.

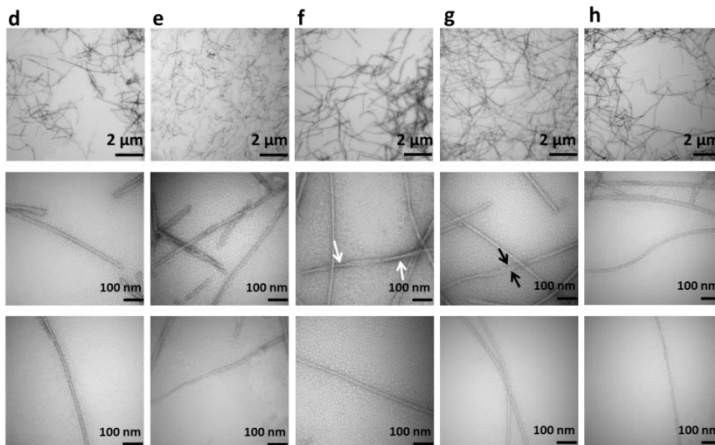


Figure 4.2. Morphological characterization of seeded fibrils of  $\alpha$ S by TEM. d.  $\alpha$ S56/69, e.  $\alpha$ S56/75, f.  $\alpha$ S56/90, g.  $\alpha$ S69/85, and h.  $\alpha$ S75/85. White arrows depict the points of cross-over of a twist in the fibril as shown for  $\alpha$ S56/90. Black arrows depict the width of a twin fibril running together.

## Chapter 4

Table 4.1. Morphology parameters of Seeded fibrils of  $\alpha$ S based on TEM

<b><math>\alpha</math>S fibril sample</b>	<b>Single fibril width (nm) <math>\pm</math> stdv (nm) [no of fibrils checked]</b>	<b>Twinned fibril width (nm) <math>\pm</math> stdv (nm) [no of fibrils checked]</b>	<b>Periodicity (nm) <math>\pm</math> stdv (nm) [no of fibrils checked]</b>
<b><math>\alpha</math>S42/69</b>	5.5 $\pm$ 0.9 [17]	9.45 $\pm$ 1.0 [7]	182.5 $\pm$ 9.5 [10], 237.8 $\pm$ 7.9 [2], 285.7 $\pm$ 14.7 [2]
<b><math>\alpha</math>S42/75</b>	5.4 $\pm$ 1.0 [16]	10.6 $\pm$ 1.2 [5]	165.8 $\pm$ 8.6 [11], 235 [1]
<b><math>\alpha</math>S42/85</b>	6.0 $\pm$ 0.6 [36]	9.5 $\pm$ 1.6 [13]	164.3 $\pm$ 9.9 [11], 227.8 $\pm$ 15 [13], 293.4 $\pm$ 9.7 [4]
<b><math>\alpha</math>S56/69</b>	6.1 $\pm$ 1.1 [7]	9.0 $\pm$ 1.3 [9]	171.8 $\pm$ 7.7 [16], 242.2 $\pm$ 6.0 [4]
<b><math>\alpha</math>S56/75</b>	5.7 $\pm$ 1.0 [7]	10.6 $\pm$ 2.2 [4]	53 $\pm$ 6.0 [2], 103 $\pm$ 12.4 [2], 152 [1]
<b><math>\alpha</math>S56/90</b>	5.2 $\pm$ 1.1 [9]	9.2 $\pm$ 1.0 [6]	165 $\pm$ 6.0 [4], 206 $\pm$ 13.5 [12], 266.8 $\pm$ 11.4 [6]
<b><math>\alpha</math>S69/85</b>	6.3 $\pm$ 1.0 [9]	11.1 $\pm$ 2.3 [8]	181.2 $\pm$ 6.0 [2], 308.3 $\pm$ 6.0 [3]
<b><math>\alpha</math>S69/90</b>	5.7 $\pm$ 1.0 [22]	8.7 $\pm$ 0.9 [4]	190.4 $\pm$ 6.0 [2]
<b><math>\alpha</math>S75/85</b>	5.0 $\pm$ 1.4 [5]	9.2 $\pm$ 0.1 [3]	177.4 $\pm$ 9.9 [5]

To illustrate the comparison of fibril morphology, we show the width and the periodicity of fibrils (given in Table 4.1) as a scatter plot in Figures 4a and b. Figure 4.3a shows the plot of the width of fibrils as a function of the type of fibrils (single and twinned fibril), and Figure 4.3b shows the plot of the periodicities of the fibrils. Figure 4.3a illustrates that the width of the fibrils are the same within the error margins of the measurement. Figure 4.3b shows that there are three distinct clusters of periodicities for most of the fibrils. With the exception of  $\alpha$ S56/75, the

## Chapter 4

periodicity of the fibrils within the clusters agrees within experimental error. The fibrils of  $\alpha$ S75/85 and  $\alpha$ S69/90 show just one class of periodicity of 177 nm and 190 nm respectively, take into account the smallest number of observations compared to the other fibrils. For all fibril samples, the difference between the clusters of periodicities is around 50 nm.

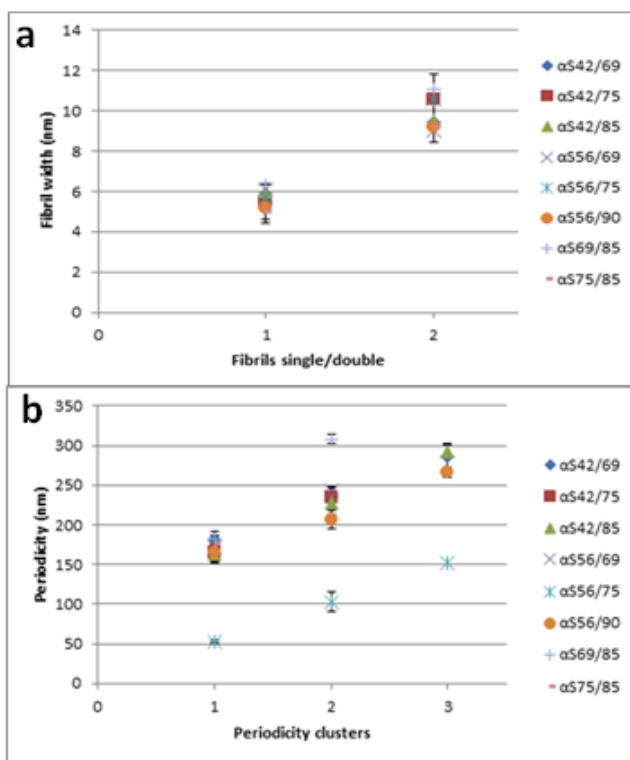


Figure 4.3. Scatter plots representing quantitative morphological features (listed in Table 4.1) of  $\alpha$ S fibrils prepared under seeded condition (for details see Materials and methods): a. comparison of width of fibrils (given in Table 4.1); b. comparison of periodicities of fibrils (given in Table 4.1). Cluster 1: shortest periodicities; cluster 2: medium periodicities; cluster 3: longest periodicities.

## Chapter 4

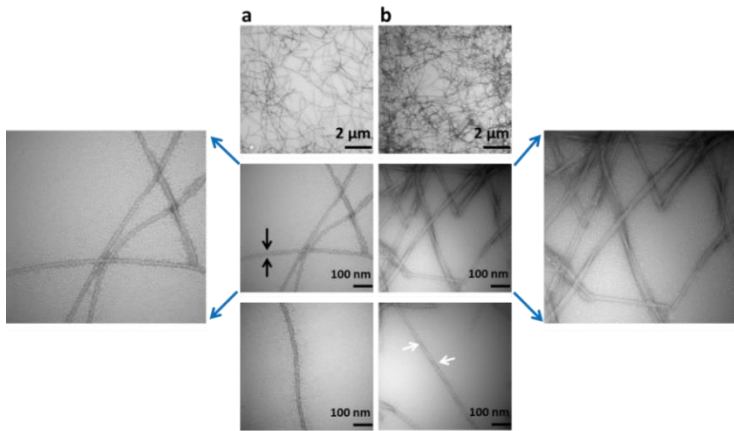


Figure 4.4. Morphological characterization of fibrils of  $\alpha$ S by TEM. Comparison of morphology of the fibril prepared from the same  $\alpha$ S69/90 protein a. under seeded conditions (for details, see Materials and methods); b. under the conditions described in Hashemi Shabestari *et al.* (21); Far left: middle panel of (a) scaled up (1.5x); Far right: middle panel of (b) scaled up (1.5x) for better view. Black arrows depict the width of the fibril, white arrows depict the points of cross-over.

Table 4.2. Comparison of fibril morphology of  $\alpha$ S grown under seeded and unseeded conditions (21) based on TEM.

$\alpha$ S fibril sample	Single fibril width (nm) $\pm$ stdv (nm) [no of fibrils checked]	Twinned fibril width (nm) $\pm$ stdv (nm) [no of fibrils checked]	Periodicity (nm) $\pm$ stdv (nm) [no of fibrils checked]
$\alpha$ S69/90	$5.7 \pm 1.0$ [22]	$8.7 \pm 0.9$ [4]	$190.4 \pm 6.0$ [2]
<b><math>\alpha</math>S69/90</b>	$5.6 \pm 1.0$ [9]	$10.6 \pm 1.2$ [5]	$116.6 \pm 6.0$ [4], $233 \pm 8$ [6], $278.7 \pm 6.0$ [3], $321.5 \pm 9$ [3], $352$ [1]

Figure 4.4 shows the TEM images of fibrils prepared from the same  $\alpha$ S69/90 protein, but under two different fibrillization conditions. Figure 4.4a shows the fibril morphology for the seeded-fibrillization conditions used in the present study (see Materials and methods), and Figure 4.4b for the fibrillization conditions

## Chapter 4

described in Hashemi Shabestari *et al.* (21,22). For clarity, we use the abbreviation  **$\alpha$ S69/90** for the latter fibrils (21). Comparing the images in Figure 4.4a and b, in Figure 4.4b fibrils appear somewhat wider (far right, enlarged view) than fibrils in Figure 4.4a (far left, enlarged view). Single fibrils, in Figure 4.4a, have a width of  $5.7 \pm 1$  nm (shown with black arrows and Table 4.2), similar to the width of the fibrils shown in Figure 4.4b (Table 4.2). Fibrils in seeded conditions show twinned fibrils of width  $8.7 \pm 0.9$  and a periodicity of  $190 \pm 6$  nm (as shown in Figure 4.4a and Table 4.2). On the other hand, twinned fibrils of  **$\alpha$ S69/90** show twists with several different periodicity lengths (shown in Table 4.2 and Figure 4.4b; twists are indicated by white arrows). The separation between the periodicity lengths varies from 45 nm to 100 nm. The differences in morphology of fibrils, grown under seeded conditions and conditions described by Hashemi Shabestari *et al.* (21), are larger than those seen between fibrils grown from different spin-label constructs under the same conditions i.e., under seeded conditions.

### 4.4 Discussion

In this study, we have used a seeded fibrillization procedure employing the conditions described in A. Sidhu *et al.* (17) (see also Materials and methods) to prepare fibrils of homogeneous morphology. Fibrils of nine different  $\alpha$ S spin-labelled variants were prepared and their morphology checked by negative stain Transmission Electron Microscopy (TEM). The overall appearance of the fibrils of all constructs is similar. The width of single fibrils and twinned fibrils in all constructs agree within the error margin of the measurement. From this, we conclude that the fibrils of all  $\alpha$ S constructs have the same morphology. The origin of the differences in the periods of the twisted fibrils are not clear, but since different periods occur within one sample, it is likely that different periods do not affect the internal structure of the fibril, i.e., the fold of the protein within the

## Chapter 4

fibril. We also observe that fibrils grown under different conditions, i.e,  $\alpha$ S69/90 and  $\alpha$ S69/90, have a difference in their TEM appearance (shown in Figure 4.4).

Fibrils isolated from the brain of patients of Parkinson's disease show a width of  $\sim 5$  nm for a single untwisted  $\alpha$ S-fibril (23), which is consistent with our finding in the present study. Vilar *et al.* (14) have reported  $\alpha$ S-fibrils that were described as straight fibrils with a width of  $5.5 \pm 0.5$  nm. They also reported that two such straight fibrils often run together with a width of  $13 \pm 1.0$  nm. The single-fibril width in this case is in agreement with the fibril width for a single fibril found in our study. The difference between 10 nm and 13 nm for the width of twinned fibrils may be related to the arrangement of the two filaments. If the two filaments are associated sidewise, this will give a larger width, i.e., in the range of 11-13 nm, than if the two filaments are partly on top of each other, which could explain the lower value of the width in the range of 9-10 nm observed in the present study. Bousset *et al.* (15) have reported cylindrical fibrils with a width of  $13 \pm 2$  nm, which may be caused by the lateral association of two to three filaments as discussed above.

Comparing our fibril morphology with that of Sidhu *et al.*, (17) we note that a. the height measured by AFM is comparable to the width we observe, and b. the lengths of periods differ. In Sidhu *et al.*, (17) at least 100 fibrils were measured and the periodicity given is averaged over the entire length of fibrils, selecting fibrils of minimally 1  $\mu$ m long each. Such details could not be obtained in the present study, where we compare a large number of samples. Therefore, the periodicity information from the present study is less reliable than the one in Sidhu *et al.* (17). In addition, the differences in imaging methods, AFM and TEM, may lead to systematic variations in the parameters observed here and in Sidhu *et al.* (17).

## Chapter 4

In conclusion, we observed that the fibrils of different protein constructs grown under seeded conditions are similar in morphology. We also found that the difference in morphology for the fibrils, grown from the same protein under the seeded conditions and the conditions described in (21), i.e., unseeded conditions, is larger compared to those observed between fibrils grown under the seeded conditions. For direct comparison with previously published fibril morphologies (14,15,17,24,25), observation of a larger number of fibrils, higher resolution techniques like cryo-electron microscopy (cryo-EM) and mass-per-length-ratio measurements by scanning transmission electron microscopy (STEM) (26) would be needed. These were beyond the scope of the present investigation.

### 4.5 References

1. Weinreb PH, Zhen W, Poon AW, Conway KA, Lansbury PT. NACP, a protein implicated in Alzheimer's disease and learning, is natively unfolded. *Biochemistry*. 1996;35:13709–13715.
2. Spillantini MG, Schmidt ML, Lee VM, Trojanowski JQ, Jakes R, Goedert M.  $\alpha$ -Synuclein in Lewy bodies. *Nature*. 1997;388:839–840.
3. Spillantini MG, Crowther RA, Jakes R, Hasegawa M, Goedert M.  $\alpha$ -Synuclein in filamentous inclusions of Lewy bodies from Parkinson's disease and dementia with Lewy bodies. *Proc Natl Acad Sci U S A*. 1998;95:6469–6473.
4. Conway KA, Harper JD, Lansbury PT. Accelerated in vitro fibril formation by a mutant  $\alpha$ -Synuclein linked to early-onset Parkinson disease. *Nat Med*. 1998;4:1318–1320.
5. El-Agnaf OM, Jakes R, Curran MD, Wallace A. Effects of the mutations Ala 30 to Pro and Ala 53 to Thr on the physical and morphological properties of  $\alpha$ -Synuclein protein implicated in Parkinson's disease. *FEBS Lett*. 1998;440:67–70.
6. Hashimoto M, Hsu LJ, Sisk A, Xia Y, Takeda A, Sundsmo M, Masliah E. Human recombinant NACP/ $\alpha$ -Synuclein is aggregated and fibrillated in vitro: Relevance for Lewy body disease. *Brain Res*. 1998;799:301–306.
7. Crowther RA, Jakes R, Spillantini MG, Goedert M. Synthetic filaments assembled from C-terminally truncated alpha-synuclein. *FEBS Lett*. 1998;436:309–12.

## Chapter 4

8. Hoyer W, Cherny D, Subramaniam V, Jovin TM. Impact of the acidic C-terminal region comprising amino acids 109–140 on  $\alpha$ -Synuclein aggregation in vitro. *Biochemistry*. 2004;43:16233–16242.
9. Yagi H, Kusaka E, Hongo K, Mizobata T, Kawata Y. Amyloid fibril formation of  $\alpha$ -Synuclein is accelerated by preformed amyloid seeds of other proteins: Implications for the mechanism of transmissible conformational diseases. *J Biol Chem*. 2005;280:38609–38616.
10. Goldsbury C, Frey P, Olivieri V, Aebi U, Müller SA. Multiple assembly pathways underlie amyloid- $\beta$  fibril polymorphisms. *J Mol Biol*. 2005;352:282–298.
11. Ionescu-Zanetti C, Khurana R, Gillespie JR, Petrick JS, Trabachino LC, Minert LJ, Carter SA, Fink AL. Monitoring the assembly of Ig light-chain amyloid fibrils by atomic force microscopy. *Proc Natl Acad Sci U S A*. 1999;96:13175–13179.
12. Lara C, Gourdin-bertin S, Adamcik J, Bolisetty S, Mezzenga R. Self-assembly of ovalbumin into amyloid and non- amyloid fibrils. *Biomacromolecules*. 2012;13:4213-4221.
13. Adamcik J, Jordens S. General self-assembly mechanism converting hydrolyzed globular proteins into giant multistranded amyloid ribbons. *Biomacromolecules*. 2011;12:1868–1875.
14. Vilar M, Chou H, Lührs T, Maji SK, Riek-Loher D, Verel R, Manning G, Stahlberg H, Riek R. The fold of  $\alpha$ -Synuclein fibrils. *Proc Natl Acad Sci U S A*. 2008;105:8637–8642.
15. Bousset L, Pieri L, Ruiz-Arlandis G, Gath J, Jensen PH, Habenstein B, Madiona K, Olieric V, Bockmann A, Meier BH, Melki R. Structural and functional characterization of two  $\alpha$ -Synuclein strains. *Nat Commun*. 2013;4:1-13.
16. Gath J, Bousset L, Habenstein B, Melki R, Böckmann A, Meier BH. Unlike twins: An NMR comparison of two  $\alpha$ -Synuclein polymorphs featuring different toxicity. *PLoS One*. 2014;9:1-11.
17. Sidhu A, Segers-Nolten I, Subramaniam V. Solution conditions define morphological homogeneity of  $\alpha$ -Synuclein fibrils. *Biochim Biophys Acta*. 2014;1844:2127–2134.
18. van Raaij ME, Segers-Nolten IMJ, Subramaniam V. Quantitative morphological analysis reveals ultrastructural diversity of amyloid fibrils from  $\alpha$ -Synuclein mutants. *Biophys J*. 2006;91:L96–L98.
19. Veldhuis G, Segers-Nolten I, Ferlemann E, Subramaniam V. Single-molecule FRET reveals structural heterogeneity of SDS-bound  $\alpha$ -Synuclein. *ChemBioChem*.

## Chapter 4

- 2009;10:436–439.
20. Drescher M, Godschalk F, Veldhuis G, van Rooijen BD, Subramaniam V, Huber M. Spin-label EPR on  $\alpha$ -Synuclein reveals differences in the membrane binding affinity of the two antiparallel helices. *ChemBioChem*. 2008;9:2411–2416.
  21. Hashemi Shabestari M, Kumar P, Segers-Nolten IMJ, Claessens MMAE, van Rooijen BD, Subramaniam V, Huber M. Three long-range distance constraints and an approach towards a model for the  $\alpha$ -Synuclein-fibril fold. *Appl Magn Reson*. 2015;46:369–388.
  22. Hashemi Shabestari M. Spin-label EPR on disordered and amyloid proteins. Thesis, Leiden University Repository. 2013.
  23. Crowther RA, Daniel SE, Goedert M. Characterisation of isolated  $\alpha$ -Synuclein filaments from substantia nigra of Parkinson's disease brain. *Neurosci Lett*. 2000;292:128–130.
  24. Heise H, Hoyer W, Becker S, Andronesi OC, Riedel D, Baldus M. Molecular-level secondary structure, polymorphism, and dynamics of full-length  $\alpha$ -Synuclein fibrils studied by solid-state NMR. *Proc Natl Acad Sci U S A*. 2005;102:15871-15876.
  25. Gath J, Habenstein B, Bousset L, Melki R, Meier BH, Böckmann A. Solid-state NMR sequential assignments of  $\alpha$ -Synuclein. *Biomol NMR Assign*. 2012;6:51–55.
  26. Tuttle MD, Comellas G, Nieuwkoop AJ, Covell DJ, Berthold DA, Kloepper KD, Courtney JM, Kim JK, Barclay AM, Kendall A, Wan W, Stubbs G, Schwieters CD, Lee VM, Goerge JM, Rienstra CM. Solid-state NMR structure of a pathogenic fibril of full-length human  $\alpha$ -Synuclein. *Nat Struct Mol Biol*. 2016;23:409–415.

## Appendix B to chapter 4

To check whether the difference in fibrillization conditions for  $\alpha$ S69/90 and  $\alpha$ S69/90 affects not only the morphology (see above), but also the internal structure, i.e., the fold of the protein inside fibrils, we performed DEER measurements on fibrils of  $\alpha$ S69/90 and  $\alpha$ S69/90. Figure B1 shows the comparison of the DEER traces of  $\alpha$ S69/90 and  $\alpha$ S69/90. The two traces look different. The modulation depth of  $\alpha$ S69/90 is larger than of  $\alpha$ S69/90 (see Table 5.2 in chapter 5). The modulation depth of  $\alpha$ S69/90 is small, therefore, the distance distribution of this sample is not meaningful, because only a small fraction of the spin population contributes to it. As both fibrillizations were made with the same protein batch, the difference in modulation depth shows that for  $\alpha$ S69/90, less spin-pairs are in the sensitive distance range of DEER (2 nm – 5 nm), which we interpret as a difference in the internal  $\alpha$ S-fold between the two types of fibrils,  $\alpha$ S69/90 and  $\alpha$ S69/90.

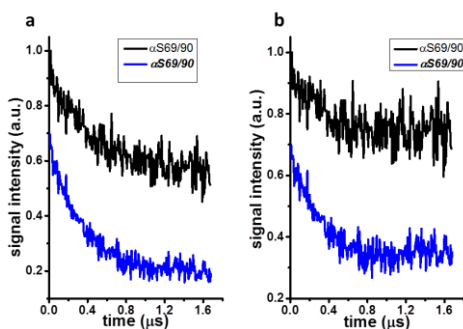


Figure B1. Comparison of DEER time traces of  $\alpha$ S 69/90 fibril samples prepared under different fibrillization conditions: a. DEER time traces of  $\alpha$ S69/90 (black lines) and  $\alpha$ S69/90 (blue lines) before background corrections, b. DEER time traces of both fibril samples after background correction (black line:  $\alpha$ S 69/90, blue lines:  $\alpha$ S 69/90) (for details see text). Both the DEER traces are normalized to one by dividing the traces by the maximum of their intensity. DEER traces are shifted vertically with respect to each other for better visibility.



## **5 Nanometer Distance Constraints for the Fold of $\alpha$ -Synuclein in Fibrils of Single Morphology**

### 5.1 Introduction

After Alzheimer's disease, Parkinson's disease (PD) (1) is the most highly spread neurodegenerative disease. This disease is characterized by the presence of intracellular protein inclusions, called Lewy bodies (2,3), in the brain of PD patients. Lewy bodies are largely composed of  $\alpha$ -Synuclein ( $\alpha$ S) (4,5). The protein  $\alpha$ S, which has a physiological function that is yet unknown, is 140 amino-acids long. It is an intrinsically disordered protein (6,7), which under certain conditions can form fibrils.

Amyloid fibrils have a cross  $\beta$ -sheet structure (8) shown schematically in Figure 5.1. In the fibril, each protein has a well-defined conformation. The protein is arranged into several consecutive  $\beta$ -strands that are connected by turns, as shown in Figure 5.1a. These individual  $\beta$ -strands, which run perpendicular to the fibril axis, combine to  $\beta$ -sheets, which are shown as colored planes in Figure 5.1b. The  $\beta$ -sheets grow in the direction of the fibril axis. The architecture of fibrils is more complex. Longer peptides, such as  $\alpha$ S can form multiple  $\beta$ -sheets and pairs of  $\beta$ -sheets can be at an angle to each other (9). Therefore, the fold of a protein such as  $\alpha$ S in the fibril is a challenging question. It is important to understand which residues are involved in the fibrillization and to identify interactions that hold the fibril together.

Solid-state nuclear magnetic resonance (ss-NMR) (10) and electron paramagnetic resonance (EPR) studies (11,12) have identified residues that are present in the  $\beta$ -sheets. Not all ss-NMR studies agreed on the extent of  $\beta$ -sheets, and several (13,14) showed doubling of NMR signals interpreted as polymorphism of the fibrils, i.e., different fibril forms in one sample. Polymorphism can influence the internal structure of fibrils (15).

## Chapter 5

Several studies (16–24) were done on the  $\alpha$ S fibril fold. Two studies (23,24) discuss the structure of  $\alpha$ S in the fibril at atomic resolution, employing the non-amyloid-beta-component (NAC) region of  $\alpha$ S. Recently, an ss-NMR study by Tuttle *et al.* (25) presented a model at atomic resolution of full-length  $\alpha$ S in fibrils.

Along with the structural information obtained from NMR studies, distance constraints in the nanometer range can be of great help to define the fibril fold, as shown recently for islet amyloid polypeptide (IAPP) (26). To obtain such long-range distance constraints, a pulsed EPR method, double electron-electron resonance (DEER) (27–30), is attractive. It can measure distances between 2 and 5 nm. In this work, we use DEER to obtain distances in the nanometer range, i.e., the intramolecular distances between two spins, from the fibrils of doubly spin-labelled  $\alpha$ S mutants.

To control the morphology of the fibrils, conditions are used that were optimized in (31) to obtain fibrils of single morphology. Fibril samples of all  $\alpha$ S spin-labelled constructs are grown by seeded fibrillization. A single batch of wt- $\alpha$ S seeds, which was grown as described in (31) (see Materials and methods), is used for each sample. In chapter 4, we described the characterization of the fibril morphology by transmission electron microscopy (TEM) and discussed our findings in detail, demonstrating that we are able to control the morphology of fibrils to a reasonable extent.

Similar to previous approaches (17,18,21,22), intramolecular distances are measured on doubly spin-labelled  $\alpha$ S. We prepared a set of nine double cysteine mutants and their respective single-cysteine references and labelled them with MTSL [(1-oxyl-2,2,5,5-tetramethylpyrroline-3-methyl)-methanethiosulfonate]. We refer to the doubly-labelled constructs as  $\alpha$ S42/69,  $\alpha$ S42/75,  $\alpha$ S42/85,  $\alpha$ S56/69,  $\alpha$ S56/75,  $\alpha$ S56/90,  $\alpha$ S69/85,  $\alpha$ S69/90, and  $\alpha$ S75/85 where the numbers denote

## Chapter 5

the labelling position in the protein sequence. As before (22), diamagnetic dilution was used, generating fibrils composed of 95 % wt- $\alpha$ S in case of doubly labelled  $\alpha$ S and 90 % for singly labelled  $\alpha$ S.

We show that long-range distance constraints for the  $\alpha$ S fibril fold can be obtained under conditions that promote fibrils of single morphology. We obtain nanometer distance constraints from eight doubly-labelled  $\alpha$ S constructs by DEER from pairs of residues that span the entire  $\beta$ -sheet region of  $\alpha$ S, from residue 42 to residue 90. We also compare our distances to distances obtained in previous DEER studies (18,21,22) and to two NMR studies (24,25) at atomic resolution of the  $\alpha$ S fibril fold.

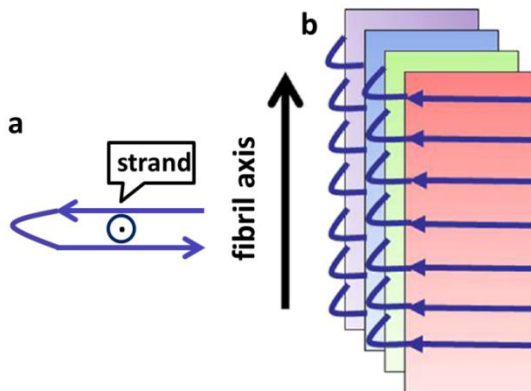


Figure 5.1. Schematic representation of the overall structure of amyloid fibrils. a: blue arrows represent a  $\beta$ -strand and the blue dot shows the direction of the fibril axis, which is pointing out of the page. b: the black arrow represents the direction of the fibril axis and colored planes depict the  $\beta$ -sheets. The Figure is modified from (22).

## Chapter 5

### 5.2 Materials and methods

#### 5.2.1 Expression and purification of cysteine mutants of the $\alpha$ -Synuclein protein

Single and double cysteine mutations were introduced into the  $\alpha$ S gene by site-directed mutagenesis. Mutants were expressed in the *Escherichia coli* strain BL21(DE3) and subsequently purified in the presence of 1 mM DTT (32,33). Prior to labelling,  $\alpha$ S mutants were reduced with a sixfold molar excess (per cysteine) of DTT for 30 min at room temperature. Subsequently, samples were desalted on Pierce Zeba5 mL desalting columns, followed by an immediate addition of a sixfold molar excess (per cysteine) of the MTSL spin label[(1-oxyl-2,2,5,5-tetramethylpyrroline-3-methyl)-methanethiosulfonate]and incubated for 1 h in the dark at room temperature. Free label was removed using two additional desalting steps. Protein samples were applied onto Microcon YM-100 spin columns to remove any precipitated and/or oligomerized proteins and diluted into 10 mM Tris-HCl, pH 7.4 to typical protein concentrations of approximately 0.25 mM (34).

#### 5.2.2 Preparation of $\alpha$ S fibril seeds

For seeds, we first prepared wild type (wt)  $\alpha$ S fibrils following the protocol from Sidhu *et al.* (31), described briefly. The wt- $\alpha$ S protein solution (concentration = 100  $\mu$ M, in 10 mM Tris-Cl buffer, pH 7.4, containing 10 mM NaCl and 0.1 mM EDTA) was aliquoted into 15 Eppendorf tubes (Eppendorf LoProtein Bind 2 ml), 500  $\mu$ l each. All tubes were incubated at a temperature of 37 °C shaking continuously at 500 rpm in a Thermo mixer (Eppendorf). The time evolution of  $\alpha$ S fibrillization was monitored by the standard Thioflavin T (ThioT) fluorescence assay. For each tube, fibrillization was stopped when the ThioT-fluorescence

## Chapter 5

intensity reached a plateau. The fibrillization was completed in 6-7 days. The content of each Eppendorf tube was divided into two samples of 250  $\mu$ l each, which were frozen quickly in liquid nitrogen and stored at  $-20$  °C. To start the seeded fibrillization experiment, one aliquot was thawed and sonicated in a bath sonicator (Branson 2510) for one minute to break the fibrils into seeds, which were then added to the samples to be fibrillized.

### 5.2.3 Seeded fibrillization of spin labelled $\alpha$ S and harvesting

We prepared the fibrils by mixing the monomeric  $\alpha$ S (spin-labelled and wild type  $\alpha$ S) with the wt- $\alpha$ S seeds. The total monomer concentration used for making fibrils was 100  $\mu$ M. To this mixture 2 % monomer-equivalent seeds were added. Diamagnetic dilution was employed to diminish the effect of intermolecular interaction. We used 1:20 (SL  $\alpha$ S:wt) diamagnetic dilution for all doubly labelled and 1:10 diamagnetic dilution for all singly labelled  $\alpha$ S. A typical sample for doubly labelled  $\alpha$ S consisted of 5  $\mu$ M spin-labelled  $\alpha$ S, 95  $\mu$ M wt- $\alpha$ S and 2  $\mu$ M  $\alpha$ S-monomer equivalent seeds. The total volume for each sample was 3.0 ml, which was aliquoted into five Eppendorf tubes and put on the thermomixer. The seeded fibrillization was performed under the same conditions as used for wt- $\alpha$ S fibrils (31). The time evolution of seeded fibrillization was monitored by the ThioT fluorescence assay. Most of the mutants completed the aggregation in 24 hours except for  $\alpha$ S69/90, which took 9 days. Seeded fibrils were harvested by ultracentrifugation for 45 min at 120000xg using a 70.1Ti rotor in a Beckman Coulter Ultracentrifuge. The fibril pellets were washed three times with the buffer used for fibrillization. The washed pellets were used for making samples for DEER measurements.

The spin concentration of spin-labelled protein was determined by comparing the double integral of the room temperature, liquid solution EPR spectrum to that of

## Chapter 5

a reference sample of known spin concentration. The protein concentration and the labelling degree are given for each sample in Table 5.1. To compensate for incompletely spin-labelled protein, actual protein concentrations used to make samples were calculated based on the amount of spin label in each protein. In Table 5.1, also the diamagnetic dilution is given that would result if the protein had been completely labelled.

Table 5.1. Protein concentrations in the  $\alpha$ S fibrillization solution and labelling degree of proteins

$\alpha$ S sample	fibril	labelling degree (%) <sup>a</sup>	concentration of spin-labelled protein ( $\mu$ M) <sup>b</sup>	concentration of wild type protein ( $\mu$ M) <sup>b</sup>	nominal diamagnetic dilution [SL $\alpha$ S : wt $\alpha$ S] <sup>c</sup>
$\alpha$ S42/69		55	9	91	1 : 11
$\alpha$ S42/75		48	10	90	1 : 10
$\alpha$ S42/85		62	8	92	1 : 12
$\alpha$ S56/69		73	7	93	1 : 14
$\alpha$ S56/75		56	9	91	1 : 11
$\alpha$ S56/90		55	9	91	1 : 11
$\alpha$ S69/85		82	6	94	1 : 17
$\alpha$ S69/90		85	6	94	1 : 17
$\alpha$ S75/85		60	8	92	1 : 12

**a:** Percentage relative to 100 % doubly spin-labelled protein. **b:** Protein concentration in the fibrillization solution. **c:** Diamagnetic dilution, if protein had been 100 % spin-labelled.

### 5.2.4 Transmission electron microscopy

Negative staining of the  $\alpha$ S-fibril samples was done by placing a fresh carbon-coated grid (200 meshes) on top of a drop (10  $\mu$ l) of the  $\alpha$ S-fibril solution for 2 minutes. The grid was then washed 3 times on a drop of distilled water.

## Chapter 5

Subsequently, the grids were placed directly on top of a small drop of 3.5 % uranyl acetate for 1.5 minutes and the excess uranyl acetate was blotted away by touching the grids to a filter paper at an angle of 45°. Afterwards the grids were placed in a Petri dish with filter paper to let them dry. The grids were examined with a FEI Technai-12 G2 Spirit Biotwin transmission electron microscope (FEI, Eindhoven, Netherlands) and micrographs were taken with a Veleta side-mounted TEM camera using Radius acquisition software (both Olympus Soft Imaging Solutions, Münster, Germany). Images were measured using the image processing feature within the Radius software package.

### 5.2.5 Continuous-wave EPR at 120 K

The 9.7 GHz cw-EPR measurements were performed using an ELEXYS E680 spectrometer (Bruker, Rheinstetten, Germany) with a rectangular cavity, using a modulation frequency of 100 kHz. For measurements at 120 K, a helium gas flow cryostat (Oxford Instruments, United Kingdom) with an ITC502 temperature controller (Oxford Instruments, United Kingdom) was used. For the measurements in frozen solution, 3 mm outer diameter quartz sample tubes were used. To obtain a frozen glass 20 % glycerol was added to the samples before freezing them in liquid nitrogen. The frozen samples were inserted in the pre-cooled helium gas flow cryostat. The EPR spectra were recorded using a modulation amplitude of 0.2 mT and a microwave power of 0.16 mW. Typical accumulation times were approximately 70 min.

### 5.2.6 DEER measurements

All DEER experiments were done at 9.5 GHz on an ELEXSYS E680 spectrometer (Bruker, Rheinstetten, Germany) using a 3 mm split-ring resonator (ER 4118XMS-3-W1). We performed the measurements at 40 K with a helium-gas flow using a

## Chapter 5

CF935 cryostat (Oxford Instruments, United Kingdom). The pump and observer frequencies were separated by 70 MHz and adjusted as reported before (35). The pump-pulse power was adjusted to invert the echo maximally (27–30). The pump-pulse length was set to 16 ns. The pulse lengths of the observer channel were 16 and 32 ns for  $\pi/2$ - and  $\pi$  - pulses, respectively. A phase cycle (+ x) - (- x) was applied to the first observer pulse. The complete pulse sequence is given by  $\frac{\pi}{2}_{\text{obs}} - \tau_1 - \pi_{\text{obs}} - t - \pi_{\text{pump}} - (\tau_1 + \tau_2 - t) - \pi_{\text{obs}} - \tau_2 - \text{echo}$ . The DEER time traces for ten different values of  $\tau_1$  spaced by 8 ns starting at  $\tau_1=200$  ns were added to suppress proton modulations. Typical accumulation times per sample were 14 - 17 hours.

### 5.2.6.1 DEER analysis

In order to analyze the DEER traces and extract the distance distributions, the software package “DeerAnalysis 2011” was used (36). Experimental background functions were derived from DEER traces of singly labelled  $\alpha$ S under conditions of diamagnetic dilution. The distance distribution was derived by the model free Tikhonov regularization (27–30,36). The width of the peaks were determined by fitting each individual peak of the distance distribution curve obtained from the DEER analysis using a Gaussian fit function provided in Origin non-linear curve fitting tools (Origin Pro 9).

### 5.2.7 MMM analysis

To compare the distances obtained in the present study with recently reported models of the  $\alpha$ S fibrils (25) and their core (24), we used the multiscale modeling of macromolecular systems (MMM) software (MMM version 2013)(37). It enables

## Chapter 5

to model the spin-label linker conformation at the desired positions of the protein to determine the distance distribution for each pair of spin-labels.

### 5.3 Results

The details of the results of the morphology of fibrils are described in chapter 4 of this thesis. Figure 5.2 shows TEM images of the fibrils grown for the present study. All fibrils were prepared using one batch of seeds and conditions described in Materials and methods. Single fibrils have a width of  $5.6 \pm 1$  nm (Figure 5.2f, black arrows) and are often found to twin with another fibril that runs parallel to generate a width of 9 -10 nm (see Figure 5.2a, black arrows). Many of these twinned fibrils are twisted, as indicated in Figures 2c and 2f by white arrows, showing a periodicity around 170 nm, 240 nm, and 290 nm.

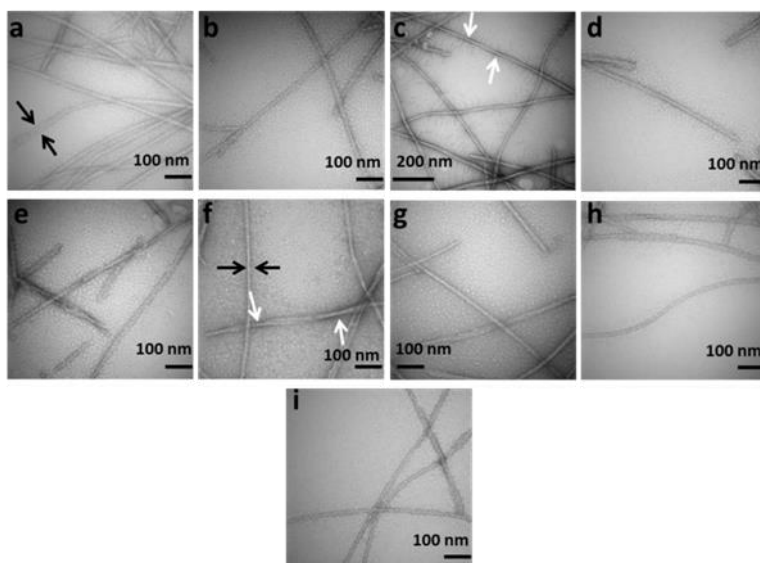


Figure 5.2. Morphological characterization of  $\alpha$ S fibrils used in this study: Negative stain transmission electron microscopy (TEM) images of a.  $\alpha$ S42/69, b.  $\alpha$ S42/75, c.  $\alpha$ S42/85, d.  $\alpha$ S56/69, e.  $\alpha$ S56/75, f.  $\alpha$ S56/90, g.  $\alpha$ S69/85, h.  $\alpha$ S75/85, and i.  $\alpha$ S69/90. Black arrows indicate the width of the twinned fibril (a) and of the single fibril (f), while the white arrows at a twist show the points between which the periodicity of twists was measured.

## Chapter 5

### 5.3.1 DEER results

In Figure 5.3a, the DEER time traces of fibrils grown from the doubly spin-labelled proteins are shown. The traces look different. Almost all DEER traces have a slow initial decay showing the absence of short distances. In Figure 5.3b the DEER time traces of  $\alpha$ S56/69 and  $\alpha$ S56/90 fibrils fibrillized under conditions employed in the present study (for details, see Materials and methods) are compared to those described by Hashemi Shabestari *et al.*(22). For clarity, from now on, we use the nomenclature  **$\alpha$ S56/69** and  **$\alpha$ S56/90** for  $\alpha$ S56/69 and  $\alpha$ S56/90 fibrils described in Hashemi Shabestari *et al.*(22). The DEER trace of  **$\alpha$ S56/69** (22) shows a fast initial decay, which is absent in the trace of  $\alpha$ S56/69 fibrils. Also the respective traces of the fibrils from  $\alpha$ S56/90 differ. The trace of  **$\alpha$ S56/90** has a fast decay component that is absent in the trace of  $\alpha$ S56/90 fibrils.

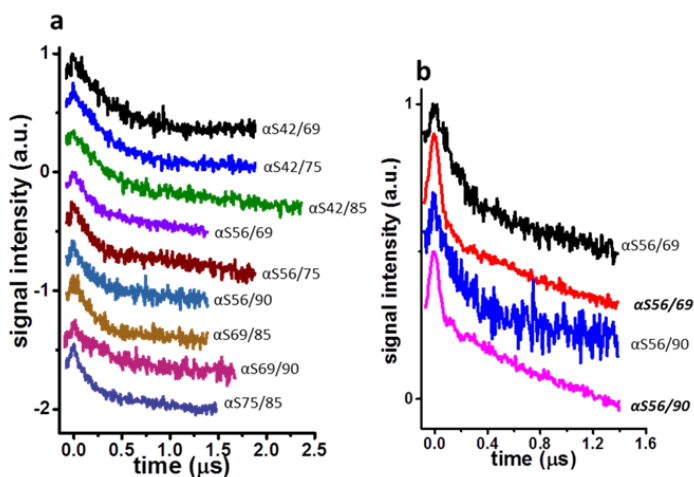


Figure 5.3. DEER time traces of  $\alpha$ S fibril samples: a.  $\alpha$ S fibril samples grown under seeded conditions, b. comparison of DEER time trace of  $\alpha$ S56/69 with  **$\alpha$ S56/69** and  $\alpha$ S56/90 with  **$\alpha$ S56/90**.  **$\alpha$ S56/69** and  **$\alpha$ S56/90** stand for fibrils of  $\alpha$ S56/69 and  $\alpha$ S56/90 respectively grown under conditions described by Hashemi Shabestari *et al.*(22). All traces are normalized, i.e., the maximum echo intensity is set to one and the traces are shifted vertically for better visibility.

## Chapter 5

In Figure 5.4, the steps of the analysis of DEER traces are shown. Figure 5.4a shows the DEER traces along with the background trace derived from a 1:1 addition of the DEER curves of the respective singly labelled  $\alpha$ S variants. Figure 5.4b shows the background-corrected data and the fits corresponding to the distance distributions shown in Figure 5.4c, d, and e. The modulation depths and the parameters of the distance distributions are given in Table 5.2. For most of the  $\alpha$ S mutants the modulation depth is 0.3 to 0.5, showing that the majority of the spin labels in the sample are involved in a two-spin interaction.

Fibrils of  $\alpha$ S69/90 have DEER traces with a comparatively low modulation depth, i.e., around 0.2. This low modulation depth shows that the number of coupled spins contributing to the distance distribution is low, which indicates that a significant population of the protein has a conformation with distances outside the DEER measurement range, i.e., distances shorter than 2 nm or longer than 5 nm. Therefore, we did not process the DEER data of the  $\alpha$ S69/90 fibril sample further. The distance distributions of the  $\alpha$ S variants  $\alpha$ S42/69,  $\alpha$ S42/75, and  $\alpha$ S56/69 show two peaks and the remaining ones have just one peak. Most of the peaks in the distance distributions have a width of approximately 0.8 nm (Table 5.2).

## Chapter 5

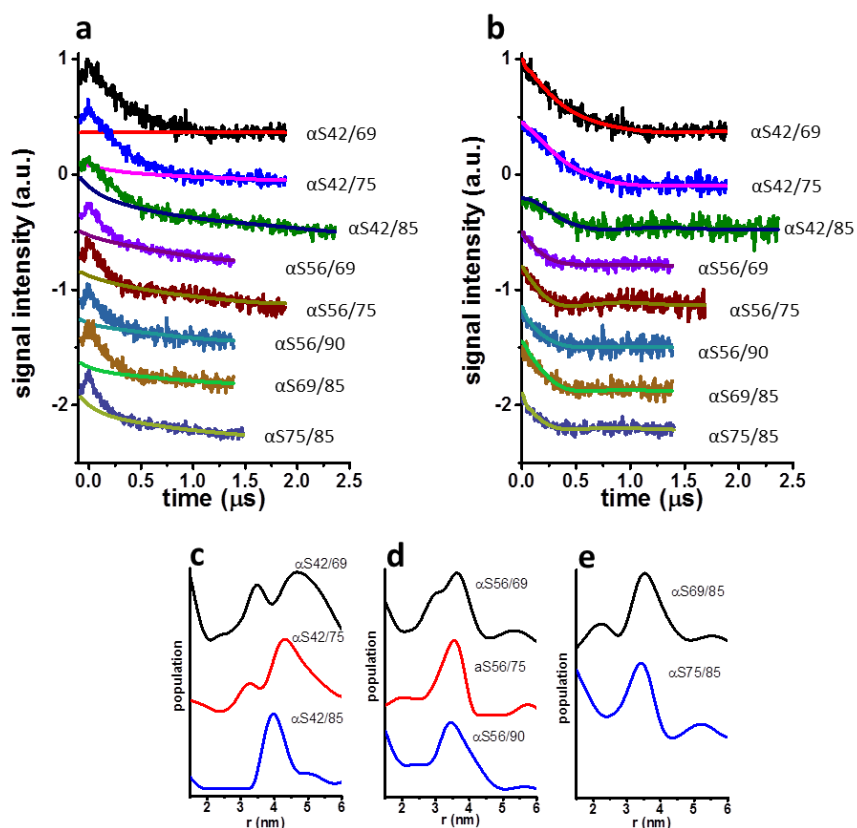


Figure 5.4. DEER analysis for  $\alpha$ S fibril samples: a. DEER time traces with experimental background, b. DEER time traces after background correction along with the fits corresponding to the distance distributions shown in c, d, and e; c. for  $\alpha$ S42/69 (black),  $\alpha$ S42/75 (red) and  $\alpha$ S42/85 (blue), d. for  $\alpha$ S56/69 (black),  $\alpha$ S56/75 (red) and  $\alpha$ S56/90 (blue), and e. for  $\alpha$ S69/85 (black),  $\alpha$ S75/85 (blue); distance distributions were derived from the DEER data after Tikhonov regularization with regularization parameter  $\alpha$  of 1000. The DEER data of the  $\alpha$ S69/90 fibril sample is not included because of the low modulation depth (see Table 5.2). All traces are normalized (maximum echo intensity is one) and shifted vertically for better visibility.

Figure 5.5 shows the distance distributions of  $\alpha$ S56/69 and  $\alpha$ S56/90 fibril samples described in (22) in comparison with those of  $\alpha$ S56/69 and  $\alpha$ S56/90. In (22), intramolecular distances found were 2.1 nm (for  $\alpha$ S56/69) and 3.4 nm ( $\alpha$ S56/90).

## Chapter 5

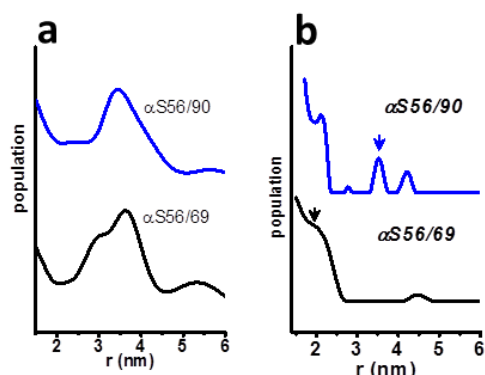


Figure 5.5. Comparison of distance distribution of fibrils of a)  $\alpha$ S56/90, and  $\alpha$ S56/69, grown under the conditions in the present study with b)  $\alpha$ S56/90, and  $\alpha$ S56/69, described in (22). Arrow depicts the intramolecular distances for b. For a, distances are shown in Table 5.2.

Table 5.2. Parameters of distance distributions of  $\alpha$ S fibrils. FWHM: Full width at half maximum (for details, see Materials and methods). The modulation depth of the DEER trace is obtained from DEER analysis, the distances and the width from Gaussian fits to the individual peaks of the distance distribution (for details see Materials and methods)

$\alpha$ S variants	modulation depth	distances (nm) and FWHM (nm) of peaks				cw-EPR line broadening <sup>a</sup>
		peak 1	FWHM	peak 2	FWHM	
$\alpha$ S42/69	0.49	3.4	0.5	4.6	1.4	no
$\alpha$ S42/75	0.55	3.3	0.8	4.3	0.8	no
$\alpha$ S42/85	0.25	4.0	0.7	na	na	no
$\alpha$ S56/69	0.25	3.0	0.9	3.7	0.7 <sup>b</sup>	no
$\alpha$ S56/75	0.32	3.5	0.8	na	na	yes
$\alpha$ S56/90	0.33	3.5	1.1	na	na	yes
$\alpha$ S69/85	0.39	3.5	0.9	na	na	yes
$\alpha$ S75/85	0.29	3.4	0.8	na	na	no
$\alpha$ S69/90	0.21	modulation depth too low for meaningful distance distributions				no

na: not applicable; **a**: see appendix C; **b**: analysis with two peaks is probably not meaningful given the small separation and the large width, i.e., FWHM, of each peak.

### 5.3.2 MMM derived distance distributions

The experimentally measured distances are between the nitroxide groups of two spin labels. The spin-label linker, which separates the nitroxide from the protein backbone, is about 0.5 nm in length and also flexible. Therefore, the spin-label linker length and flexibility has to be taken into account to compare the distance measured by DEER to the fibril structure from crystallography or NMR studies. Spin-label linker conformations were calculated by the rotamer-library based method with the multiscale modeling of macromolecular systems (MMM) software (37). The experimental distance distributions were compared with the MMM simulations of the distance distributions based on the fibril structure published recently by Tuttle *et al.* (25) (PDB accession number: 2N0A).

Figure 5.6 shows the experimental DEER traces of all  $\alpha$ S fibrils used in the present study and their corresponding distance distributions in comparison to those derived from MMM. To distance distributions derived from MMM, we refer as MMM distance distributions. All MMM distance distributions have narrower peaks than the experimental ones. For  $\alpha$ S42/69 (a),  $\alpha$ S42/75 (b),  $\alpha$ S42/85 (c),  $\alpha$ S56/69 (d), and  $\alpha$ S56/75 (e), the MMM distance agrees with one of the experimentally observed distances, while for  $\alpha$ S56/90 (f),  $\alpha$ S69/85 (g), and  $\alpha$ S75/85 (i), no such agreement can be seen. The short MMM distance for  $\alpha$ S69/90 suggests broadening of the cw-EPR spectra, which is not observed experimentally (see Table 5.2).

## Chapter 5

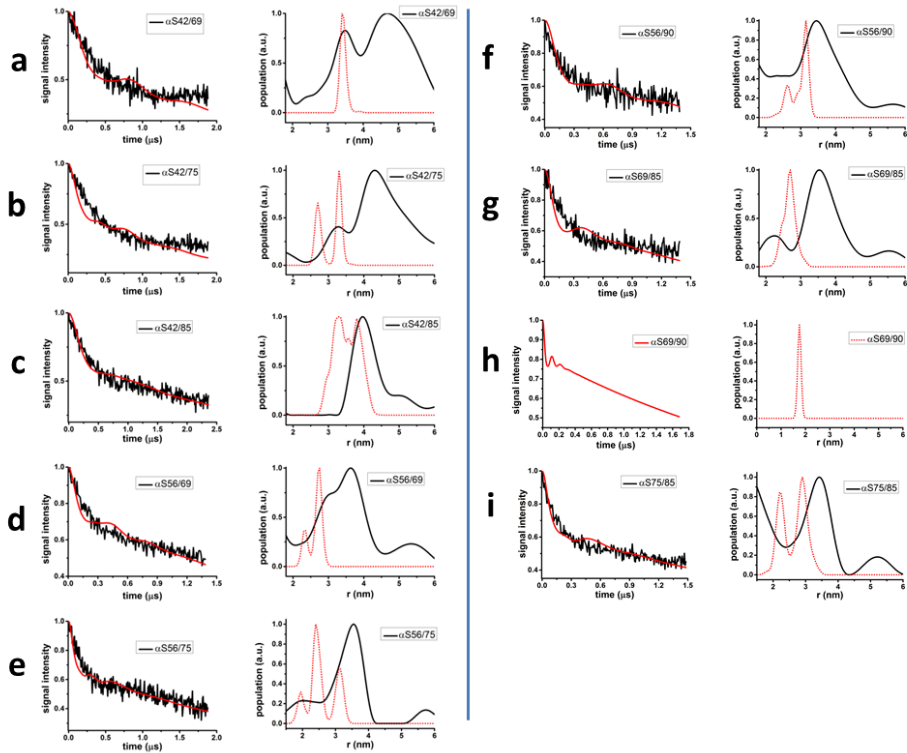


Figure 5.6. Comparison of DEER experimental data with those derived by simulation from the PDB structure of  $\alpha$ S-fibril, which we refer to as the Rienstra model (25) (Accession no: 2N0A) using the MMM analysis package: Superposition of experimental DEER traces of  $\alpha$ S fibrils and their distance distributions (both shown as a black line) with MMM DEER traces (red line) and their distance distributions (shown as a red dotted line) respectively derived from MMM analysis. a.  $\alpha$ S42/69, b.  $\alpha$ S42/75, c.  $\alpha$ S42/85, d.  $\alpha$ S56/69, e.  $\alpha$ S56/75, f.  $\alpha$ S56/90, g.  $\alpha$ S69/85, h.  $\alpha$ S69/90, and i.  $\alpha$ S75/85.

### 5.4 Discussion

We have investigated fibrils of a set of SL- $\alpha$ S variants containing two spin labels, for which fibrils of SL- $\alpha$ S variants containing one spin label are also needed. Using seeded fibrillization with seeds derived from one batch of wild-type  $\alpha$ S grown under the conditions optimized in (31), we avoid polymorphism as much as possible.

## Chapter 5

The detailed study of the morphology of fibrils is described in chapter 4 of this thesis. Transmission electron microscopy on all doubly labelled fibrils used in the present study shows similarity in their morphologies (see Figure 5.2). We observe differences in the periods of the twists, however, as described in chapter 4, the small number of observations and the difficulty in detecting the cross-over points makes it difficult to determine period lengths accurately. The remaining parameters show that the fibril morphology is similar for all constructs, assuring that distances from all constructs relate to one fibril-morphology.

### 5.4.1 Distances from DEER experiments

Distances are obtained between eight pairs of residues, which cover the entire fibril core of  $\alpha$ S. The distances are listed in Table 5.2, from which we discuss a few peculiarities. One is the  $\alpha$ S69/90 mutant that has a low modulation depth, which indicates distances outside the sensitivity range of DEER. We exclude short distances because of the absence of line broadening in cw-EPR spectra (see appendix C) and therefore conclude that the distance between residue 69 and 90 is larger than 4 nm.

The distance distributions of  $\alpha$ S42/69 and  $\alpha$ S42/75 (Figure 5.4c, top two traces) show two distances, although, under normal circumstances, only one distance is expected. Intermolecular distances, i.e., distances between spin labels at different proteins in the fibril could be a source of additional distances. Intermolecular interactions would also increase the modulation depth, which is relatively high for  $\alpha$ S42/69, and  $\alpha$ S42/75. Intermolecular interactions could be stronger for  $\alpha$ S42/69,  $\alpha$ S42/75,  $\alpha$ S56/75, and  $\alpha$ S56/90 because the degree of spin-labelling of the starting protein was low in these samples. The low degree of labelling was compensated for by adding relatively more spin-labelled protein to the sample

## Chapter 5

(see Materials and methods, and Table 5.1). If the degree of labelling is low because both spin-label positions are incompletely labelled to the same degree, for example label position 1, 50 % and position 2, 50 %, no complication arises, but if the spin-labelled protein contains a substantial amount of protein that is only singly labelled, a lower contribution of intramolecular distances results, giving a larger contribution of intermolecular versus intramolecular interactions. Therefore, one of the two distance peaks observed in DEER for  $\alpha$ S42/69 and  $\alpha$ S42/75 might be due to intermolecular interactions. For the  $\alpha$ S56/75 and the  $\alpha$ S56/90 mutants, we attribute the short distance component observed by broadening of the cw-EPR spectra (see appendix C) to intermolecular interactions. Additional experiments, starting with protein of higher degree of labelling, and fibrils prepared with higher diamagnetic dilution would be needed to decide which of the distances in the distributions of these mutants are inter or intramolecular.

While annoying, the setup of the present study made it impossible to avoid these complications. The ultimate goal, to use these long-range constraints to build and test atomic models of the fibril fold, requires a large number of double mutants, fibrillized under single morphology conditions, making it impossible to optimize every single set of double-mutant DEER measurements. In the analysis so far and for future model building, we take into account that some distances can be intermolecular. Obviously, atomic models can also find inconsistencies in the distances, which arise from the experimental limitations. Therefore, we expect to refine the interpretation in the future.

## Chapter 5

### 5.4.2 Comparison with DEER distances from other studies

Previously, in our lab, we performed DEER experiments on  $\alpha$ S fibrils (22). These fibrils were grown under different conditions than used in the present study. The distances are compared in Table 5.3.

Table 5.3. Comparison of  $\alpha$ S fibril distances from the present study with those from Hashemi Shabestari *et al.* (22)

spin-label positions	distances (nm) from the present study		distances (nm) (22)
	peak 1	peak 2	
$\alpha$ S56/69	3.0	3.7	2.1 nm
$\alpha$ S56/90	3.5		3.4 nm
$\alpha$ S69/90	> 4.0 nm		> 4.0 nm

For the  $\alpha$ S56/69 mutant, the distances differ. For  **$\alpha$ S56/69**, the distance of 2.1 nm dominates (Figure 5.5b, and Table 5.3), whereas  $\alpha$ S56/69 has distances of 3.0 nm and 3.7 nm (Figure 5.5a, and Table 5.3). For  $\alpha$ S56/90 and  $\alpha$ S69/90 (Table 5.3), similar distances are found, however the width of the distance distribution of  $\alpha$ S56/90 in the present study is larger than the one in (22) (see Figure 5.5a and b). Because of the large differences in DEER results for  $\alpha$ S56/69 and  $\alpha$ S56/90, we conclude that not only the morphology (chapter 4) of the fibrils differs, but also the protein fold is different for the two forms.

Next, we compare our distances with the distances reported by Pornsuwan *et al.* (21). They reported seven DEER distances. Only one pair has spin labels at positions similar to the ones measured in the present study. This is  $\alpha$ S54/90 in (21) and  $\alpha$ S56/90 in the present case. Pornsuwan *et al.* (21) reported the distance of 2.35 nm for  $\alpha$ S54/90, whereas  $\alpha$ S56/90 in the present study has the distance of

## Chapter 5

3.5 nm. The difference of 1.0 nm is large considering that 54 and 56 are only two residues apart in the sequence, and would point in the same direction of the strand, if they were on the same strand. The difference in distance of the pair  $\alpha$ S56/90 and  $\alpha$ S54/90 suggests that the protein folds are different. To be sure, an atomic resolution model for the fold derived from our study or (21) is needed, because against such a model, all measured distances can be compared.

### 5.4.3 Comparison with recently published structural models

Three structural models were published recently: a. An NMR study yielding atomic coordinates for full-length  $\alpha$ S, which we refer to as the Rienstra model (25), b. A model based on shorter  $\alpha$ S-fragments that form fibrils and were crystallized, which we refer to as the Eisenberg model (24), and c. a molecular dynamics (MD) simulation study of fibrils (23). We compare our data to the first two models. We used the published coordinates and modeled the spin-label linker using the MMM program (37).

#### 5.4.3.1 Comparison with the Rienstra model (25) for the $\alpha$ S fibril fold

The Rienstra model (25) describes the structure of  $\alpha$ S fibrils at atomic-resolution level. Using distance constraints derived from solid-state NMR, atomic coordinates of the  $\alpha$ S fibril fold (pdb file: 2N0A (25)) are given. For this structure we calculated the spin-label linker conformations with MMM (37), as described in the Results section.

Overall the MMM distances derived from the ss-NMR study do not agree well with the measured ones. This is most obvious for  $\alpha$ S56/69,  $\alpha$ S56/75,  $\alpha$ S56/90,  $\alpha$ S69/85, and  $\alpha$ S75/85. For none of these positions the experimentally

## Chapter 5

determined distances agree with those predicted from the structure. For  $\alpha$ S69/90, the short distance predicted is just in the range where cw-EPR line broadening is small and DEER is not sensitive (38), so it could be compatible with the experimental observation. For  $\alpha$ S42/85, the majority of the MMM predicted distance range is outside the experimental one, and only for  $\alpha$ S42/69 and  $\alpha$ S42/75, the MMM distances fall within one of the two distance peaks observed experimentally. For the latter two mutants, the respective distance distributions could be compatible, if one would assume that the second peak is due to an intermolecular distance.

In view of the overall disagreement, it seems possible that ss-NMR probes a different fibril fold than the present study. A different fold could be explained by the different fibrillization conditions used in (25), and be compatible with differences in the fibril morphology described in (25). To be sure, further experiments would be needed, such as a more detailed EM study on the fibrils of the present study.

### 5.4.3.2 Comparison with the Eisenberg model (24)

The Eisenberg model (24) describes the structure of the toxic core (called the NACore) of  $\alpha$ S at atomic-resolution level, derived from micro-electron diffraction. This model (24) represents the  $\alpha$ S fibril fold for residues 42 to 83 generated from the shorter fragments crystallized. We use MMM to derive distance distributions and compare with the distances from the present study (see Table 5.4)

## Chapter 5

Table 5.4. Comparison of distances from the present study with the distances derived from the model described in (24) using MMM.

mutants	distances (nm) in the present study		distances (nm) <sup>a</sup>	agreement
	peak 1	peak 2		
$\alpha$ S42/69	3.4	4.6	4.3	yes
$\alpha$ S42/75	3.3	4.3	3.2	yes
$\alpha$ S56/69	3.0	3.7	1.2	no
$\alpha$ S56/75	3.5	na	2.1	no

a: distances obtained from the Eisenberg model (24) using MMM

Because the Eisenberg model comprises only residues from 42 to 83, only four of our DEER distances (Table 5.4) can be compared to the model.

For  $\alpha$ S42/69, one of the two distance peaks, the one at 4.6 nm (Figure 5.4c) is in agreement with the distance of 4.3 nm derived from the Eisenberg model by MMM. A similar situation occurs for  $\alpha$ S42/75, where one of the two distances, 3.2 nm agrees with the distance from the Eisenberg model. The distances from the other two doubly labelled  $\alpha$ S ( $\alpha$ S56/69 and  $\alpha$ S56/75) do not agree with the ones from the Eisenberg model. Therefore, we consider our distances not compatible with the Eisenberg model (24). The reason may lie in the fact that the model by Eisenberg is generated from fibrils of short fragments of  $\alpha$ S. Long range interactions of  $\alpha$ S may not be well-represented in that model.

In this study, we show that long-range distance constraints for the  $\alpha$ S fibril fold can be obtained under conditions that promote fibrils of single morphology. We

## Chapter 5

show that the present results are not compatible with the recently published structural models for the  $\alpha$ S fibril fold (24,25) in certain aspects. Whether this is due to the limitations of the present study or really reflects a difference in the fibril fold remains to be determined. Several approaches for developing DEER data of fibrils into a model for the fibril fold are possible (22,26) and we will pursue them in the future.

### 5.5 References

1. Parkinson J. *An Essay on the Shaking Palsy* (Whitingham and Rowland, London). 1817.
2. Junn E, Ronchetti RD, Quezado MM, Kim S-Y, Mouradian MM. Tissue transglutaminase-induced aggregation of  $\alpha$ -Synuclein: Implications for Lewy body formation in Parkinson's disease and dementia with Lewy bodies. *Proc Natl Acad Sci U S A*. 2003;100:2047–2052.
3. Chung KK, Zhang Y, Lim KL, Tanaka Y, Huang H, Gao J, Ross CA, Dawson VL, Dawson TM. Parkin ubiquitinates the  $\alpha$ -Synuclein-interacting protein, synphilin-1: Implications for Lewy-body formation in Parkinson disease. *Nat Med*. 2001;7:1144–1150.
4. Spillantini MG, Schmidt ML, Lee VM, Trojanowski JQ, Jakes R, Goedert M.  $\alpha$ -Synuclein in Lewy bodies. *Nature*. 1997;388:839–840.
5. Spillantini MG, Crowther RA, Jakes R, Hasegawa M, Goedert M.  $\alpha$ -Synuclein in filamentous inclusions of Lewy bodies from Parkinson's disease and dementia with Lewy bodies. *Proc Natl Acad Sci U S A*. 1998;95:6469–6473.
6. Dunker AK, Lawson JD, Brown CJ, Williams RM, Romero P, Oh JS, Oldfield CJ, Campen AM, Ratliff CM, Hipps KW, Ausio J, Nissen MS, Reeves R, Kang C, Kissinger CR, Bailey RW, Griswold MD, Chiu W, Garner EC, Obradovic Z. Intrinsically disordered protein. *J Mol Graph Model*. 2001;19:26–59.
7. Dyson HJ, Wright PE. Intrinsically unstructured proteins and their functions. *Nat Rev Mol Cell Biol*. 2005;6:197–208.
8. Fändrich M. On the structural definition of amyloid fibrils and other polypeptide aggregates. *Cell Mol Life Sci*. 2007;64:2066–2078.

## Chapter 5

9. Margittai M, Langen R. Fibrils with parallel in-register structure constitute a major class of amyloid fibrils: Molecular insights from electron paramagnetic resonance spectroscopy. *Q Rev Biophys.* 2008;41:265-297.
10. Heise H, Hoyer W, Becker S, Andronesi OC, Riedel D, Baldus M. Molecular-level secondary structure, polymorphism, and dynamics of full-length  $\alpha$ -Synuclein fibrils studied by solid-state NMR. *Proc Natl Acad Sci U S A.* 2005;102:15871-15876.
11. Der-Sarkissiant A, Jao CC, Chen J, Langen R. Structural organization of  $\alpha$ -Synuclein fibrils studied by site-directed spin labeling. *J Biol Chem.* 2003;278:37530-37535.
12. Chen M, Margittai M, Chen J, Langen R. Investigation of  $\alpha$ -Synuclein fibril structure by site-directed spin labeling. *J Biol Chem.* 2007;282:24970-24979.
13. Heise H, Celej MS, Becker S, Riedel D, Pelah A, Kumar A, Jovin TM, Baldus M. Solid-state NMR reveals structural differences between fibrils of wild-type and disease-related A53T mutant  $\alpha$ -Synuclein. *J Mol Biol.* 2008;380:444-450.
14. Bousset L, Pieri L, Ruiz-Arlandis G, Gath J, Jensen PH, Habenstein B, Madiona K, Olieric V, Bockmann A, Meier BH, Melki R. Structural and functional characterization of two  $\alpha$ -Synuclein strains. *Nat Commun.* 2013;4:1-13.
15. Fändrich M, Meinhardt J, Grigorieff N. Structural polymorphism of Alzheimer A $\beta$  and other amyloid fibrils. *Prion.* 2009;3:89-93.
16. Vilar M, Chou H, Lührs T, Maji SK, Riek-Loher D, Verel R, Manning G, Stahlberg H, Riek R. The fold of  $\alpha$ -Synuclein fibrils. *Proc Natl Acad Sci U S A.* 2008;105:8637-8642.
17. Karyagina I, Becker S, Giller K, Riedel D, Jovin TM, Griesinger C, Bennati M. Electron paramagnetic resonance spectroscopy measures the distance between the external  $\beta$ -strands of folded  $\alpha$ -Synuclein in amyloid fibrils. *Biophys J.* 2011;101:L1-L3.
18. Hashemi Shabestari M, Segers-Nolten IMJ, Claessens MMAE, van Rooijen BD, Subramaniam V, Huber M. Elucidating the  $\alpha$ -Synuclein fibril fold by pulsed EPR. *Biophys J.* 2012;102:454a.
19. Gath J, Habenstein B, Bousset L, Melki R, Meier BH, Böckmann A. Solid-state NMR sequential assignments of  $\alpha$ -Synuclein. *Biomol NMR Assign.* 2012;6:51-55.
20. Comellas G, Lemkau LR, Zhou DH, George JM, Rienstra CM. Structural intermediates during  $\alpha$ -Synuclein fibrillogenesis on phospholipid vesicles. *J Am Chem Soc.* 2012;134:5090-5099.
21. Pornsuwan S, Giller K, Riedel D, Becker S, Griesinger C, Bennati M. Long-range

## Chapter 5

- distances in amyloid fibrils of  $\alpha$ -Synuclein from PELDOR spectroscopy. *Angew Chemie-Int Ed.* 2013;52:10290–10294.
22. Hashemi Shabestari M, Kumar P, Segers-Nolten IMJ, Claessens MMAE, van Rooijen BD, Subramaniam V, Huber M. Three long-range distance constraints and an approach towards a model for the  $\alpha$ -Synuclein-fibril fold. *Appl Magn Reson.* 2015;46:369–388.
  23. Atsmon-Raz Y, Miller Y. A proposed atomic structure of the self-assembly of the non-amyloid- $\beta$  component of human  $\alpha$ -Synuclein as derived by computational tools. *J Phys Chem B.* 2015;119:10005–10015.
  24. Rodriguez JA, Ivanova MI, Sawaya MR, Cascio D, Reyes FE, Shi D, Sangwan S, Guenther EL, Johnson LM, Zhang M, Jiang L, Arbing MA, Nannenga BL, Hattne J, Whittelegge J, Brewster AS, Messerschmidt M, Boutet S, Sauter NK, Gonen T, Eisenberg DS. Structure of the toxic core of  $\alpha$ -Synuclein from invisible crystals. *Nature.* 2015;525:486–490.
  25. Tuttle MD, Comellas G, Nieuwkoop AJ, Covell DJ, Berthold DA, Kloepper KD, courtney JM, Kim JK, Barclay AM, Kendall A, Wan W, Stubbs G, Schwieters CD, Lee VM, Goerge JM, Rienstra CM. Solid-state NMR structure of a pathogenic fibril of full-length human  $\alpha$ -Synuclein. *Nat Struct Mol Biol.* 2016;23:409–415.
  26. Bedrood S, Li Y, Isas JM, Hegde BG, Baxa U, Haworth IS, Langen R. Fibril structure of human islet amyloid polypeptide. *J Biol Chem.* 2012;287:5235–5241.
  27. Jeschke G. Distance measurements in the nanometer range by pulse EPR. *ChemPhysChem.* 2002;3:927–932.
  28. Jeschke G. Determination of the Nanostructure of Polymer Materials by Electron Paramagnetic Resonance Spectroscopy. *Macromol Rapid Commun.* 2002;23:227–246.
  29. Jeschke G, Koch A, Jonas U, Godt A. Direct conversion of EPR dipolar time evolution data to distance distributions. *J Magn Reson.* 2002;155:72–82.
  30. Jeschke G, Polyhach Y. Distance measurements on spin-labelled biomacromolecules by pulsed electron paramagnetic resonance. *Phys Chem Chem Phys.* 2007;9:1895-1910.
  31. Sidhu A, Segers-Nolten I, Subramaniam V. Solution conditions define morphological homogeneity of  $\alpha$ -Synuclein fibrils. *Biochim Biophys Acta.* 2014;1844:2127–2134.
  32. van Raaij ME, Segers-Nolten IMJ, Subramaniam V. Quantitative morphological analysis reveals ultrastructural diversity of amyloid fibrils from  $\alpha$ -Synuclein

## Chapter 5

- mutants. *Biophys J.* 2006;91:L96–L98.
33. Veldhuis G, Segers-Nolten I, Ferlemann E, Subramaniam V. Single-molecule FRET reveals structural heterogeneity of SDS-bound  $\alpha$ -Synuclein. *ChemBioChem.* 2009;10:436–439.
  34. Drescher M, Godschalk F, Veldhuis G, van Rooijen BD, Subramaniam V, Huber M. Spin-label EPR on  $\alpha$ -Synuclein reveals differences in the membrane binding affinity of the two antiparallel helices. *ChemBioChem.* 2008;9:2411–2416.
  35. Drescher M, Veldhuis G, Van Rooijen BD, Milikisyants S, Subramaniam V, Huber M. Antiparallel arrangement of the helices of vesicle-bound  $\alpha$ -Synuclein. *J Am Chem Soc.* 2008;130:7796–7797.
  36. Jeschke G, Chechik V, Ionita P, Godt A, Zimmermann H, Banham J, Timmel CR, Hilger D, Jung H. DeerAnalysis2006 - a comprehensive software package for analyzing pulsed ELDOR data. *Appl Magn Reson.* 2006;30:473–498.
  37. Polyhach Y, Bordignon E, Jeschke G. Rotamer libraries of spin labelled cysteines for protein studies. *Phys Chem Chem Phys.* 2011;13:2356–2366.
  38. Banham JE, Baker CM, Ceola S, Day IJ, Grant GH, Groenen EJJ, Rodgers CT, Jeschke G, Timmel CR. Distance measurements in the borderline region of applicability of CW EPR and DEER: A model study on a homologous series of spin-labelled peptides. *J Magn Reson.* 2008;191:202–218.

### *Appendix C to chapter 5*

The DEER method is not sensitive to short distances, which under the conditions of the experiments in chapter 5, applies to distances below 2 nm. Therefore, it is customary to complement DEER experiments with low temperature cw-EPR, as the latter method reveals short distances between spins, i.e., distances below 2 nm by spectral line broadening. To detect this broadening, reference spectra are needed that give the lineshape in the absence of spin-spin interaction. For the samples investigated here, the reference spectra are the spectra of 1:1 mixture of spectra of the respective singly labelled  $\alpha$ S-fibril-reference spectra. Spectra of some of the fibrillized singly spin-labeled  $\alpha$ S show broadening with respect to a spectrum of a spin label in frozen solution at the same concentration. This concerns the spectra of  $\alpha$ S42,  $\alpha$ S56,  $\alpha$ S69, and  $\alpha$ S75, whereas  $\alpha$ S85 and  $\alpha$ S90 are not broadened. We attribute this broadening to intermolecular interactions, and note that it is intriguing that some positions show this broadening and others do not.

To determine whether short intramolecular distances occur in the fibrils of the doubly-labelled  $\alpha$ S protein, the broadening of the reference spectra is a complication.

Figure C1 shows the EPR spectra of doubly labelled  $\alpha$ S superimposed on the spectra of the 1:1 mixture of the respective reference spectra (for details, see Figure caption). The lineshapes of the spectra of  $\alpha$ S42/69,  $\alpha$ S42/75,  $\alpha$ S42/85,  $\alpha$ S56/69, and  $\alpha$ S75/85, are close to those of their respective references, showing the absence of short intramolecular distances, while the lineshapes of the spectra of  $\alpha$ S56/75,  $\alpha$ S56/90, and  $\alpha$ S69/85 are broader than their reference spectra.

To test the influence of the reference spectra on this result, in Figure C2, the spectra that show broadening in Figure C1 are compared to the most broadened

## Chapter 5

cw-EPR spectra of the respective singly-labelled  $\alpha$ S. In the comparison in Figure C2,  $\alpha$ S69/85 is not broadened, showing that the composition of the reference spectra has a strong effect on the outcome and suggesting that the broadening of  $\alpha$ S69/85 has an intermolecular component. The double mutants  $\alpha$ S56/75, and  $\alpha$ S56/90 show broadening in Figure C2, which could be intramolecular. It corresponds to a distance in the order of 2 nm for two-spin interaction. Because the lineshape of the reference spectra depends on the ratio by which the spectra of the two singly labelled  $\alpha$ S fibrils are added, the reference lineshape is uncertain. Therefore, a clear assignment to inter or intramolecular distances is not possible, and the cw-EPR data for  $\alpha$ S56/75 and  $\alpha$ S56/90 are not conclusive. Given the DEER data, it is more likely that the broadening is due to intermolecular interactions.

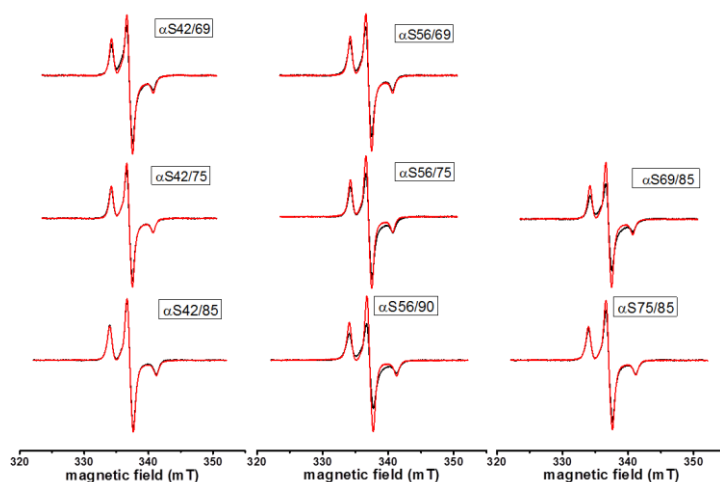


Figure C1. Continuous-wave EPR spectra of the fibrils in frozen solution of all the doubly labelled  $\alpha$ S proteins (black) superimposed with the 1:1 mixture of spectra of the respective singly labelled counterparts (red). Field scale applies to all vertically displaced spectra.

## Chapter 5

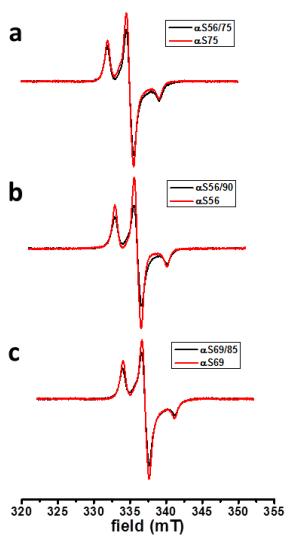


Figure C2. Comparison of the spectra of doubly labelled  $\alpha$ S fibrils in frozen solution superimposed with spectra of the respective singly labelled variants showing most broadened lineshape; a. the spectrum of  $\alpha$ S56/75 (black) with that of  $\alpha$ S75 (red), b. the spectrum of  $\alpha$ S56/90 (black) with that of  $\alpha$ S56 (red), and c. the spectrum of  $\alpha$ S69/85 (black) with that of  $\alpha$ S69 (red).

### ***Appendix D to chapter 5: Exploring Methods to Increase the DEER Evolution Time in $\alpha$ -Synuclein Fibrils: Deuteration of Buffer and 35 GHz DEER***

Longer DEER evolution times improve the sensitivity for longer distances. For  $\alpha$ -Synuclein ( $\alpha$ S) fibrils, we tested two commonly used approaches: replacing protons by deuterons to increase the  $T_2$  time of the electron spin and DEER at 35 GHz to make use of the higher sensitivity. Both approaches were tested on the  $\alpha$ S56/69 mutant in preparation of the experiments described in chapter 4 and 5.

#### Materials and methods

Expression and purification of cysteine mutants of the  $\alpha$ S were performed as described in chapter 5.

#### Preparation and harvesting of fibrillar $\alpha$ S

Fibrils of  $\alpha$ S were formed by incubating monomer solutions at a total protein concentration of 100  $\mu$ M. Fibrils of the doubly spin-labelled mutant were prepared with a diamagnetic dilution of 1 in 20, using 5  $\mu$ M spin-labeled  $\alpha$ S with 95  $\mu$ M wild-type protein. The fibrils of the corresponding singly labeled mutants were prepared using a diamagnetic dilution of 10  $\mu$ M spin-labeled  $\alpha$ S in the presence of 90  $\mu$ M wild-type  $\alpha$ S (1 in 10), to keep the spin-label concentrations constant. All aggregations were performed in 10 mM Tris – HCl, 50 mM NaCl, pH 7.4 buffer (abbreviated as H<sub>2</sub>O-Tris buffer). The total volume of the mixture was 3.0 ml, which was aliquoted into three Eppendorf tubes (Eppendorf LoProtein Bind 2ml), 1.0 ml each. All tubes were incubated at a temperature of 37 °C with constant shaking at 1000 rpm in a Thermo mixer (Eppendorf). The time evolution of  $\alpha$ S aggregation was monitored by the standard Thioflavin T (ThioT)

## Chapter 5

fluorescence assay. For each tube, fibrillization was stopped when the ThioT-fluorescence intensity reached a plateau. The fibrillization was generally completed in 6-8 days. Fibrils were harvested by ultra-centrifugation for 30 min at 120000xg using 70.1Ti rotor in a Beckman Coulter Ultracentrifuge. Centrifugation was performed at 4°C. The fibril pellets were washed three times by resuspending the pellets each time in 2.5 ml buffer used for fibrillization and re-centrifuging as described above. Glycerol (20 % (v/v)) was added to the washed fibril pellets before transferring them into the 3 mm (outer diameter) quartz tubes. The sample tubes were plunged into liquid nitrogen for fast freezing. These samples were used for EPR measurements.

Fibrils with deuterated buffer were prepared the same way as described above, however, the washing steps were done by resuspending into deuterated Tris-HCl (D<sub>2</sub>O-Tris), pH 7.4 buffer three times and re-centrifuging as described above. The buffer has the same composition as used for aggregation, but was prepared by dissolving the buffer salts in D<sub>2</sub>O instead of H<sub>2</sub>O. After the final wash, 20 % (v/v) of deuterated glycerol (glycerol-d<sub>8</sub>) was added to the fibril pellet. The fibril pellet was transferred into the EPR tube and flash-frozen in liquid N<sub>2</sub>. We tested this approach with one set of spin-labeled  $\alpha$ S mutants ( $\alpha$ S56/69,  $\alpha$ S56 and  $\alpha$ S69).

### T2 echo decay experiment

The two-pulse echo decay experiments were performed at 9.5 GHz on an ELEXSYS E680 spectrometer (Bruker, Rheinstetten, Germany) using a 3 mm split-ring resonator (ER 4118XMS-3-W1). The temperature was kept at 40 K with a helium-gas stream using a CF935 (Oxford Instruments, United Kingdom) cryostat with an ITC502 temperature controller (Oxford Instruments, United Kingdom). The pulse lengths for the two pulses,  $\pi/2$ - and  $\pi$ -pulses, were 80 and 160 ns. The initial separation of the two pulses was 120 ns.

## Chapter 5

### DEER measurements

The DEER measurements were performed at 9.5 GHz and 35 GHz. The DEER measurements at 9.5 GHz were performed on an ELEXSYS E680 spectrometer (Bruker, Rheinstetten, Germany) using a 3 mm split-ring resonator (ER 4118XMS-3-W1). The temperature was kept at 40 K with a helium-gas stream using a CF935 (Oxford Instruments, United Kingdom) cryostat with an ITC502 temperature controller (Oxford Instruments, United Kingdom). The pump and observer frequencies were separated by 70 MHz and adjusted as reported before (1). The pump-pulse power was adjusted to invert the echo maximally (2). The pump-pulse length was set to 16 ns. The pulse lengths of the observer channel were 16 and 32 ns for  $\pi/2$ - and  $\pi$  - pulses, respectively. All DEER measurements were performed as two-dimensional experiments, to suppress the proton modulation. To do so, DEER time traces were measured for ten different  $\tau$  -values spaced by 8 ns starting at  $\tau = 200$  ns. The typical accumulation times per sample were 16 h.

The 35 GHz DEER experiments were performed on the samples used for 9.5 GHz DEER. An ELEXSYS E580 spectrometer (Bruker, Rheinstetten, Germany) with a 3 mm, 35 GHz EPR resonator with a 150 W TWT amplifier was used. Temperature: 33 resp. 45 K; separation of pump and observer frequencies of 64.4 MHz. The pump-pulse was adjusted to the maximum of the echo-detected field-sweep spectrum and the observer-frequency to a frequency corresponding to 2.2 mT higher field. The pump-pulse lengths were optimized to maximally invert the echo and were between 14 and 20 ns. The pulse lengths of the observer channel were 10 and 20 ns for  $\pi/2$ - and  $\pi$  - pulses, respectively. The complete pulse sequence is given by:  $\frac{\pi}{2}_{\text{obs}} - \tau_1 - \pi_{\text{obs}} - t - \pi_{\text{pump}} - (\tau_1 + \tau_2 - t) - \pi_{\text{obs}} - \tau_2 - \text{echo}$ . The DEER time traces for ten different  $\tau_1$  values spaced by 8 ns, starting at  $\tau_1 = 180$  ns were added to suppress nuclear modulations. Accumulation time per sample was

## Chapter 5

2 hours. These experiments were performed at Bruker, Biospin Rheinstetten, Germany and we thank Patrick Carl for making this possible.

### Results and discussion

#### Comparison of fibrils in deuterated and protonated buffer

To see the effect of D<sub>2</sub>O exchange on the T<sub>2</sub> relaxation time for the  $\alpha$ S56/69 fibril samples, we performed a two-pulse echo-decay experiment. The echo-decay times of  $\alpha$ S56/69 fibrils in deuterated or protonated buffer are the same (Figure D1). At the first sight this result is surprising. Deuterating the buffer of soluble spin labelled proteins results in longer T<sub>2</sub> times, because protons are more effective than deuterons in enhancing T<sub>2</sub> relaxation of electron spins (3). Apparently, the high proton content of the fibril itself is sufficient to cause T<sub>2</sub> relaxation in the fibril samples, whether the buffer is deuterated or not. Therefore, the experiments described in chapter 4 and 5 were performed using protonated buffer. By harvesting the fibrils more efficiently, we were successful to extend the evolution times from 1.5  $\mu$ s in previous experiments to an evolution time of 1.8  $\mu$ s.

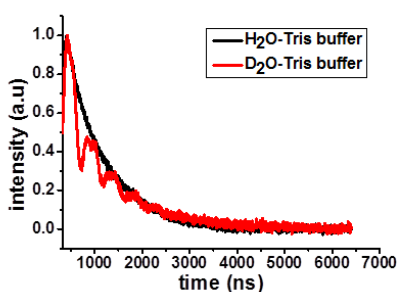


Figure D1. Effect of D<sub>2</sub>O exchange on the T<sub>2</sub> relaxation time for the  $\alpha$ S56/69 fibril sample; T<sub>2</sub> echo decay of  $\alpha$ S56/69 fibril with H<sub>2</sub>O-tris buffer (black) and D<sub>2</sub>O-tris buffer (red).

## Comparison of DEER measurements of $\alpha$ S56/69 fibrils at 9.5 GHz and 35 GHz

With 35 GHz DEER, a longer evolution time of 2.2  $\mu$ s and also a better signal to noise ratio is obtained than at 9.5 GHz. In Figure D2, the DEER data are shown. The distance distributions obtained after Tikhonov regularization show that both distributions have the most intense peak around 2.5 nm. In the DEER trace obtained at 35 GHz, this peak is more pronounced and shifted to shorter distances, which we attribute to a better separation of background and modulation, which is the result of the longer evolution time at 35 GHz. These results show that also for fibril samples, DEER at 35 GHz is advantageous.

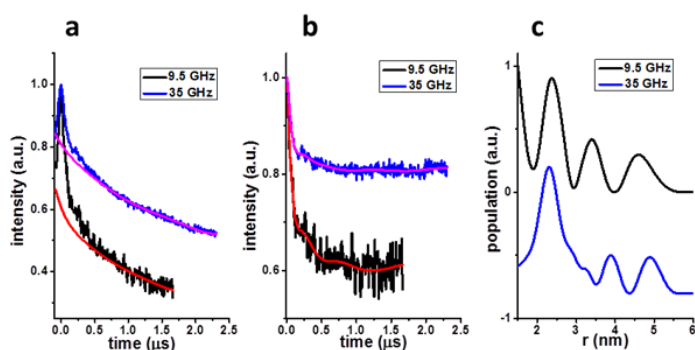


Figure D2. Results of DEER experiments for  $\alpha$ S56/69 fibril samples at 9.5 GHz (black line) and 35 GHz (blue line): a. DEER time traces with experimental background, b. DEER time traces after background correction along with the fits corresponding to the distance distributions shown in c; c. distance distributions derived from DEER data after Tikhonov regularization with a regularization parameter  $\alpha$  of 100. DEER time traces are normalized (maximum echo intensity is set to one) and shifted vertically for better visibility.

## References

1. Drescher M, Veldhuis G, van Rooijen BD, Milikisyants S, Subramaniam V, Huber M. Antiparallel arrangement of the helices of vesicle-bound  $\alpha$ -Synuclein. *J Am Chem Soc.* 2008;130:7796–7797.

## Chapter 5

2. Jeschke G. Distance measurements in the nanometer range by pulse EPR. *ChemPhysChem*. 2002;3:927–932.
3. Huber M, Lindgren M, Hammarström P, Mårtensson LG, Carlsson U, Eaton GR, Eaton SS. Phase memory relaxation times of spin labels in human carbonic anhydrase II: Pulsed EPR to determine spin label location. *Biophys Chem*. 2001;94:245–256.



## **6 Understanding the Peptide-Coiled-Coil Interaction of the Membrane-Fusion K/E Peptides**

## Chapter 6

### 6.1 Introduction

All living organisms utilize membrane fusion for their normal functioning. Cellular activities that involve membrane fusion are hormone secretion, enzyme release, neurotransmission etc. Membrane fusion needs a specialized set of proteins, such as the SNARE protein complex (1–7) (SNARE: soluble NSF attachment protein receptor; NSF=*N*-ethylmaleimide-sensitive factor). Membrane fusion induced by SNARE involves the coiled-coil interaction between three complementary SNARE proteins (8).

To understand this protein-mediated membrane fusion, a coiled-coil model system mimicking the complex of SNARE proteins was designed (9,10). It performs fusion by a pair of complementary lipidated oligopeptides E/K, which contain a lipid anchor segment, a coiled-coil zipper segment, and a linker that connects the two segments (see Figure 6.1). To gain a better picture on membrane fusion, we focus on the coiled-coil zipper segment of the complex, which consists of the helical peptides K and E, for sequences see Table 6.1.

The peptides are relevant to initiate the interaction of the two membranes to be brought together, a process that relies on complementary charges of K and E, and coiled-coil formation enhanced by the knob and hole principle (see Figure 6.2). Previous studies (9, 11) have shown that the K and E peptides behave differently in solution: E, anionic in nature, is in a random coil conformation and K, cationic in nature, has some helical character and a larger tendency to self-aggregate than E.

## Chapter 6

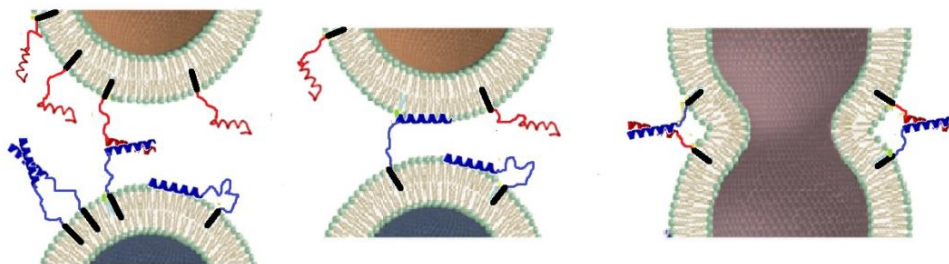


Figure 6.1. Membrane fusion model: Two membranes (top and bottom) are brought together by the lipidated peptide constructs (E/K): lipid anchor, black; PEG12 chains, the linker (for clarity drawn at the same color as the peptide); complementary peptides K, blue and E red respectively. The proposed interaction [by Rabe *et al.*, (12)] of peptide K with lipid head groups is not shown.

Table 6.1. Sequence of the helical peptides E and K

Peptides	sequences
E	Ac-(EIAALEK) <sub>3</sub> -GY-NH <sub>2</sub>
K	Ac-(KIAALKE) <sub>3</sub> -GW-NH <sub>2</sub>
E-SL	Ac-(EIAALEK) <sub>3</sub> -GYC(SL)-NH <sub>2</sub>
K-SL	Ac-(KIAALKE) <sub>3</sub> -GWC(SL)-NH <sub>2</sub>
SL-K	Ac-C(SL)-(KIAALKE) <sub>3</sub> -GW-NH <sub>2</sub>

C(SL): cysteine with MTSL attached, Ac: acetyl

A new mechanism was proposed about a twofold role of the K-peptide in membrane fusion (12,14): a. to first bring the target vesicles into close proximity ( $\approx 8$  nm) by E/K coiled-coil formation and b. to modify the head group regions of the K-peptide-binding sites at two different membranes, promoting protrusion of the lipid acyl chains as the initial state of lipid mixing. The role of K-peptide dehydration is not yet clear.

## Chapter 6

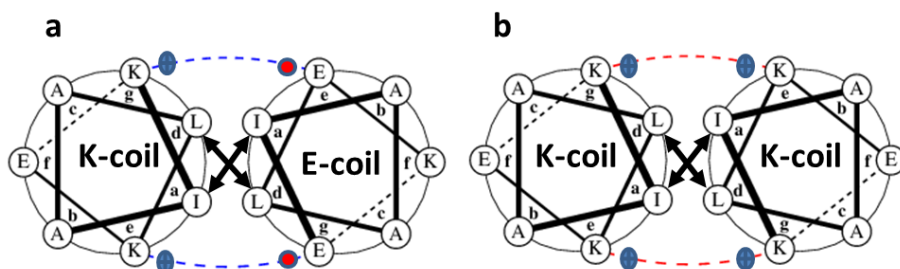


Figure 6.2. Helical wheel representation of the quaternary structure of parallel oriented (a) K/E-heterodimer and (b) K-homodimer. a, b, c, d, e, f, and g indicates the position of heptad repeats. Blue dashed line: coulomb attractions of the positively charged lysine side chains and negatively charged glutamate side chains; Red dashed line: coulomb repulsions of the positively charged lysine side chains; bold arrows: Van der Waals interactions of hydrophobic leucine and isoleucine side chains. Helical wheel projections also showing the knobs into hole model (13): Ile represents the hole; Leu represents the knob.

Circular-Dichroism (CD) experiments revealed the thermal folding, i.e., formation of  $\alpha$ -helices of the two peptides in aqueous solution (11,15), suggesting that the proteins form helical dimers. The folding constants ( $K_f$ ) were obtained for the pure E-peptides ( $5.3 \times 10^2 \text{ M}^{-1}$ ), the pure K-peptides ( $3.4 \times 10^3 \text{ M}^{-1}$ ) and mixtures of the E and K-peptides ( $1.8 \times 10^7 \text{ M}^{-1}$ ). The folding constant for the K-peptide suggests that it forms a dimer under the conditions of the present study.

Up to now, the presence of K-homodimers and their arrangement was not proven in a more direct way. For the E/K-heterodimer, techniques like Förster resonance energy transfer (FRET) and paramagnetic proton nuclear magnetic resonance (NMR) were applied to study the orientation of the heterodimer suggesting a parallel-oriented arrangement (16). The electron paramagnetic resonance (EPR) approach used in the present study, allows measuring distances between spin labels in a self-associated complex of identical (K/K) and non-identical (E/K) peptide molecules.

## Chapter 6

Here, we investigated variants of the oligopeptides E and K, synthesized (16,17) following the original protocol developed by Litowski and Hodges (11). The two oligopeptides are oppositely charged, attain random coil (E peptides) and  $\alpha$ -helical form (K peptides) in solution and form coiled-coil structures (11) when mixed together. The structure and the orientation of dimers are studied by continuous-wave (cw) EPR and a pulsed EPR method called double electron-electron resonance (DEER).

Similar to the results of other techniques (16,18), we detected the parallel orientation of the heterodimer of E/K peptides. In addition, we also detected the homodimers of K-peptides and their orientation.

## 6.2 Materials and methods

### 6.2.1 Peptide synthesis, labelling and sample preparation

The synthesis of the MTSL-labelled K and E peptides listed in Table 6.1 has been described elsewhere (16,17). Solutions of each peptide were prepared in PBS buffer containing 20% (wt) glycerol used as a cryo-protectant for the preparation of frozen samples listed in Table 6.2. For studying the E/K coiled-coil-complex formation the two different peptides were mixed in an 1:1 molar ratio by keeping the total peptide concentration at 0.3 mM. Peptide solutions were put into 3 mm (outer diameter) quartz tubes and then the samples were plunged into liquid nitrogen for fast freezing. The same samples were used for cw-EPR and DEER measurements.

## Chapter 6

Table 6.2. List of samples used for EPR measurements, for abbreviations see Table 6.1.

1	<b>E-SL</b>
2	<b>K-SL</b>
3	<b>SL-K</b>
4	<b>E-SL:K-SL</b>
5	<b>E-SL:SL-K</b>

### 6.2.2 cw-EPR measurements at 120 K

The 9.7 GHz cw-EPR measurements were performed using an ELEXYS E680 spectrometer (Bruker, Rheinstetten, Germany) with a rectangular cavity, using a modulation frequency of 100 kHz. For measurements at 120 K, a helium gas flow cryostat (Oxford Instruments, United Kingdom) with an ITC502 temperature controller (Oxford Instruments, United Kingdom) was used. The frozen samples were inserted in the pre-cooled helium gas flow cryostat. The EPR spectra were recorded using modulation amplitude of 0.25 mT and a microwave power of 0.63 mW. Typical accumulation times were 10-14min.

#### 6.2.2.1 Simulation of EPR spectra

The spectral simulation was performed using Matlab (7.11.0.584, Natick, Massachusetts, U.S.A) and the EasySpin package (19). For all simulations, the following spectral parameters were used:  $g = [2.00906, 2.00687, 2.00300]$  (20), the hyperfine tensor parameters  $A_{xx} = A_{yy} = 13$  MHz, and the  $A_{zz}$  parameter was varied. We used  $A_{zz} = 103$  MHz for **E-SL** and 102 MHz for both **K-SL** and **E-SL : K-SL**. The linewidth parameter (lwpp, peak to peak linewidth in mT) was obtained from the simulation of the spectrum of a sample of MTSL in the buffer described above

## Chapter 6

and was kept fixed for the simulation of the other spectra. A traceless-dipolar tensor of the form  $[-D - D + 2D]$ , in which  $2D$  represents the parallel component of the dipolar tensor, was used. The value of  $D$  (in MHz) was varied until the simulation agrees with the experimental spectrum. By doing this we were able to obtain the dipolar frequency (in MHz), from which the corresponding inter-spin distance is calculated.

### 6.2.3 DEER measurements

All DEER experiments were done at 9.5 GHz on an ELEXSYS E680 spectrometer (Bruker, Rheinstetten, Germany) using a 3 mm split-ring resonator (ER 4118XMS-3-W1). We performed the measurements at 40 K with a helium gas flow using a CF935 cryostat (Oxford Instruments, United Kingdom). The pump and observer frequencies were separated by 70 MHz and adjusted as reported before (21). The power of the pump-pulse was adjusted to invert the echo maximally (22–25). The length of the pump-pulse was set to 16 ns. The pulse lengths of the observer channel were 16 and 32 ns for  $\pi/2$ - and  $\pi$ - pulses, respectively. A phase cycle (+ x) - (- x) was applied to the first observer pulse. The complete pulse sequence is given by:  $\frac{\pi}{2_{\text{obs}}} - \tau_1 - \pi_{\text{obs}} - t - \pi_{\text{pump}} - (\tau_1 + \tau_2 - t) - \pi_{\text{obs}} - \tau_2 - \text{echo}$ . The DEER time traces for ten different  $\tau_1$  values spaced by 8 ns starting at  $\tau_1 = 200$  ns were added to suppress proton modulations. Typical accumulation times per sample were 16-20 hours.

#### 6.2.3.1 DEER analysis

In order to analyze the DEER traces and extract the distance distributions, the software package “DeerAnalysis 2011” was used (26). All the DEER traces were corrected by a homogeneous 3D-background function, which describes the three-

## Chapter 6

dimensional random distribution of nano-objects in the sample (21-24). This approach is justified because the proteins are soluble in buffer and no membranes are present. Peptides or proteins interacting with membranes can cause lower dimensionality background functions, such as a 2D background. The distance distribution was derived by the model-free Tikhonov regularization (22–26).

### 6.3 Results

Figure 6.3 shows the cw-EPR spectra of spin-labelled E and K peptides measured at 120 K. We compare the spectra of all peptide samples (listed in Table 6.2) with the spectrum of MTSL, which serves as a monomeric reference for the spin label under the solution conditions used for the K/E peptides. Figure 6.3a shows the superposition of the spectra of **E-SL**, **K-SL** and a 1 : 1 mixture of **E-SL** : **K-SL** with MTSL and Figure 6.3b shows the superposition of the spectra of **SL-K** and a 1 : 1 mixture of **E-SL** : **SL-K** with MTSL. Line broadening is observed for the spectra shown in Figure 6.3a, but not for those in Figure 6.3b. These observations are summarized in Table 6.3.

## Chapter 6

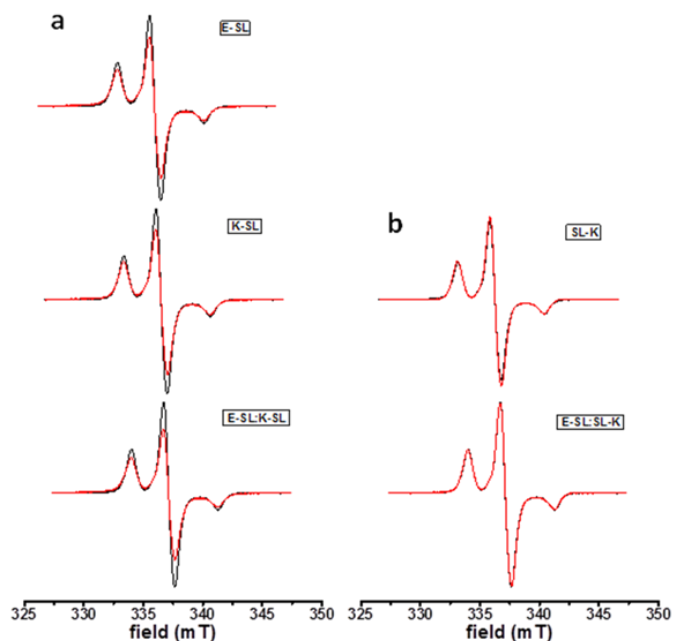


Figure 6.3. cw-EPR spectra of spin labelled E, K and coiled-coil E/K peptides at low temperature (120 K). a: Superposition of spectra of **E-SL**, **K-SL** and **E-SL : K-SL** peptides (red) is shown with the spectrum of pure MTSL (black), b: Superposition of spectra of **SL-K** and **E-SL : SL-K** (red) with the spectrum of free MTSL (black). All spectrum is normalized to the same number of spins.

Figure 6.4 shows the DEER results obtained for spin-labelled E and K peptide samples listed in Table 6.2; in Figure 6.4a the experimental DEER time traces before the background correction are displayed, in Figure 6.4b the experimental time traces after background correction with the fits corresponding to the distance distributions in Figure 6.4c. The experimental traces of **K-SL** and the 1 : 1 mixture of **E-SL : K-SL** (shown in Figure 6.4a) have a low modulation depth (see Table 6.3), showing that a significant population has conformations with distances outside the DEER measurement range (i.e., smaller than 2 nm or larger than 5 nm). In contrast, the modulation depth in the DEER traces of **E-SL**, **SL-K** and **E-SL :**

## Chapter 6

**SL-K** (see Table 6.3) shows that a significant population of spins in these samples have conformations with distances in the sensitive range of DEER.

Table 6.3. Summary of EPR properties and distances of E/K peptides

samples	cw-EPR line-broadening compared to MTSL	distance from cw-EPR spectra (nm)	modulation depth of the DEER trace	distance from DEER analysis (nm) (width (FWHM))
<b>E-SL</b>	yes	1.8 – 2.0	0.29	4.4 (1.6)
<b>K-SL</b>	yes	1.8 – 2.0	0.21	na
<b>SL-K</b>	no	no short distances	0.31	2.6 (1.4)
<b>E-SL : K-SL</b>	yes	1.8 – 2.0	0.22	na
<b>E-SL : SL-K</b>	no	no short distances	0.40	3.2 (1.3)

na: modulation depth too low to obtain relevant distances (see text); FWHM: full width half maximum of distance peak

The distance distribution obtained for **E-SL** is broad (full width half maximum (FWHM) 1.6 nm, see Table 6.3) with a maximum at 4.4 nm, whereas that for **SL-K** is narrow (FWHM 1.4 nm) with a maximum at 2.6 nm. The distance distribution of **E-SL : SL-K** is broad, suggesting that multiple conformations contribute to the distance distribution. The distance distributions for **K-SL** and **E-SL : K-SL** are not meaningful, because they represent only a very small population of spins in the sample (see above).

## Chapter 6

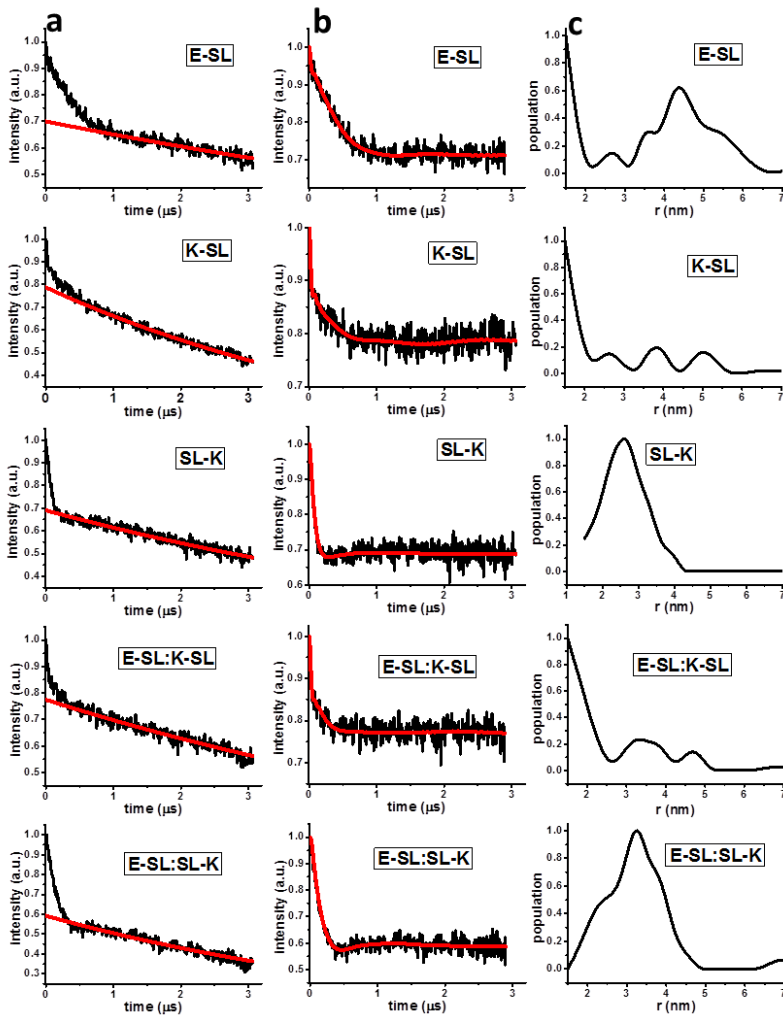


Figure 6.4. DEER results of experiments on spin labelled E and K peptides (listed in Table 6.2). a. DEER time traces before background corrections (black lines), background (red line); b. DEER time traces after background corrections (black line), fit of the time trace (red line) with the distance distributions shown in c; c. distance distributions obtained after Tikhonov regularization.

### 6.4 Discussion

In this study, we determine the interactions between the K- and the E-peptides by EPR using two complementary methods: Short distances (up to 2 nm) are detected by cw-EPR and longer distances by DEER. For these experiments, the peptides are investigated in frozen solution using the same sample for both types of measurements. Table 6.3 summarizes the results obtained.

The broadening of cw-EPR spectra is observed for **E-SL**, **K-SL** and **E-SL : K-SL** corresponds to distances in the range of 1.8 to 2.0 nm. These distances are derived from simulations of the EPR spectra (see Materials and methods). In the present samples, because of different spin-label linker conformations and the intermolecular nature of the interactions, cw-EPR line broadening most likely reflects not a single distance/conformation and therefore only a range of distances (see Table 6.3) can be derived from the broadening observed. Longer distances (> 2 nm) are detected by DEER, a method that gives the distance distributions, which reflect the distances of all members of the ensemble. Under the present experimental conditions, distances longer than 5 nm cannot be reliably detected. In DEER, the modulation depth reflects the fraction of the sample in which two spins interact within the distance range of the experiment, here 2-5 nm. Distance distributions of DEER experiments with low modulation depth, i.e., around 0.2, see Table 6.3, are not meaningful, because they are not representative of a major fraction of the spins in the sample. Using these principles we arrive at the following interpretations:

The K/E mixture shows a short distance when the C-termini of both peptides are labelled (cw-EPR) and a distance of 3.2 nm when the C-terminus of K and the N-terminus of E are labelled. The K peptide alone shows a short distance when labelled at the C-terminus and a distance of 2.6 nm when labelled at the N-

## Chapter 6

terminus, whereas E shows a broad range of distances, suggestive of unspecific aggregation.

A short distance between the two C-terminally labelled peptides (**E-SL : K-SL**) and a longer one, when one peptide is labelled at the C-terminus and the other at the N-terminus (**E-SL : SL-K**) is in qualitative agreement with a parallel heterodimer. The WebLab software (Molecular Simulations) calculations of the dimer, discussed below, qualitatively support this view.

The interaction of the spin-labels in the K-peptide is stronger for the C-terminally labelled K (**K-SL**) than for the N-terminally labelled K (**SL-K**). A distance between 1.8 nm and 2 nm for **K-SL** is only compatible with a parallel homodimer. The distance for **SL-K**, 2.6 nm, is consistent with a homodimer in which the spin labels point away from each other and possibly indicate flared-out ends of the N-terminal region of the homodimer.

In order to visualize the dimer of **E-SL : SL-K**, the model of the dimer has been created from WebLab software (Molecular Simulations) by assuming standard  $\phi$  (phi) and  $\psi$  (psi) angles for a regular  $\alpha$  helix including cysteine (SH) (both Cys-K and E-Cys). We have built the S-S bond and included the atoms required to define the MTSL label. The molecules were arranged as close as possible and in a parallel orientation (shown in Figure 6.5) to represent the quaternary structure of the E/K complex. The dimer of **E-SL : SL-K** with spin labels attached gives a distance of 3.5 nm in agreement with the result of DEER of a parallel heterodimer.

## Chapter 6

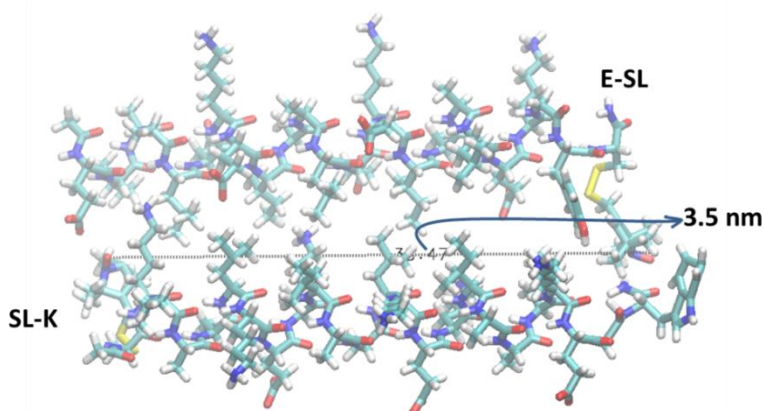


Figure 6.5. Quaternary structure of the E : K complex based on WebLab software (Molecular Simulations). Top: E-SL; Bottom: SL-K. Relative orientation: parallel with Ile and Leu oriented at the center of the E/K complex. The arrow indicates the distance between the spin labels attached to E- and K-peptide in the dimer form.

The quaternary structure of the parallel heterodimer has been also confirmed previously by different techniques (H-NMR, PRE-NMR, FRET) (16,18), and our present result is in full agreement with these results.

The finding of a K- homodimer based on DEER, in our study, was not described before.

We attribute the longer distance between the spin labels at the N-terminus (**SL-K**) to fraying of the helix ends in combination with the spin labels pointing away from each other. Distances between 1.8 and 2.0 nm at the C-terminus (**K-SL**) are consistent with the spin labels pointing towards each other. Fraying, as postulated for the N-terminus, may not be prominent for the C-terminus helix end (27,28). This is because the C-terminus contains a tryptophan residue, and could form a H-bond between the NO of the spin label and the NH proton of the indole group of the tryptophan.

The finding of a parallel homodimer for the K-peptide must be attributed to dominance of the knob-into-hole interaction (as depicted in Figure 6.2), which

## Chapter 6

overrides the unfavorable electrostatic interaction of the K-residues and the repulsive helix-dipole interaction of a parallel homodimer.

In general, we observe results that indicate K-homodimers and E/K heterodimers. The distances observed are consistent with a parallel heterodimer of the K and E peptide and a parallel homodimer of the K-peptide, in which the C-termini approach each other more closely than N-termini.

The absence of such an interaction for the E-peptides is in agreement with the previously found low tendency of the E-peptide to form dimers. The  $K_f$  of  $530 \text{ M}^{-1}$  (15) for E-homodimers would correspond to a population of 7% dimer under our conditions, which would be too low to detect. We attribute the broadened EPR spectra and the weak DEER response observed in the **E-SL** sample to unspecific aggregation.

In conclusion, we show that the EPR approach gives insight into the interaction of the K/E peptides in solution, peptides that are designed for membrane fusion. The study focused on the interaction of the peptide part of the membrane-fusion constructs, and opens the way to investigate molecular properties of the full membrane-fusion system.

### 6.5 References

1. Bennett M, Calakos N, Scheller R. Syntaxin: a synaptic protein implicated in docking of synaptic vesicles at presynaptic active zones. *Science*. 1992;257:255–259.
2. Oyler GA. The identification of a novel synaptosomal-associated protein, SNAP-25, differentially expressed by neuronal subpopulations. *J Cell Biol*. 1989;109:3039–3052.
3. Trimble WS, Cowan DM, Scheller RH. VAMP-1: a synaptic vesicle-associated integral membrane protein. *Proc Natl Acad Sci U S A*. 1988;85:4538–4542.
4. Südhof TC, De Camilli P, Niemann H, Jahn R. Membrane fusion machinery: insights from synaptic proteins. *Cell*. 1993;75:1–4.

## Chapter 6

5. Söllner T, Bennett MK, Whiteheart SW, Scheller RH, Rothman JE. A protein assembly-disassembly pathway in vitro that may correspond to sequential steps of synaptic vesicle docking, activation, and fusion. *Cell*. 1993;75:409–418.
6. Weber T, Zemelman BV., McNew JA, Westermann B, Gmachl M, Parlati F, Sollner TH, Rothman JE. SNAREpins: Minimal Machinery for Membrane Fusion. *Cell*. 1998;92:759–772.
7. Shi L, Howan K, Shen Q-T, Wang YJ, Rothman JE, Pincet F. Preparation and characterization of SNARE-containing nanodiscs and direct study of cargo release through fusion pores. *Nat Protoc*. 2013;8:935–948.
8. Burkhard P, Stetefeld J, Strelkov SV. Coiled coils: a highly versatile protein folding motif. *Trends Cell Biol*. 2001;11:82–88.
9. Robson Marsden H, Korobko AV, van Leeuwen ENM, Pouget EM, Veen SJ, Sommerdijk NAJM, Kros A. Noncovalent triblock copolymers based on a coiled-coil peptide motif. *J Protein Chem*. 2008;130:9386–9393.
10. Robson Marsden H, Elbers NA, Bomans PHH, Sommerdijk NAJM, Kros A. A Reduced SNARE Model for Membrane Fusion. *Angew Chemie Int Ed*. 2009;48:2330–2333.
11. Litowski JR, Hodges RS. Designing heterodimeric two-stranded alpha-helical coiled-coils. Effects of hydrophobicity and alpha-helical propensity on protein folding, stability, and specificity. *J Biol Chem*. 2002;277:37272–37279.
12. Rabe M, Aisenbrey C, Pluhackova K, de Wert V, Boyle AL, Bruggeman DF, Krisch SA, Bockmann RA, Kros A; Raap J, Bechinger B. A Coiled-Coil Peptide Shaping Lipid Bilayers upon Fusion. *Biophys. J*. 2016;111:1-14.
13. Crick FHC. The packing of  $\alpha$ -helices: simple coiled-coils. *Acta Crystallogr*. 1953;6:689–697.
14. Rabe M, Schwieger C, Zope HR, Versluis F, Kros A. Membrane Interactions of Fusogenic Coiled-Coil Peptides: Implications for Lipopeptide Mediated Vesicle Fusion. *Langmuir*. 2014;30:7724-7735.
15. Rabe M, Boyle A, Zope HR, Versluis F, Kros A. Determination of oligomeric states of peptide complexes using thermal unfolding curves. *Biopolymers*. 2015;104:65–72.
16. Zheng T, Boyle A, Robson Marsden H, Valdink D, Martelli G, Raap J, Kros A. Probing coiled-coil assembly by paramagnetic NMR spectroscopy. *Org Biomol Chem*.

## Chapter 6

- 2015;13:1159–1168.
17. Zheng T. Zipping into fusion. Thesis, Leiden University Repository. 2014
  18. Lindhout DA, Litowski JR, Mercier P, Hodges RS, Sykes BD. NMR solution structure of a highly stable de novo heterodimeric coiled-coil. *Biopolymers*. 2004;75:367–375.
  19. Stoll S, Schweiger A. EasySpin, a comprehensive software package for spectral simulation and analysis in EPR. *J Magn Reson*. 2006;178:42–55.
  20. Steigmiller S, Börsch M, Gräber P, Huber M. Distances between the b-subunits in the tether domain of FOF1-ATP synthase from *E. coli*. *Biochim Biophys Acta-Bioenerg*. 2005;1708:143–153.
  21. Drescher M, Veldhuis G, van Rooijen BD, Milikisyants S, Subramaniam V, Huber M. Antiparallel arrangement of the helices of vesicle-bound  $\alpha$ -Synuclein. *J Am Chem Soc*. 2008;130:7796–7797.
  22. Jeschke G. Distance measurements in the nanometer range by pulse EPR. *ChemPhysChem*. 2002;3:927–932.
  23. Jeschke G. Determination of the Nanostructure of Polymer Materials by Electron Paramagnetic Resonance Spectroscopy. *Macromol Rapid Commun*. 2002;23:227–246.
  24. Jeschke G, Koch A, Jonas U, Godt A. Direct conversion of EPR dipolar time evolution data to distance distributions. *J Magn Reson*. 2002;155:72–82.
  25. Jeschke G, Polyhach Y. Distance measurements on spin-labelled biomacromolecules by pulsed electron paramagnetic resonance. *Phys Chem Chem Phys*. 2007;9:1895-1910.
  26. Jeschke G, Chechik V, Ionita P, Godt A, Zimmermann H, Banham J, Timmel CR, Hilger D, Jung H. DeerAnalysis2006 - a comprehensive software package for analyzing pulsed ELDOR data. *Appl Magn Reson*. 2006;30:473–498.
  27. Milov AD, Tsvetkov YD, Gorbunova EY, Mustaeva LG, Ovchinnikova TV., Handgraaf J-W, Raap J. Solvent Effects on the Secondary Structure of the Membrane-Active Zervamicin Determined by PELDOR Spectroscopy. *Chem Biodivers*. 2007;4:1243–1255.
  28. Milov AD, Tsvetkov YD, Raap J, De Zotti M, Formaggio F, Toniolo C. Conformation, self-aggregation, and membrane interaction of peptaibols as studied by pulsed electron double resonance spectroscopy. *Biopolymers*. 2016;106:6–24.



## Summary

The protein  $\alpha$ -Synuclein ( $\alpha$ S) is known to be associated with Parkinson's disease. As an intrinsically disordered protein,  $\alpha$ S lacks an ordered structure in solution, while it forms an  $\alpha$ -helical structure when bound to membranes or it can form aggregates and  $\beta$ -sheets containing fibrils. Modifications of  $\alpha$ S such as phosphorylation are important for its function. Unstructured proteins are difficult to study by most of the available methods. We apply electron paramagnetic resonance (EPR) spectroscopy. Chapter 1 introduces the protein and describes briefly the EPR approaches used in this thesis.

The protein  $\alpha$ S plays its role by interacting with vesicles/membranes in nerve cells in the brain, and this interaction is believed to be crucial for both its pathological and physiological functions. Studies suggest that modifications like phosphorylation play a role in disease and that phosphorylation can modulate the membrane-binding ability of  $\alpha$ S. In chapters 2 and 3, we describe the binding of  $\alpha$ S with membranes. Membranes are represented by vesicles of different sizes and compositions to mimic the cell conditions. We place spin-labels at desired positions on the protein and, after mixing with vesicles, monitor the local membrane binding. Membrane binding shows up as immobilization of the spin label, and is detected by 9 GHz EPR.

Chapter 2 describes the study of the interaction of  $\alpha$ S with two natural membrane mimics, the inner mitochondrial membrane (IMM) and the neuronal plasma membrane (NPM). We observe that  $\alpha$ S binds surprisingly well to the two natural membranes considering their low surface charge density. In particular, a part of the protein that binds poorly to model membranes binds well to these natural membranes. This finding prompted us to investigate whether the membrane

## Summary

bound form of  $\alpha$ S has the extended conformation or the horseshoe conformation. To obtain such structural information, we measure the distance between two positions of  $\alpha$ S, in our case, two paramagnetic labels, by a pulse EPR method called double electron-electron resonance (DEER). We find that the majority of the protein is in the extended conformation. We also observe that the horseshoe conformation of  $\alpha$ S on natural membranes has a larger opening angle than previously found for model membranes.

In chapter 3, we discuss the effect of phosphorylation on the binding of  $\alpha$ S to model membranes. The effect of phosphorylation at positions S87 and S129, previously found to have an effect on membrane binding and aggregation of  $\alpha$ S, is investigated by using the same spin-label approach as described in chapter 2. We show that phosphorylation at position S87 causes local unbinding of  $\alpha$ S from the membrane; however, phosphorylation at S129 shows no effect on membrane binding. We also show that phosphorylation at position S87 does not detach the protein completely from the membrane, but rather causes local unbinding.

The chapters 4 and 5 are dedicated to the study of one of the peculiar properties of  $\alpha$ S that is to form fibrils. The fibrils of  $\alpha$ S are present abundantly in the Lewy bodies characteristic of Parkinson's disease. In the fibril, the protein chain of  $\alpha$ S is folded up in a specific way. Knowing this fold is important to identify the residues that are crucial for fibril formation. Therefore, to understand the inner structure, i.e., the fibril fold of  $\alpha$ S, is important. We focus on this particular issue in chapter 5. To determine the intrinsic fold of  $\alpha$ S in fibrils, distances between two spin labels in  $\alpha$ S in fibrils are measured by the similar pulse EPR method, DEER. We use a series of  $\alpha$ S proteins with two spin labels attached at different positions and prepare fibrils of all those protein constructs. We check if the fibrils of all protein constructs have similar morphology by negative stain transmission electron

## Summary

microscopy (TEM), described in chapter 4. We find that the fibrils of all protein constructs have a similar morphology. From these fibrils, we obtain eight long-range distance constraints that span the entire  $\beta$ -sheet region of  $\alpha$ S, from residue 42 to residue 90. This study paves the way to build a model of the inner fold of  $\alpha$ S in the fibril in the future.

In the last part of this thesis, in chapter 6, we focus on peptides that help in membrane fusion. Membrane fusion can be performed by constructs that consist of a lipid anchor segment and a coiled-coil zipper segment. We focus on the coiled-coil segment of the fusion complex. We use two small helical peptides, K and E. The two peptides, when mixed together, form coiled-coil structures. We investigate the structure and the orientation of the individual peptides by applying EPR. We report that the E/K peptides are in a parallel orientation in the heterodimer form, and that the K peptides form a parallel homodimer. The latter result has not been observed before. This study opens the way to investigate molecular properties of the full membrane-fusion system in the future.

This thesis shows that EPR can be used in determining the structure of disordered proteins that is difficult to study otherwise. As the presence of vesicles is not an obstacle for EPR, also biological processes like membrane fusion can be unraveled.



## Samenvatting

Het eiwit  $\alpha$ -Synuclein ( $\alpha$ S) speelt een rol bij de ziekte van Parkinson. Als een zogenaamd 'intrinsically disordered' eiwit, heeft  $\alpha$ S in oplossing geen gedefinieerde structuur. Wel kan het eiwit een  $\alpha$ -helix structuur aannemen, wanneer het bindt aan membranen, en  $\beta$ -sheets vormen, wanneer het aggregereert tot amyloid fibrillen. Tevens ondergaat het eiwit modificaties zoals fosforylering, wat belangrijk is voor het functioneren van het eiwit. Om eiwitten te bestuderen, die niet volledig gestructureerd zijn, voldoen de meeste beschikbare methoden niet. Wij hebben electron paramagnetic resonance (EPR) spectroscopie gebruikt en de toepasbaarheid voor dit doel onderzocht. In hoofdstuk 1 wordt het  $\alpha$ S eiwit geïntroduceerd en worden de EPR methodes beschreven, die in dit proefschrift zijn gebruikt.

Het eiwit  $\alpha$ S functioneert via interactie met vesicles/membranen in zenuwcellen in de hersenen, wat verondersteld wordt cruciaal te zijn voor zowel de pathologische als de fysiologische functies van het eiwit. Onderzoek suggereert dat modificaties zoals fosforylering een rol spelen bij de ziekte van Parkinson, omdat deze modificaties de binding van  $\alpha$ S aan membranen moduleren. In hoofdstukken 2 en 3 beschrijven we de binding van  $\alpha$ S aan membranen. Membranen worden gebruikt in de vorm van vesicles van verschillende grootte en samenstelling, om zoveel mogelijk de omstandigheden in cellen na te bootsen. We plaatsen een spin-label op de gewenste posities op het eiwit en na mengen met vesicles volgen we de lokale membraanbinding. Wanneer membraanbinding optreedt wordt het spin-label geïmmobiliseerd en gedetecteerd door middel van 9 GHz EPR.

Hoofdstuk 2 beschrijft de studie van de interactie van  $\alpha$ S met twee nagebootste natuurlijke membranen, namelijk het binnenste mitochondriële membraan (IMM)

## Samenvatting

en het neuronale plasma membraan (NPM). We stellen vast dat  $\alpha$ S goed bindt aan de twee natuurlijke membranen, wat verrassend is gezien hun lage ladingsdichtheid op het oppervlak. Het blijkt dat het deel van het eiwit dat zwak bindt aan modelmembranen, juist goed bindt aan deze natuurlijke membranen. Dit verrassende resultaat was aanleiding om te kijken of de membraangebonden vorm van  $\alpha$ S de langgerekte of de hoefijzer conformatie heeft. Om dergelijke structurele informatie te verkrijgen, hebben we de afstand gemeten tussen twee posities op het  $\alpha$ S eiwit, in feite tussen twee paramagnetische labels, door middel van gepulsde EPR technieken. Het merendeel van het eiwit blijkt de langgerekte conformatie te hebben. De hoefijzer conformatie vertoont bij binding aan natuurlijke membranen een grotere openingshoek dan eerder gevonden voor modelmembranen.

In hoofdstuk 3, bespreken we het effect van fosforylering op de binding van  $\alpha$ S aan modelmembranen. Het effect van fosforylering op de posities S87 en S129, waarvan eerder vastgesteld was dat deze een effect hebben op membraanbinding en aggregatie van  $\alpha$ S, is onderzocht door dezelfde methode van spin-labeling te gebruiken als beschreven in hoofdstuk 2. We laten zien dat fosforylering op positie S87 tot gevolg heeft dat  $\alpha$ S niet volledig, maar alleen op bepaalde posities op het eiwit, loslaat van het membraan; fosforylering op positie S129 vertoont geen effect op membraanbinding.

De hoofdstukken 4 en 5 zijn gewijd aan bestudering van de kenmerkende eigenschap van  $\alpha$ S om fibrillen te vormen. Fibrillen van  $\alpha$ S worden vooral aangetroffen in Lewy bodies, die karakteristiek zijn voor de ziekte van Parkinson. In fibrillen is de  $\alpha$ S eiwitketen op een speciale manier gevouwen. Kennis van deze vouwing is van belang om er achter te komen welke aminozuren cruciaal zijn voor fibrilvorming. Dit is het onderwerp waarop we focuseren in hoofdstuk 5. Om de

## Samenvatting

interne vouwing van  $\alpha$ S in fibrillen te bepalen, vormen we fibrillen van  $\alpha$ S eiwit, dat we op twee posities voorzien hebben van spin labels. Vervolgens meten we de afstand tussen de labels door middel van een gepulste EPR methode, double electron-electron resonance (DEER) genoemd. We gebruiken voor de fibrilvorming een reeks  $\alpha$ S eiwitten, waarbij paren van spin-labels op specifieke posities, verspreid over de aminozuurketen, aangebracht zijn. We hebben, door negatieve kleuring toe te passen, met transmissie elektronen microscopie (TEM) bekeken of alle eiwitconstructen leiden tot fibrillen met vergelijkbare morfologie, zoals beschreven is in hoofdstuk 4. De fibrillen van alle eiwitconstructen blijken inderdaad vergelijkbare morfologie te hebben. Voor de vouwing van  $\alpha$ S in fibrillen hebben we acht lange-afstands vouwingscriteria gevonden, verdeeld over het gehele  $\beta$ -sheet vormende deel van de  $\alpha$ S eiwitketen, van aminozuur 42 tot 90. Op basis van deze resultaten kunnen we in de toekomst een model creëren van de interne vouwing van  $\alpha$ S, zoals deze voorkomt in fibrilvorm.

Een ander aspect, dat beschreven wordt in hoofdstuk 6, focuseert op peptiden die een rol spelen bij membraanfusie. Membraanfusie kan bewerkstelligd worden door constructen, die bestaan uit een lipide-anker segment en een coiled-coil zipper ('rits') segment. We richten ons op het coiled-coil segment van het fusiecomplex. We maken gebruik van twee kleine peptiden, K and E, met helix structuur. De twee peptiden vormen coiled-coil structuren, wanneer ze samengevoegd worden. We onderzoeken de structuur en de oriëntatie van de individuele peptiden door EPR methodes toe te passen. We concluderen dat de E/K peptiden in een parallelle oriëntatie in de heterodimeer vorm voorkomen, en dat de K peptiden een parallelle homodimeer vormen. Dit laatste resultaat is niet eerder gevonden. Dit onderzoek opent de weg om de moleculair eigenschappen van het gehele membraanfusiesysteem in de toekomst in kaart te brengen.

## **Samenvatting**

Dit proefschrift laat zien dat EPR geschikt is om de structuur van niet volledig gevouwen eiwitten te bepalen, wat met andere methoden moeilijk te realiseren is. Omdat de aanwezigheid van vesicles geen belemmering is, is EPR ook geschikt om biologische processen, zoals membraanfusie, op te helderen.

# Curriculum Vitae

**Pravin Kumar**

Born on 12/02/1983 in Munger, Bihar, India.

## Research Experience

June 2012 – April 2017

PhD student

Huygens-Kamerlingh Onnes Laboratory

Leiden Institute of Physics

Leiden University

Leiden, The Netherlands

Project: Parkinson's Protein  $\alpha$ -Synuclein: Membrane Interactions and Fibril Structure

Supervisors: Dr. Martina Huber and Prof. dr. Edgar J.J. Groenen

July 2010 – Feb 2012

Junior research fellow

Biomolecular NMR facility

National Institute of Immunology

New Delhi, India

Project: Biophysical characterization of A $\beta$ -42 peptide (associated with Alzheimer's disease) and PfACP protein (from Plasmodium falciparum associated with Malaria)

Supervisor: Dr. Monica Sundd

## Education

July 2007 – July 2009

M. Sc. in Biotechnology

School of Biotechnology

Jawaharlal Nehru University

New Delhi, India

Project: Effect of polyamines on heat induced fibrillar aggregation using Lysozyme as a model protein.

Supervisor: Prof. Dr. Rajiv Bhat

June 2004- June 2007

B. Sc. in Biotechnology

C.C.S. University

Meerut, Uttar Pradesh, India

## Curriculum vitae

### Research related experience:

Teaching assistant for the bachelor course of Physics B for Life science and technology students

Thesis supervisor of one bachelor student

### Conferences and workshops

Oral presentation at Benelux EPR Society meeting 2016 in Liege, Belgium

Oral Presentation at Gorter symposium 2016 in Leiden, The Netherlands

Poster presentation at EFEP conference 2016 in Turin, Italy

Oral presentation at CHAINS 2015, Dutch Chemical Conference in Veldhoven, The Netherlands

Poster presentation at EFEP summer school 2015 in Berlin, Germany

Oral presentation at workshop "Amyloid Aggregation: Single molecule approach to a many molecule problem" Lorentz workshop 2015, Leiden University.

Poster presentations at Dutch Biophysics Conferences 2012-2016 in Veldhoven, The Netherlands

## List of Publications

### Published Articles

1. **Kumar P**, Bulk M, Webb A, Van der Weerd A, Oosterkamp T, Huber M, Bossoni L. A novel approach to quantify different iron forms in *ex-vivo* human brain tissue. *Scientific Reports*, 2016;6:1-11.
2. **Kumar P**, Schilderink N, Subramaniam V, Huber M. Membrane binding of Parkinson's protein  $\alpha$ -Synuclein: Effect of phosphorylation at positions 87 and 129 by the S to D mutation approach. *Israel Journal of Chemistry*, 2016; DOI: 10.1002/ijch.201600083
3. Dimitrova A, Walko M, Hashemi Shabestari M, **Kumar P**, Huber M, Kocer A. In situ, reversible gating of a mechanosensitive ion channel through protein-lipid interactions. *Frontiers in Physiology*, 2016;21:1-9.
4. **Kumar P**, Segers-Nolten IMJ, Schilderink N, Subramaniam V, Huber M. Parkinson's protein  $\alpha$ -Synuclein binds efficiently and with a novel conformation to two natural membrane mimics. *PLOS ONE*, 2015;10:1-11.
5. Hashemi Shabestari M, **Kumar P**, Segers-Nolten IMJ, Claessens MMAE, van Rooijen BD, Subramaniam V, Huber M. Three long-range distance constraints and an approach towards a model for the  $\alpha$ -Synuclein-fibril fold. *Applied Magnetic Resonance*, 2015;46: 369–388.
6. Schilder J, Liu WM, **Kumar P**, Overhand M, Huber M, Ubbink M. Protein docking using an ensemble of spin labels optimized by intra-molecular paramagnetic relaxation enhancement. *Physical Chemistry Chemical Physics*, 2016;18:5729-5742.
7. Gloaguen Y, Rebreyend C, Lutz M, **Kumar P**, Huber M, van der Vlugt JI, Schneider S, de Bruin B. An isolated nitridyl radical-bridged {Rh(N·)Rh} complex. *Angewandte Chemie International Edition*, 2014;53:6814-6818.

### In Preparation

1. **Kumar P**, Schilderink N, Subramaniam V, Huber M. Nanometer distance constraints for the fold of  $\alpha$ -Synuclein in fibrils of single morphology.
2. **Kumar P**, van Son M, Zhang T, Raap J, Kros A, Huber M. Understanding the peptide-coiled-coil interaction of the membrane-fusion K/E peptides.



## Acknowledgements

Yes, finally the journey is about to end. During these past years, I met really nice people, colleagues and friends, who contributed in many ways to the completion of my thesis.

I would like to express my gratitude to Dr. Martina Huber for giving me the opportunity to do my PhD in the MoNOS group. Thank you for supporting me and helping me with every step of my PhD. You made me learn a lot, especially about scientific presentation, writing, and planning my research. Thank you for correcting my English, especially the articles, throughout my PhD. I would also like to thank Prof. Edgar Groenen for his support and for giving fruitful suggestions during my PhD.

I would like to thank Prof. Vinod Subramaniam for his constant input and valuable discussion, together with his permission to use his lab facility and providing the proteins throughout my PhD. I would like to thank Dr. Ine Seger-Nolten for introducing me to  $\alpha$ -Synuclein fibrils preparation and harvesting, and a special thank for translating the summary of my thesis from English to Dutch. I learned how to prepare lipid-vesicles under the supervision of Dr. Martin Stöckl and I would like to acknowledge his kind help. The continuous supply of proteins was made possible just because of one person, Nathalie Schilderink, and I would like to thank her for that.

I would like to express my gratitude to all the members of the FOM program “A single molecule view on protein aggregation” for all the valuable discussions and feedback given during the progress meetings. Especially, I would like to thank Prof. Gerard Canters, Prof. Thijs Aartsma, Prof. Mireille Claessens, and Dr. Volodymyr Shvadchak for their motivational discussions and suggestions time to

## Acknowledgements

time. I am also thankful to Arshdeep, Aditya, Himanshu and Anja from the nanobiophysics group in the MESA+ institute of nanotechnology, University of Twente for all the scientific discussions and experimental help.

Working with our collaborators, Prof. Marcellus Ubbink, Prof. Alexander Kros, Dr. Jan Raap, Prof. A. Kocer, Prof. B. de Bruin, Dr. Yan Gloaguen, Dr. Tingting Zhang, and Dr. Lucia Bossoni was a great learning experience and I would like to thank them for that.

I am thankful to Dr. Navraj S. Pannu for his suggestion of performing the transmission electron microscopy (TEM) we needed for our fibril samples at the department of cell biology and histology, academic medical center, University of Amsterdam under the guidance of Dr. Nicole N. van der Wel. Therefore, I want to extend my gratitude to Dr. Nicole N. van der Wel, Henk van Veen and Daisy Picavet for their help and support in using the TEM microscope and in processing the TEM images.

Assistance by Nico Meeuwenoord in preparing spin-labelled A $\beta$ -40 peptides, Wim Jesse in introducing me to the DLS apparatus and CD spectroscopy, Geri Moolenaar for giving me access to the ultracentrifugation facility, Dr. Federica Galli for allowing me to use the AFM machine, is gratefully acknowledged.

I would like to thank Dr. Peter Gast for being a friendly floor manager; Henriette van Leeuwen, for her support in all the administrative matters and for being always ready to read my letters written in Dutch; Jos Disselhorst and Harmen van der Meer for their technical assistance. I am grateful to Frans Folst and Tom Jansen at the Leidse Instrumentmakers School (LIS) for preparing EPR tubes. Assistance by Arno van Amersfoort and Ruud Kuyvenhoven for the maintenance of the computers and the computer network is gratefully acknowledged. I am grateful to Siva Kanaku at expedition.

## Acknowledgements

I am grateful to Dr. Mykhailo Azarkh for being always there to clear all my doubts, mainly those related to simulations. I would like to thank Dr. Martin van Son for his initial help, especially in learning to work on the Bruker EPR machine. I would like to thank Dr. Kamran Mohammad along with Dr. Marija Mucibabic for helping me in performing AFM measurements many times and Dr. Aquiles Carattino for his computational help. I am also thankful to Rembrandt Donkersloot, who completed his bachelor project with me in the MoNOS group, for his curiosity and dedication to conduct the research.

I would like to extend my thanks to all my friends and colleagues from past and present at LION: Maryam, Saumaya Khatua, Saptaswa, Aquiles, Biswajit, Faezeh, Gabriele, Marija, Kamran, Nico, Lei, Martin, Weichun, Thomas, Lionell, Marcel, Miao and Enrico, not only for their scientific contributions, but also for being good and caring friends. Special thanks to Pedro and Mehdi for making Vijf Meiplein 62 like a home.

I would like to express my gratitude to the Gorter Foundation for providing me the financial support for my initial three months stay in Leiden. I would like to acknowledge FOM which, beyond the financial support, provided me with lots of opportunities to improve important skills and to get in contact with experts.

I would like to thank my parents for their endless love and support in each step at every moment of my life. Finally, very special thanks to my wife, Suhani, for her continuous love, support, patience and understanding.

